IMPROVING MAGNETIC RESONANCE THERMOMETRY USING RESPIRATION CORRECTION, ULTRASOUND FOCUS PREDICTION AND GOLDEN ANGLE STACK OF STARS SAMPLING

by

Bryant Troy Svedin

A dissertation submitted to the faculty of
The University of Utah
in partial fulfilment of the requirements for the degree of

Doctor of Philosophy

in

Physics

Department of Physics and Astronomy

The University of Utah

May 2017

The University of Utah Graduate School

STATEMENT OF DISSERTATION APPROVAL

The dissertation of **Bryant Troy Svedin**

has been approved by the following supervisory committee members:

Orest George Symko	, Chair	**02/17/2017** Date Approved
Dennis L. Parker	, Member	**02/17/2017** Date Approved
Allison Hampshire Payne	, Member	**02/17/2017** Date Approved
Clayton Williams	, Member	**02/17/2017** Date Approved
Brian Saam	, Member	**02/17/2017** Date Approved

and by **Benjamin C. Bromley** , Chair of

the Department of **Physics and Astronomy**

and by David B. Kieda, Dean of The Graduate School.

ABSTRACT

This dissertation presents original research that improves the ability of magnetic resonance imaging (MRI) to measure temperature in aqueous tissue using the proton resonance frequency (PRF) shift and T_1 measurements in fat tissue in order to monitor focused ultrasound (FUS) treatments. The inherent errors involved in measuring the longitudinal relaxation time T_1 using the variable flip angle method with a two-dimensional (2D) acquisition are presented. The edges of the slice profile can contribute a significant amount of signal for large flip angles at steady state, which causes significant errors in the T_1 estimate. Only a narrow range of flip angle combinations provided accurate T_1 estimates.

Respiration motion causes phase artifacts, which lead to errors when measuring temperature changes using the PRF method. A respiration correction method for 3D imaging temperature of the breast is presented. Free induction decay (FID) navigators were used to measure and correct phase offsets induced by respiration. The precision of PRF temperature measurements within the breast was improved by an average factor of 2.1 with final temperature precision of approximately 1 °C.

Locating the position of the ultrasound focus in MR coordinates of an ultrasound transducer with multiple degrees of freedom can be difficult. A rapid method for predicting the position using 3 tracker coils with a special MRI pulse

sequence is presented. The Euclidean transformation of the coil's current positions to their calibration positions was used to predict the current focus position. The focus position was predicted to within approximately 2.1 mm in less than 1 s.

MRI typically has tradeoffs between imaging field of view and spatial and temporal resolution. A method for acquiring a large field of view with high spatial and temporal resolution is presented. This method used a multiecho pseudo-golden angle stack of stars imaging sequence to acquire the large field of view with high spatial resolution and k-space weighted image contrast (KWIC) to increase the temporal resolution. The pseudo-golden angle allowed for removal of artifacts introduced by the KWIC reconstruction algorithm. The multiple echoes allowed for high readout bandwidth to reduce blurring due to off resonance and chemical shift as well as provide separate water/fat images, estimates of the initial signal magnitude M(0), T_2^* time constant, and combination of echo phases. The combined echo phases provided significant improvement to the PRF temperature precision, and ranged from ~0.3-1.0 °C within human breast. M(0) and T_2^* values can possibly be used as a measure of temperature in fat.

This work is dedicated to my wonderful wife Jen.

Thank you for pushing me to get my Ph.D.

TABLE OF CONTENTS

ABSTRACT iii

LIST OF FIGURES ix

LIST OF TABLES xv

LIST OF ACRONYMS xvi

Chapters

1. INTRODUCTION 1

    1.1 Introduction 1
    1.2 Overview of NMR Physics 3
        1.2.1. Quantum Mechanical Description 4
        1.2.2. Classical Description 9
        1.2.3. Bloch Equations - RF Excitation and Signal Generation 10
        1.2.4. Bloch Equations - Relaxation 12
    1.3 Signal Localization 16
        1.3.1. Slice Excitation 18
        1.3.2. Frequency Encoding 21
        1.3.3. Phase Encoding 22
        1.3.4. k-Space Formulation 23
        1.3.5. Sampling of k-Space 23
    1.4 Basic Pulse Sequences 24
        1.4.1. Gradient Echo 24
        1.4.2. Spin-Echo 25
        1.4.3. Signal Contrast 26
        1.4.4. Echo Planar Imaging 27
        1.4.5. Radial (Non-Cartesian) Imaging 30
    1.5 Image Reconstruction 31
        1.5.1. Cartesian Sampling 32
        1.5.2. Non-Cartesian Sampling 35
        1.5.3. Image Artifacts 37
        1.5.4. Water and Fat Separation 41
    1.6 References 42

2. MAGNETIC RESONANCE THERMOMETRY 48

2.1 Introduction 48
2.2 T1 Relaxation Time 48
2.3 T2 Relaxation Time 53
2.4 Proton Resonance Frequency Shift 54
2.4.1. Factors Affecting PRF Accuracy 56
2.5 References 58

3. FOCUSED ULTRASOUND 63

3.1 Introduction 63
3.2 Ultrasound Physics 64
3.3 Difficulties in FUS 68
3.4 References 70

4. THE EFFECT OF 2D EXCITATION PROFILE ON T1 MEASUREMENT ACCURACY USING THE VARIABLE FLIP ANGLE METHOD 72

4.1 Introduction 72
4.2 Theory 75
4.3 Methods 75
4.3.1. Simulations 75
4.3.2. Experiment 79
4.3.3. Flip Angle Correction Method 80
4.4 Results 80
4.5 Discussion 86
4.6 Conclusion 90
4.7 References 91

5. RESPIRATION ARTIFACT CORRECTION IN THREE-DIMENSIONAL PROTON RESONANCE FREQUENCY MR THERMOMETRY USING PHASE NAVIGATORS 93

5.1 Abstract 93
5.2 Introduction 94
5.3 Methods 97
5.3.1. Phase Navigator 97
5.3.2. Experiments 100
5.3.3. In Vivo Breast Nonheating Experiments 100
5.3.4. MRgFUS Phantom Experiments 101
5.4 Results 102
5.5 Discussion 107
5.6 Conclusion 109
5.7 References 109

6. FOCAL POINT DETERMINATION IN MAGNETIC RESONANCE-GUIDED FOCUSED ULTRASOUND USING TRACKING COILS 113

6.1 Abstract 113
6.2 Introduction 114
6.3 Methods 116
6.3.1. Hardware 116
6.3.2. Software 118
6.3.3. Tracker Coil Signal 120
6.3.4. Accuracy Verification 120
6.4 Results 123
6.5 Discussion 125
6.6 Acknowledgements 129
6.7 References 129

7. MULTI-ECHO PSEUDO-GOLDEN ANGLE STACK OF STARS THERMOMETRY WITH HIGH SPATIAL AND TEMPORAL RESOLUTION USING K-SPACE WEIGHTED IMAGE CONTRAST 133

7.1 Introduction 133
7.2 Methods 138
7.2.1. Sequence and Data Acquisition 138
7.2.2. Image Reconstruction 138
7.2.3. Respiration Correction 142
7.2.4. Coil Combination 143
7.2.5. Thermometry Calculations 144
7.2.6. Experiments 147
7.2.7. In Vivo Breast Nonheating Experiments 148
7.2.8. MRgFUS Phantom Experiments 150
7.3 Results 150
7.4 Discussion 160
7.5 Conclusion 163
7.6 Appendix A 164
7.7 Appendix B 165
7.8 References 166

8. CONCLUSIONS 172

LIST OF FIGURES

Figures Page

1.1 The Zeeman effect. A spin ½ particle placed in an external field will have two energy levels 7

1.2 Precession of a spin about an external magnetic field 10

1.3 a) 90° RF rotation of magnetization around y axis as seen in the laboratory frame. b) 90° RF rotation of magnetization around y axis as seen in the rotating frame 12

1.4 Relaxation for a spin system with T_2 = 100 ms and T_1 = 750 ms after a 90° RF pulse 13

1.5 Simulated FID signals from a spin system (ω_0 = 3kHz) with a) one isochromat ($\Delta B = 0$), b) two isochromats (ΔB = 0.25 kHz), and c) a continuum of isochromats (ΔB = 0.03 kHz) 16

1.6 Diagram of spin-echo signal acquisition. a) Magnetization vectors immediately after excitation. b-c) Blue – Slightly off resonant spins, Red – Very off resonant spins b) Magnetization vectors before the 180° pulse. c) Magnetization vectors after the 180° pulse. d) Magnetization vectors at time 2τ. e) Pulse sequence diagram showing the signal decaying by T_2^* and being refocused to an amplitude determined by T_2 17

1.7 Pulse truncation effects. a) Infinite sinc pulse and its slice profile. b) Truncated sinc pulse with 4 sidelobes and its slice profile. c) Hamming windowed truncated sinc pulse with 4 sidelobes and its slice profile 20

1.8 An RF pulse with a given bandwidth $\Delta\omega$. In the presence of $G_{z,1}$, a slice will be excited between $z_1 < z < z_2$, and in the presence of $G_{z,2}$, a slice will be excited between $z_3 < z < z_4$ 20

1.9 Pulse sequence timing diagram. After excitation, gradients move the sampling position of k-space 24

1.10 Gradient recalled echo timing diagram. The signal is refocused by a gradient area equal to the area of the defocusing gradient. $A_1 = A_2 = A_3$ 25

1.11 Example of visual illusion. The small squares in the middle have equal image intensity, but do not appear equally bright 26

1.12 Timing diagram of EPI sequence. All lines of k-space are acquired during each TR 28

1.13 Timing diagram of seg-EPI sequence. Multiple lines of k-space are acquired during each TR. Lines are interleaved to reduce artifacts 29

1.14 Timing diagram of seg-EPI flyback sequence. Multiple lines of k-space are acquired in the same direction during each TR 30

1.15 Cartesian vs. radial trajectory 31

1.16 Point Spread function with a) N=64 and b) N= 256 34

1.17 Example of density compensation effects. Left) Reconstructed image without density compensation has significant blurring. Right) Reconstructed image with density compensation 38

1.18 Example of Gibb's ringing. Left) Reconstructed image with 64 points along each direction. Middle) Reconstructed image with 128 points. Right) Reconstructed image with 256 points 38

1.19 Aliasing artifact due to undersampling along the horizontal direction by a factor of 2 39

1.20 Simulated gridding reconstruction using radial projections taken uniformly from 0 to π for, Left) 8 projections, Middle) 16 projections, Right) 32 projections 40

1.21 Example of chemical shift artifact. The position of fat is misregistered with respect to water due to a difference in frequency 41

2.1 Phase images from the current time frame during heating and from a reference time before heating. The phase difference is proportional to the temperature change. The arrow indicates the location of the temperature increase 56

3.1 Reflection and refraction of incident wave at interface between two mediums, in this case, $c_1 > c_2$ 66

3.2 Schematic diagram of ultrasound transducer with diameter D, focal length l_f, and focus diameter d 68

4.1 Excitation profile simulation results. Real component (solid) and imaginary (dashed). Black vertical bars show desired slice thickness of 3 mm. Comparison of TBP 2, 4, 6, 8, 10, at 90° flip angle, TR = 20 ms, T1 = 280 ms for a) initial

excitation profile b) and steady state profiles. c) Comparison of steady state profile for TBP 4 at various flip angles. 78

4.2 Comparison of total signal vs. flip angle from Bloch simulations (dash) to experiment (solid) for TBP 2, 4, 6, 8, and 10 using (a) gelatin phantom (T1 = 741±3 ms) and (b) breast fat (T1 = 278±8 ms). Signal vs. flip angle using calculated flip angle correction values for (c) gelatin phantom and (d) breast fat 82

4.3 Normalized total signal vs. flip angle from Bloch simulations for TBP 2, 4, 6, 8, 10 compared to normalized SPGR signal Eq. [4.1] at a) T1 = 740 ms and b) T1 = 280 ms. Signal vs. flip angle using calculated flip angle correction values for c) T1 = 740 ms and d) T1 = 280 ms 83

4.4 Bloch simulation calculations of T1for every combination of flip angles displayed as percent of true T1. a-c) T1 = 280 ms a) TBP 2, b) TBP 6, c) TBP 10. d-f) T1 = 740 ms d) TBP 2, e) TBP 6, f) TBP 10 83

4.5 Bloch simulation calculations of T1 for every combination of flip angles using flip angle correction displayed as percent of true T1. a-c) T1 = 280 ms a) TBP 2, b) TBP 6, c) TBP 10. d-f) T1 = 740 ms d) TBP 2, e) TBP 6, f) TBP 10. Flip angles shown are desired flip angle 85

4.6 Bloch simulation calculations of T1 for every combination of flip angles using flip angle correction within 5% of true T1. a-c) T1 = 280 ms a) TBP 2, b) TBP 6, c) TBP 10. d-f) T1 = 740 ms d) TBP 2, e) TBP 6, f) TBP 10. Flip angles shown are desired flip angle 85

4.7 Experimental calculations of T1 for every combination of flip angles using flip angle correction displayed as percent of true T1. a-c) T1 = 280 ms a) TBP 2, b) TBP 6, c) TBP 10. d-f) T1 = 740 ms d) TBP 2, e) TBP 6, f) TBP 10. Flip angles shown are desired flip angle 87

4.8 Monte Carlo simulations of standard deviation of T1 for every combination of flip angles using flip angle correction. Results are displayed as SNR multiplied by the fractional error of true T1. a-d) T1 = 280 ms a) TBP 2, b) TBP 6, c) TBP 10, d) SPGR. e-h) T1 = 740 ms e) TBP 2, f) TBP 6, g) TBP 10, h) SPGR. Flip angles shown are desired flip angle 87

5.1 (a) Modified segmented EPI sequence with flyback readout. FID phase navigator readouts are acquired before and after EPI readout. (b) Example of phase during navigator readout for a single TR. (c) Example of average phase difference estimate for 8 coils during one image acquisition. (d) Example of phase variation about constant phase difference for 8 coils during one image acquisition. (e) Example of field shift (in ppm) for one coil over 30 image acquisitions..... 98

5.2 In vivo breast images for the five healthy volunteers. Top two row: Magnitude images uncorrected (top row) and corrected (bottom row). Middle two rows: Standard deviation of magnitude uncorrected (top row) and corrected (bottom row). The color scale indicates the percent of the mean signal value. Bottom two rows: Standard deviation of PRF temperature estimates in water and glandular tissue (°C) uncorrected (top row) and corrected (bottom row) 104

5.3 Phantoms under nonheating conditions. (a) PRF temperature precision images for gelatin and pork comparing the no breathing, breathing without correction, and breathing with correction cases without FUS heating. (b) PRF temperature change of a single voxel in gelatin phantom for all three cases. (c) PRF temperature change of a single voxel in pork phantom for all three cases..... 105

5.4 MRgFUS phantom experiments. (a) PRF temperature change images at the time of the peak temperature for gelatin and pork comparing the no breathing, breathing without correction, and breathing with correction cases with MRgFUS heating. (b) PRF temperature change of a single voxel in gelatin phantom for all three cases. (c) PRF temperature change of a single voxel in pork phantom for all three cases..... 106

6.1 a) MRgFUS breast system b) Cross section showing various degrees of freedom. c) Tracker coil arrangement. The transducer is cut in half horizontally to clearly show tracker coils. d) Conceptual circuit design. Coil axis is rotated ~15° from vertical to give maximum signal possible for every transducer position. e) Locator Sequence for one readout direction GR. This is applied along Gx, Gy and Gz to locate the tracker coil..... 117

6.2 Transducer positions and imaging slabs. Green – Parallel slab. Yellow – Perpendicular slab. RO – Readout direction. a) Initial position at Φ=10°, δ=2 cm, α=0°. b) Φ=20°, δ=2 cm, α=0°. c) Φ=20°, δ=3 cm, α=0°. d) Φ=20°, δ=3 cm, α=10°. Red lines show approximate ultrasound beam propagation. Curved blue line outlines the transducer face. All experiment locations used one of these four positions with the system rotation θ at 0°, 40° or 90°. See Figure 1b for definitions of θ, δ, α, and Φ..... 122

6.3 a) Example tracker signal from a single coil for all 6 readout directions with inset showing zoomed in profiles. b) Tracker signal vs. head-foot distance from isocenter for four Φ rotations for tracker coil #2. c) Gradient warp correction distance as a function of head-foot distance from isocenter for four Φ rotations for tracker coil #2. d-e) Predicted focus movement relative to the first predicted location with and without gradient warp correction for the LR axis (d) and AP axis (e). f) Deviation from expected difference relative to the first predicted focus location with and without gradient warp correction for the HF axis 124

6.4 PRF temperature at the focus overlaid on magnitude images for the three orthogonal planes through the temperature center of mass for all 16 transducer positions of the parallel slab imaging case. The calculated temperature center of

mass location is shown by a green marker and the predicted focus location from the tracker coils is shown by a blue marker 126

7.1 a) Example of fully sampled pseudo-golden angle (PGA) k-space with 34 projections. b) Asymmetric KWIC window with 3 center and 34 outermost projections. c) Example of k-space sampling using KWIC with 3 center and 13 outermost projections. d) Example of k-space sampling using KWIC with 8 center and 34 outermost projections. e) Example of k-space sampling using KWIC with 3 center and 34 outermost projections at the first reconstructed time point. f) Example of k-space sampling using KWIC with 3 center and 34 outermost projections at the second reconstructed time point. 139

7.2 Separated water (left) and fat (right) images for in vivo breast coronal (left column) and sagittal (right column) for five volunteers and pork phantom (bottom left). Yellow line in fat images display the location of the center slice in the other orientation 151

7.3 Standard deviation through time maps of PRF temperature in aqueous tissue for the four calculation methods for volunteer 2. Left column: 1st image used as phase reference. Right column: Trajectory-matched baseline images. Top Row: PRF temperature calculated from the last echo. Bottom row: PRF temperature calculated from the combined phase..... 152

7.4 Standard deviation through time maps of PRF temperature in aqueous tissue for each volunteer using the CE-TB method and image set 1. The total number of aqueous voxels for each image orientation and volunteer is displayed at the bottom of each image 153

7.5 a) Standard deviation through time maps of PRF temperature in aqueous tissue with (left) and without (right) respiration correction for volunteer 4 using the CE-TB method and image set 1. b) Example of measured field shift in the central slice of the image set 1 coronal acquisition for volunteer 4..... 154

7.6 Spatially averaged PRF standard deviation as a function of TE in aqueous tissue in the breast for volunteer 3 and image set 1. Errors bars are the standard error of the average PRF standard deviation for each echo image volume. PRF temperature calculated using the: Red) SE-FB method; Blue) SE-TB method; Green) CE-FB method; Black) CE-TB method. The combined phases (CE methods) only used the echoes up to and including the displayed TE 155

7.7 a) Spatially averaged PRF standard deviation values from image set 1 for the last TE in aqueous tissue in the breast for each volunteer in the coronal and sagittal orientations for each of the four calculation methods. Errors bars are the standard error of the spatial values. PRF temperature calculated using: Red) SE-FB method; Blue) SE-TB method; Green) CE-FB method; Black) CE-TB method. Bars between methods indicate no statistically significant difference between the

methods. b) Average improvement in PRF precision compared to the SE-FB method. Bars between improvement values indicate no statistically significant difference between the methods 156

7.8 a) Example of SOS multiecho exponential decay with weighted linear least squares fit to data removing offset C (green) and without removing offset C (red dash). b) Example of T_2^* measurements within the breast without removing C (left) and with removing C (right). The T_2^* values within aqueous and adipose tissue are more uniform after removing the offset C. c) Example of the measured offset value C within the breast 157

7.9 Standard deviation through time maps for volunteer 2 of M(0) and T2* as a percent difference from the baseline value determined using the trajectory matched baseline library a) using only the in phase echoes and b) using all echoes in the fit 158

7.10 Phantom FUS heating. a) PRF temperature change during FUS heating in aqueous tissue within a pork phantom. Solid red line – CE-TB Stack of stars sequence. Dashed blue line – seg-EPI sequence. b) Percent change in M(0) (black) and percent change in T_2^* (red) during FUS heating in adipose tissue within a pork phantom. Vertical bars indicate the duration of the FUS..... 159

LIST OF TABLES

Tables Page

1.1 Factors that determine signal weighting 27

5.1 Comparison of in vivo breast results..... 105

5.2 Phantom results 106

LIST OF ACRONYMS

ADC	Analog to Digital Converter
AP	Anterior-Posterior
ARFI	Acoustic Radiation Force Imaging
COM	Center of Mass
CT	Computed Tomography
DESPOT1	Driven Equilibrium Single Pulse Observation of T1
EPI	Echo Planar Imaging
FID	Free Induction Decay
FOV	Field of View
FUS	Focused Ultrasound
GA	Golden Angle
GRE	Gradient Recalled Echo
GUI	Graphical User Interface
HF	Head-Foot
HIFU	High Intensity Focused Ultrasound
ICE	Image Calculation Environment
IR	Inversion Recovery
IRB	Institutional Review Board
KWIC	k-Space Weighted Image Contrast

LR	Left-Right
MnCL2	Manganese Chloride
MRgFUS	Magnetic Resonance Guided Focused Ultrasound
MRgHIFU	Magnetic Resonance Guided High Intensity Focused Ultrasound
MRI	Magnetic Resonance Imaging
NMR	Nuclear Magnetic Resonance
NUFFT	Non-Uniform Fast Fourier Transform
PD	Proton Density
PE	Phase Encoding
PGA	Pseudo-Golden Angle
PPM	Parts Per Million
PRF	Proton Resonance Frequency
PSF	Point Spread Function
RF	Radiofrequency
RO	Readout
seg-EPI	Segmented Echo Planar Imaging
SNR	Signal to Noise Ratio
SOS	Stack of Stars
SPGR	Spoiled Gradient Recalled
TBP	Time Bandwidth Product
TE	Echo Time
TR	Repetition Time

US	Ultrasound
VFA	Variable Flip Angle

CHAPTER 1

INTRODUCTION

1.1 Introduction

This dissertation will present work done to improve temperature imaging in magnetic resonance imaging (MRI). The ability of MRI to noninvasively provide real-time temperature measurements provides unique advantages, especially when coupled with a noninvasive therapy such as focused ultrasound (FUS). Near real-time measurements of induced temperature change can ensure patient safety as well as treatment efficacy. MR-guided FUS (MRgFUS) has a wide range of promising applications including the treatment of cancer (1-3), localized drug delivery (4-6), and neuromodulation (7,8). High spatial and temporal resolution combined with a large imaging field of view are critical for successful monitoring of thermal therapy treatment (9). The large field of view is necessary to monitor any near/far-field heating that may occur, and the high temporal resolution is critical due to the rapid accumulation of tissue damage at high temperature. For many applications, these demands on monitoring are not currently met.

Currently, clinical monitoring of MR-guided FUS (MRgFUS) treatments is limited to a single (or relatively few) two-dimensional (2D) slices (10-16) providing a limited field of view. It can also be difficult to properly position a single 2D slice to capture the entire focus. Multiple 2D slices will have a gap between each slice,

meaning any temperature increase in the gap will not be measured. Respiration and motion artifacts will also introduce errors to the temperature monitoring. Partial volume effects cause an underestimation of the actual temperature achieved (17), which will increase with voxel size.

3D MR thermometry can overcome many of the field of view, partial volume, and coverage gap limitations, which are inherent in 2D imaging but unfortunately, standard 3D sequences typically require too much time to acquire k-space to be clinically viable. Imaging in 3D will also allow for zero-filled interpolation along all 3 dimensions, providing a more correct representation of the temperature profile (18). The works presented in this dissertation are focused on improving the viability of 3D temperature measurements to provide sufficient spatial and temporal resolution to meet the necessary demands for successful thermal treatment monitoring.

This dissertation is divided into eight chapters. The rest of this chapter provides the background and theory of MRI. The quantum and classical mechanical descriptions of nuclear magnetic resonance (NMR) are covered, followed by basic imaging techniques. Chapter 2 discusses the different methods available in MRI to monitor temperature changes. The strengths and weaknesses of each method are covered. Chapter 3 gives a brief introduction to how FUS works. FUS is the method used to deliver energy for all of the heating experiments in this thesis. Chapter 4 describes the inherent problems in measuring the longitudinal relaxation time T_1 using the variable flip angle method with 2D images. In Chapter 5, a respiration artifact correction method is covered in detail. 3D imaging is more susceptible to motion artifacts and requires a robust method of correction. Chapter 6 presents a fast and

accurate method for locating the geometric focus of an ultrasound transducer in MR coordinates. Locating the ultrasound focus in MR coordinates of a transducer with multiple degrees of freedom can be difficult, especially when no position sensors are present in the system. By quickly and accurately locating the focus, overall treatment time and efficacy will be improved. In Chapter 7, a unique method of providing 3D temperature measurements with high spatial and temporal resolution with a large field of view is presented. This method uses a stack of stars sequence using a pseudo-golden angle acquisition and k-space weighting to improve temporal resolution. By also acquiring multiple echoes, separate water/fat images are produced as well as the ability to calculate the initial signal magnitude and the time constant T_2^*, both of which can provide another measure of temperature. Multiple echoes also allows for echo combination to improve the temperature precision using the proton resonance frequency (PRF) shift thermometry technique. Chapter 8 summarizes the work accomplished and describes potential future work to be done.

1.2 Overview of NMR Physics

The Stern-Gerlach experiments in the 1920s demonstrated that particles possess an intrinsic spin angular momentum that only takes certain quantized values (19). Isidor Rabi and his team were able to measure the magnetic moment of particles using molecular beams and an oscillating magnetic field (20), for which he won a Nobel Prize in 1944. The magnetic resonance phenomenon, in which particles absorb electromagnetic radiation at a specific energy corresponding to the strength of the magnetic field and the magnetic properties of the particle, was discovered independently in 1946 by Felix Bloch and Edward Purcell (21,22), who were both

awarded the Nobel Prize for their discovery in 1952. For the next 20 years, NMR was used to study the chemical and physical properties of molecules.

In 1973, Paul Lauterbur introduced the idea of spatially varying magnetic fields, or gradients, to spatially encode the information from each spin (23). He used a back-projection technique, similar to computed tomography (CT), to create the first MR images. Peter Mansfield demonstrated the relationship of the Fourier transform to the magnetic gradients and signal location (24). Lauterbur and Mansfield shared the Nobel Prize in Medicine in 2003 for their work. Richard Ernst made use of this Fourier transform relationship to produce 2D images with frequency and phase encoding in 1975 (25). This technique is the basis of current MRI techniques.

Magnetic resonance imaging has been an incredibly successful imaging modality. MRI provides incredible versatility in imaging. It has the ability to create both 2D and 3D images along any plane. It also provides excellent soft tissue contrast as well as several methods of generating contrast between different tissues. A more thorough examination of MR signal creation, detection, localization, and image formation is presented throughout the rest of this chapter, where the majority of the presented information comes from the books written by Liang and Slichter (26,27). NMR is one of the rare topics that can be described in both the quantum and classical point of views (27). The quantum mechanical description will be considered first, followed by the classical description.

1.2.1 Quantum Mechanical Description

The majority of the quantum mechanical description in this section is found in Slichter (27). Spin is a fundamental property of nature like electrical charge or mass.

The spin of a particle is specific and unchangeable. Protons, neutrons and electrons all have spin ½, and atomic nuclei can have 0, ½-integer, or integer spin quantum number. It is only particles with nonzero spin that exhibit the magnetic resonance phenomenon. Almost every element on the periodic table has an isotope with a nonzero nuclear spin. Some spin ½ nuclei of interest in MR imaging include ^{1}H, ^{3}He, ^{13}C, ^{19}F and ^{31}P, while nuclei with other spin values ^{17}O (spin 5/2) and ^{23}Na (spin 3/2) are also used. MRI is most commonly performed using the spin ½ hydrogen nucleus due to its natural abundance in the human body. The work in this thesis is based solely on ^{1}H MRI studies and therefore the theory presented will only deal with spin ½ systems.

An isolated particle with spin s will have a total angular momentum:

$$\vec{J} = J_x\hat{\imath} + J_y\hat{\jmath} + J_z\hat{k} \qquad [1.1]$$

The eigenvalues of J^2 and J_z are $\hbar^2 s(s+1)$ and $\hbar m$ where s = 0, ½, 1, 3/2, …, m = -s, -s+1, … s, and ħ is Planck's constant divided by 2π. For any nucleus with nonzero spin, m has (2s+1) possible values. For spin ½ particles, there are only two possible eigenstates, spin up ($|\uparrow\rangle$) with m = ½ and spin down ($|\downarrow\rangle$)with m = -½. The general state of the nucleus is a linear combination of the two eigenstates

$$\Psi = c_+|\uparrow\rangle + c_-|\downarrow\rangle \qquad [1.2]$$

where c_+ and c_- are complex constants determined by initial conditions.

The particle's magnetic moment μ is related to the total angular momentum by

$$\vec{\mu} = \gamma\vec{J} \qquad [1.3]$$

where γ is the gyromagnetic ratio. The value of γ is proportional to the inverse of twice its mass, $1/2m$. The dependence of the gyromagnetic ratio to a particle's mass creates

a factor of nearly 2000 difference between the gyromagnetic ratio of the proton and electron. The magnitude of the magnetic moment is $\mu = \gamma\hbar\sqrt{s(s+1)}$. While the magnitude of μ is known whether or not there is an external magnetic field, its direction is completely random without an external field present due to thermal random motion. The exception to this takes place in ferromagnets, which exhibit spontaneous magnetization. When an external field $\vec{B}$ is applied along the z direction $\vec{B} = B_0\hat{k}$, the z-component of μ is $\mu_z = \gamma\hbar m$ (27). The interaction energy between the magnetic field and the magnetic moment of the 2s+1 different eigenstates is

$$E_m = -\vec{\mu} \cdot \vec{B} = -\gamma\hbar B_0 m. \qquad [1.4]$$

The general solution is obtained by summing the individual eigenstates and adding the time dependence

$$\Psi(\mathrm{t}) = \sum_{m=-s}^{s} c_m |s, m\rangle e^{-iE_m t/\hbar} \qquad [1.5]$$

For spin ½ systems there are only two stationary states and the particle can exist in any combination of the two states, reducing Equation [1.5] to

$$\Psi(\mathrm{t}) = c_+|\uparrow\rangle e^{-i\gamma B_0 t/2} + c_-|\downarrow\rangle e^{i\gamma B_0 t/2} \qquad [1.6]$$

The expectation value for the three components of the nucleus' magnetic moment can be computed by

$$\langle\mu_{x,y,z}\rangle = \int \Psi(\mathrm{t})^* \mu_{x,y,z} \Psi(\mathrm{t}) \mathrm{d}\tau \qquad [1.7]$$

It can be shown that the expectation values for the individual components for the spin ½ system described in Equation [1.6] are (27),

$$\langle\mu_x\rangle = \frac{\gamma\hbar}{2}\sin(\theta)\cos(\omega_0 t + \phi_0) \qquad [1.8]$$

$$\langle \mu_y \rangle = \frac{\gamma\hbar}{2} \sin(\theta) \sin(\omega_0 t + \phi_0) \quad [1.9]$$

$$\langle \mu_z \rangle = \frac{\gamma\hbar}{2} \cos(\theta) \quad [1.10]$$

where $\omega_0 = \gamma B_0$ is known as the Larmor frequency. The expectation values show that the magnetic moment will precess about the main field at a fixed angle, θ, with frequency ω_0. Particles with spin up will be parallel to the main field and be in the lower energy state, while spin down particles will be antiparallel and be in the higher energy state. The energy difference between the two states is

$$\Delta E = \gamma\hbar B_0 = \hbar\omega_0. \quad [1.11]$$

The splitting of energy levels based on spin is known as the Zeeman effect and is illustrated in Figure 1.1.

When a group of spin ½ particles is placed in a magnetic field, there are only two energy states. Transitions between energy states can occur through spontaneous or stimulated emission. The populations of the two states at equilibrium is governed

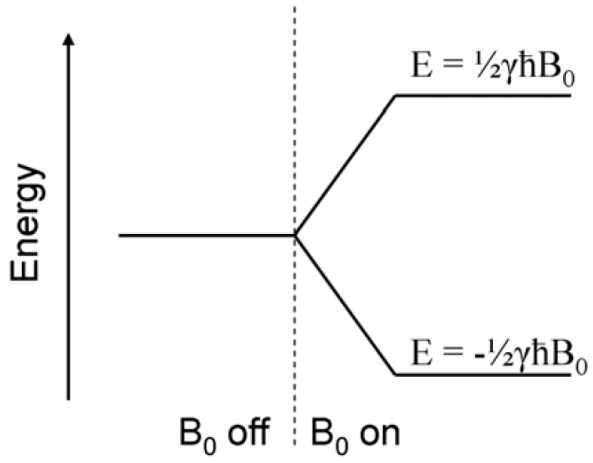

Figure 1.1. The Zeeman effect. A spin ½ particle placed in an external field will have two energy levels.

by the energy difference and the Boltzmann relationship

$$\frac{N_\uparrow}{N_\downarrow} = \exp\left(\frac{\Delta E}{kT}\right) \quad [1.12]$$

where $N_\uparrow$ is the number of spins aligned parallel, $N_\downarrow$ is the number of spins anti-parallel, k is the Boltzmann constant and T is the absolute temperature of the spin system. According to the Boltzmann relation, the probability of spins being up (lower energy state) is slightly higher than being down. The population difference can be quickly estimated by expanding the exponential term using a first order approximation

$$\frac{N_\uparrow}{N_\downarrow} \approx 1 + \frac{\Delta E}{kT} = 1 + \frac{\gamma \hbar B_0}{kT} \quad [1.13]$$

The population difference is then obtained using $N_{tot} = N_\uparrow + N_\downarrow$

$$N_\uparrow - N_\downarrow \approx N_{tot} \frac{\gamma \hbar B_0}{2kT} \quad [1.14]$$

Substituting the values for a typical MRI situation, B_0 = 3 T, the gyromagnetic ratio of ^{1}H $\gamma = 42.58\ MHz/T$, and human body temperature T = 310 K, the population difference is approximately one in a million. Even though the population difference is very small, enough signal for detection is generated due to the very large number of spins within a sample. Each spin will have a magnetic moment $\mu_z = {}^1/_2\,\gamma\hbar$, and using the population difference from Equation [1.9], the net magnetization M_z of the sample can be approximated as

$$M_z \approx N_{tot} \frac{\gamma^2 \hbar^2 B_0}{4kT}. \quad [1.15]$$

The net magnetization is oriented along the main magnetic field, is proportional to the total number of spins, the main field strength, and inversely proportional to temperature. As temperature decreases, the population difference and net

magnetization will increase.

1.2.2 Classical Description

The majority of the classical description given here is found in Liang (26). A magnetic moment will experience torque when placed in an external magnetic field. The resulting torque is equal to the rate of change of its angular momentum J.

$$\frac{d\vec{J}}{dt} = \vec{\mu}\times\vec{B} \qquad [1.16]$$

The magnetic moment is related to the angular momentum by $\vec{\mu} = \gamma\vec{J}$, giving

$$\frac{d\vec{\mu}}{dt} = \gamma\vec{\mu}\times\vec{B} \qquad [1.17]$$

This relation holds whether $\vec{B}$ is a static or time varying field. It also means that at any moment the changes in μ are perpendicular to both $\vec{\mu}$ and $\vec{B}$. When B is a constant field, Equation [1.17] can be easily solved to give

$$\mu_{xy}(t) = \mu_{xy}(0)e^{-i\gamma B_0 t} = \mu_{xy}(0)e^{-i\omega_0 t} \qquad [1.18]$$

$$\mu_z(t) = \mu_z(0) \qquad [1.19]$$

The longitudinal magnetization μ_z remains constant while the transverse magnetization will precess around the main field with the Larmor frequency ω_0, forming a cone shape. This is similar to the wobbling of a spinning top in a gravitational field and is shown in Figure 1.2. The precession predicted by the classical mechanical approach is the same as predicted from the expectation values derived using the quantum mechanical approach.

The net magnetization is a sum of all the individual magnetic moments, and the longitudinal component will sum to a nonzero value as shown in Equation [1.15],

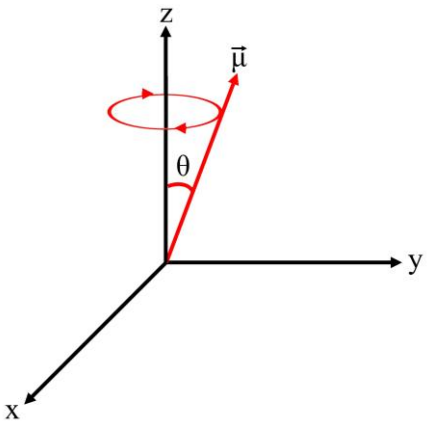

Figure 1.2. Precession of a spin about an external magnetic field.

while there is no transverse component of the net magnetization. The z magnetization will remain stationary in time. In order to create a detectable signal, the longitudinal magnetization must be rotated into the transverse plane as discussed in the next section.

1.2.3 Bloch Equations - RF Excitation and Signal Generation

An oscillating magnetic field applied at the correct frequency can rotate the magnetization into the transverse plane. This is often referred to as RF (radiofrequency) excitation, as the excitation frequency in typical MRI (20-450 MHz) is in the radio portion of the spectrum. The excitation magnetic field is referred to as the B_1 field and is given by the expression

$$\vec{B}_1(t) = 2\vec{B}_1^e(t)\cos(\omega_{rf}t + \phi)\,\hat{\imath} \qquad [1.20]$$

where $\vec{B}_1^e(t)$ is an envelope function that is really the heart of an RF pulse, ω_{rf} is the frequency of the RF pulse and ϕ is the initial phase. Equation [1.17] needs to be modified slightly to account for how the magnetization responds to a B_1 field and is known as the Bloch equation:

$$\frac{d\vec{M}}{dt} = \gamma\vec{M}\times\vec{B} - \frac{M_x\hat{\imath} + M_y\hat{\jmath}}{T_2} - \frac{(M_z - M_z^0)\hat{k}}{T_1} \quad [1.21]$$

where T_2 is the transverse (also known as spin-spin) relaxation time constant and T_1 is the longitudinal (also known as spin-lattice) relaxation time constant. More detail about T_1 and T_2 is provided on relaxation in the next section.

As long as the RF pulse duration is much shorter than T_1 or T_2, their effects can be ignored during excitation. It is often easier to describe what is happening to the magnetization both conceptually and mathematically when in a rotating frame of reference that is rotating at the RF frequency. In the rotating frame of reference, and during excitation, Equation [1.21] becomes

$$\frac{d\vec{M}}{dt} = \gamma\vec{M}\times\vec{B}_{eff} \quad [1.22]$$

$$\vec{B}_{eff} = \left(B_0 - \frac{\omega_{rf}}{\gamma}\right)\hat{k} + B_1^e(t)\hat{\imath} \quad [1.23]$$

where $\vec{B}_{eff}$ is the effective magnetic field in the rotating frame (26). From these equations, it is evident that when the frequency of the RF pulse matches the Larmor frequency, only the transverse B_1 field remains. The magnetization will rotate around B_1 until B_1 is turned off. The amount the longitudinal magnetization is tipped into the transverse plane is called the flip angle α and is related to the shape and magnitude of the B_1 field and the length of the pulse τ_p as follows

$$\alpha = \int_0^{\tau_p} \gamma B_1^e(t)dt. \quad [1.24]$$

Figure 1.3 shows a 90° flip angle in both the laboratory and rotating frames of reference.

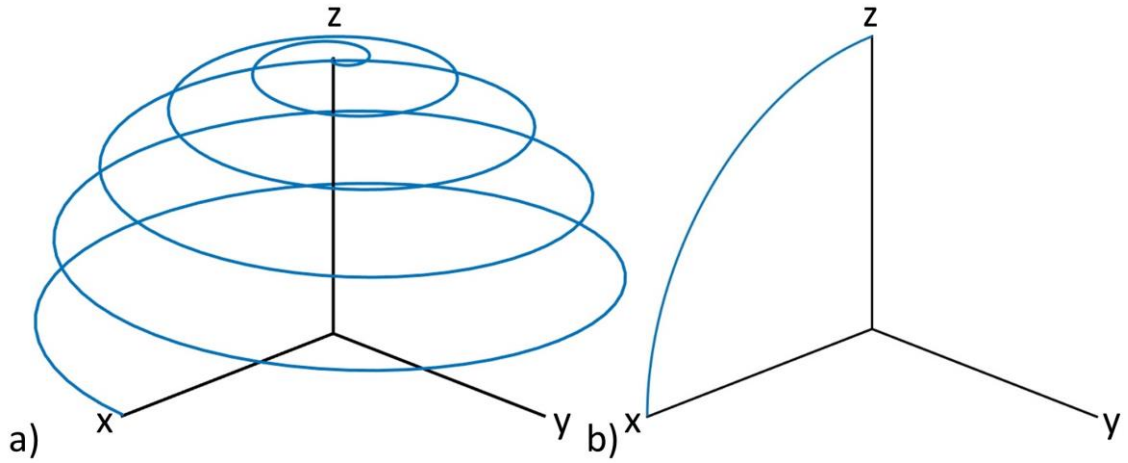

Figure 1.3. a) 90° RF rotation of magnetization around y axis as seen in the laboratory frame. b) 90° RF rotation of magnetization around y axis as seen in the rotating frame.

1.2.4 Bloch Equations - Relaxation

After excitation, the evolution of the magnetization can be described by the Bloch equations in the rotating frame (Equation [1.21]) with B_{eff} set to zero, which can be broken apart into two separate ordinary differential equations.

$$\frac{dM_z}{dt} = -\frac{(M_z - M_z^0)\hat{k}}{T_1} \quad [1.25]$$

$$\frac{dM_{xy}}{dt} = -\frac{M_{xy}}{T_2} \quad [1.26]$$

The solutions to these two equations are

$$M_z(t) = M_z^0\left(1 - e^{\frac{-t}{T_1}}\right) + M_z(0)e^{\frac{-t}{T_1}} \quad [1.27]$$

$$M_{xy}(t) = M_{xy}(0)e^{\frac{-t}{T_2}} \quad [1.28]$$

The only difference to these two equations in the laboratory frame is that the transverse magnetization, Equation [1.28], will rotate at the Larmor frequency. These equations show that the transverse magnetization will decay exponentially with the time

constant T_2 and the longitudinal magnetization will relax back to its thermal equilibrium value of M_z^0 with the time constant T_1. The transverse magnetization is the source of the detectable signal and must be sampled before it has decayed. Figure 1.4 shows the relaxation of the longitudinal and transverse magnetization after a 90° excitation pulse.

T_1 relaxation is the mechanism by which the z component of the magnetization reaches thermal equilibrium with its surroundings. Spontaneous emission of energy is extremely unlikely in the NMR range of frequencies. All energy emission in NMR must be stimulated through another magnetic field fluctuating near the Larmor frequency in the transverse plane. The source of the locally fluctuating field is typically another proton or electron on the same or a nearby molecule causing direct dipole

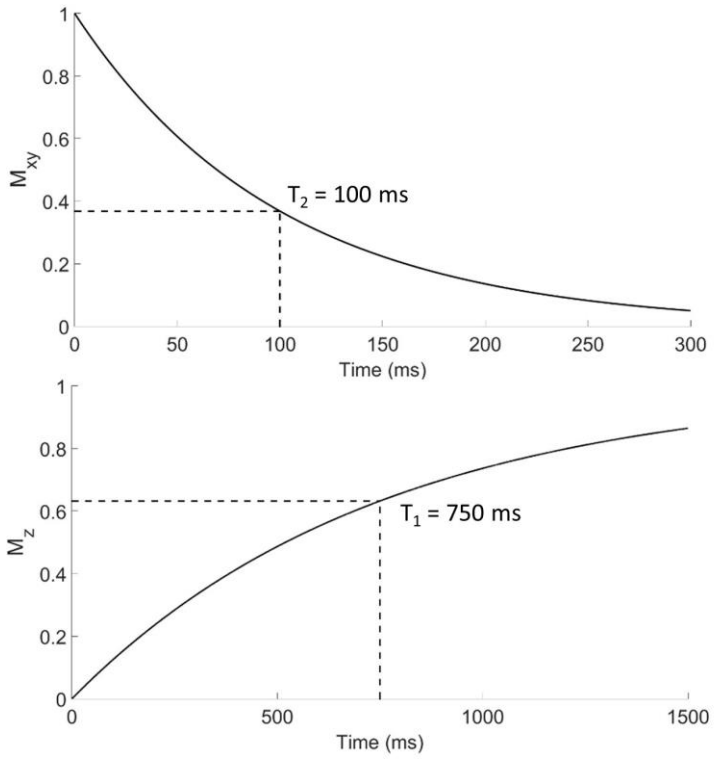

Figure 1.4. Relaxation for a spin system with T_2 = 100 ms and T_1 = 750 ms after a 90° RF pulse.

interactions or through collisions, and rotations. These dipole fields are local and affect only a few spins. The stimulated transfer of energy that the spins obtained from the RF pulse back to the surrounding environment (also referred to as the lattice) is what restores the equilibrium state. This is why T_1 relaxation is referred to as spin-lattice relaxation.

The transverse relaxation time constant T_2 is known as spin-spin relaxation for the mechanisms by which it decays. After an RF pulse, the nuclear spins are phase coherent and are precessing at the same frequency. The coherence is gradually lost due to microscopic and/or macroscopic field inhomogeneities and direct interactions between spins with and without the transfer of energy to the lattice. This relaxation does not affect the total amount of z magnetization. T_2 is typically less than or much less than T_1. T_1 relaxation occurs when a spin exchanges energy with its external environment. If such an energy exchange were to affect one of the spins contributing to the transverse signal, both the transverse and longitudinal components of its angular momentum would be randomly changed and it would immediately lose phase relations with other spins and thus contribute to T_2 decay. Any process causing T_1 relaxation also results in T_2 relaxation. T_2 relaxation can also occur with dipolar interactions. In this mechanism, a pair of spins simultaneously exchange their longitudinal angular momentum components resulting in no net T_1 effect but loss of T_2 coherence (28).

The simplest form of signal detection in MR is known as free induction decay (FID) signal. For a system comprised of spins resonating perfectly at the Larmor frequency, the magnetization will decay exactly as Equation [1.28] describes. This is,

of course, never found in nature. Local chemical makeup or field inhomogeneities will cause spins to resonate with varying frequencies, which are called isochromats. The different frequencies will cause the transverse signal to lose phase coherence, and thus decay faster. The FID signal is characterized by a different relaxation constant T_2^* that is related to T_2 by

$$\frac{1}{T_2^*} = \frac{1}{T_2} + \gamma \Delta B \qquad [1.29]$$

where ΔB is the strength of the local spatially varying field. The T_2^* time constant is shorter than T_2. A simulated example of the FID signal is shown in Figure 1.5, where the difference between T_2 and T_2^* is evident when comparing a) and c). Figure 1.5c was generated using Equation 4.15 from (26).

FID phase decoherence is not a true relaxation process as it is not random. For molecules that are not moving, the signal can be recovered by performing a spin-echo experiment. The spin-echo was discovered by Erwin Hahn (29). Immediately after excitation, all of the spins are pointed in the same direction, Figure 1.6a. Some of the spins will rotate faster than others. This spreads out the spins until the sum of the transverse components is zero, Figure 1.6b. A 180° RF pulse can be applied in the transverse plane at time τ after the initial RF pulse to cause the spins to change their phase by 180°, Figure 1.6c. Those spins that were spinning faster and were ahead, are now behind, but continue to spin faster. At time 2τ the phases will again be coherent, Figure 1.6d. The realignment of the spins into a coherent signal is referred to as an echo, and the time the echo is form is called the echo time (TE). It turns out that an echo can be formed from any combination of 2 or more RF pulses (30). It is also possible to form an echo using only the gradients, which are referred to as gradient

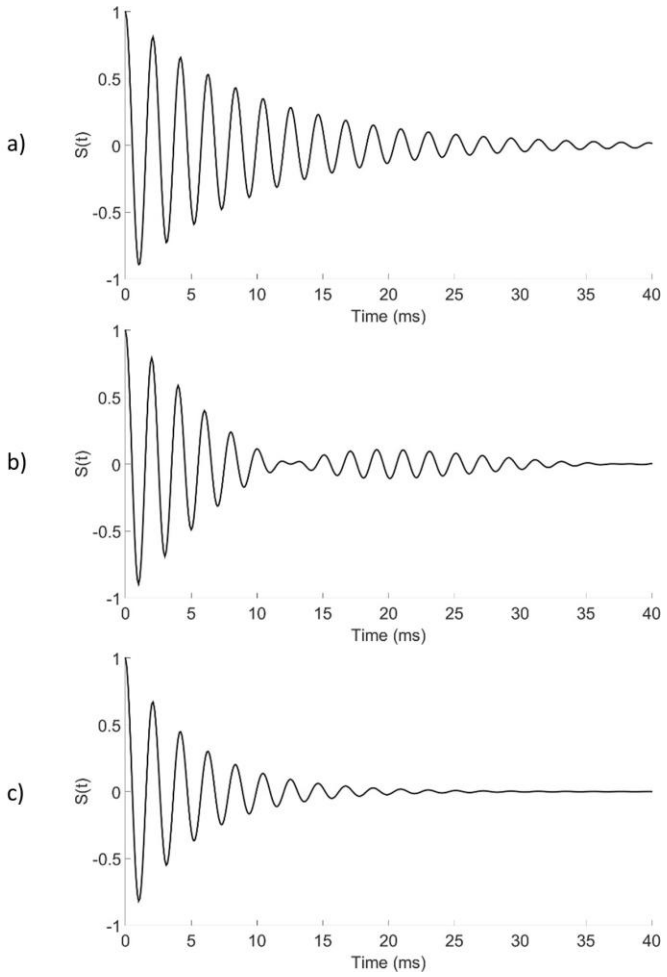

Figure 1.5. Simulated FID signals from a spin system ($\omega_0 = 3$ kHz) with a) one isochromat ($\Delta B = 0$), b) two isochromats ($\Delta B = 0.25$ kHz), and c) a continuum of isochromats ($\Delta B = 0.03$ kHz).

echoes to distinguish them from spin-echoes, and are described in Section 1.4.1.

1.3 Signal Localization

After the spins have been tipped into the transverse plane, an MR signal is detectable. In order to create an image, the received signal must be mapped to its source location. This is accomplished through the use of magnetic gradients. The gradient applies a spatially varying magnetic field on top of the main field. The spatially varying field will cause spins from different locations to rotate at different

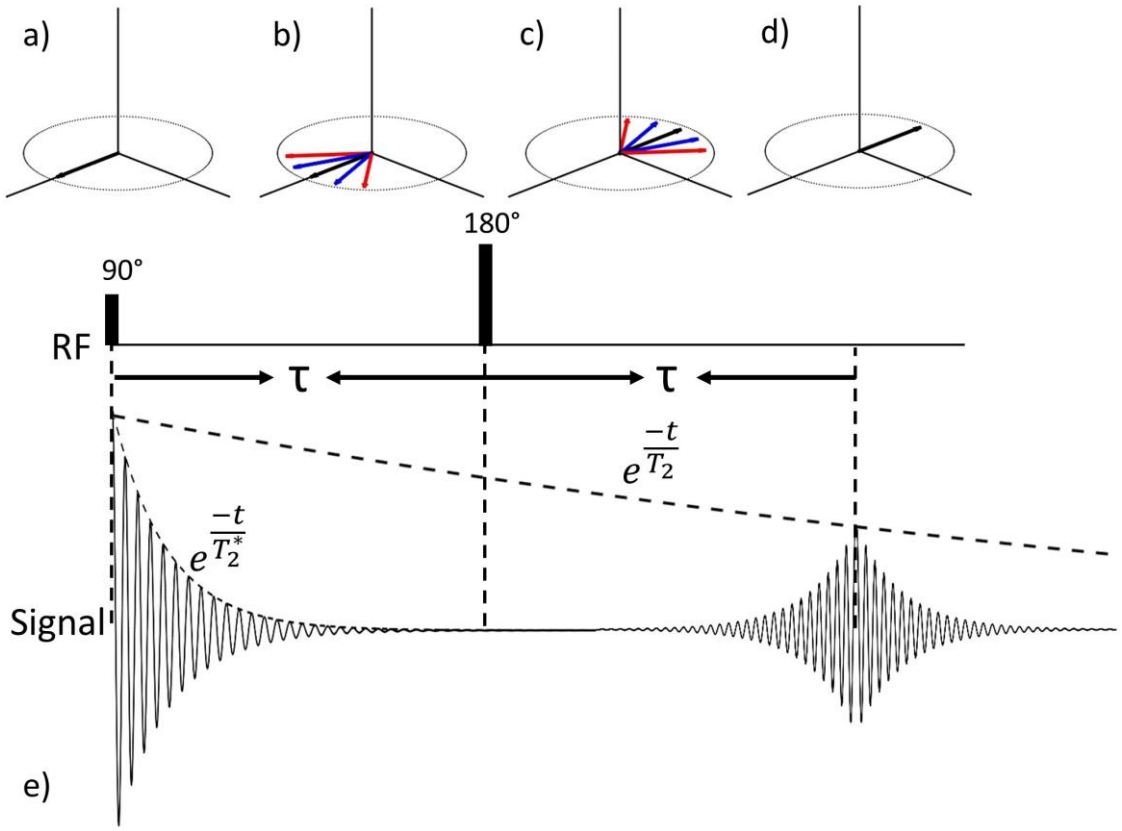

Figure 1.6. Diagram of spin-echo signal acquisition. a) Magnetization vectors immediately after excitation. b-c) Blue – Slightly off resonant spins, Red – Very off resonant spins b) Magnetization vectors before the 180° pulse. c) Magnetization vectors after the 180° pulse. d) Magnetization vectors at time 2τ. e) Pulse sequence diagram showing the signal decaying by T_2^* and being refocused to an amplitude determined by T_2.

frequencies, and thus allow them to be mapped to their source location with knowledge of the gradient's spatial strength. The easiest and most commonly used gradient is a 1D linear gradient. A linear gradient provides quick simple mapping of frequency to location. Nonlinear gradients have been investigated for use in MR imaging (31), though these methods require more complex reconstruction algorithms. When a gradient is applied along the x-direction, denoted as G_x, the strength of the magnetic field will vary along the x-direction. It is important to recognize that this is not a magnetic field pointing in the x-direction, rather it is still a magnetic field

pointing in the z-direction but the strength will vary along the x-direction. The methods of creating 2D and 3D images through the use of gradients is described in the following subsections.

1.3.1 Slice Excitation

The first step in localizing the signal, is to only excite a thin plane of spins. This is accomplished by turning on a magnetic gradient during the RF excitation pulse. The spatially varying frequency with the slice selection gradient is described by

$$\omega(z) = \omega_0 + \gamma G_z z \qquad [1.30]$$

where G_z is the gradients strength per distance along the z-direction and z is the position. In order to excite a slice at a specific location z with a thickness Δz, the frequency selectivity of the RF pulse needs to be specified so that the center frequency of the pulse is at the center of the slice z_0, $\omega_{rf} = \omega(z_o)$, and the RF pulse bandwidth corresponds with the desired slice thickness, Equation [1.33]. The RF excitation in the rotating frame is controlled by the envelope B_1^e as seen in Equations [1.20] and [1.23] As long as the desired flip angle is less the 90°, the profile of the slice excitation can be accurately described through the small angle approximation, also known as the Fourier transform approach (26). When the flip angle is larger, the Bloch equations must be solved to accurately describe the excitation characteristics. In general, the desired shape (profile p) of the excited slice is a rect function.

$$p(z) = \begin{cases} 1 & |z - z_0| < \Delta z/2 \\ 0 & otherwise \end{cases} \qquad [1.31]$$

It is well known that the Fourier transform of a rect function is a sinc function. For a desired slice thickness the envelope would have the following shape,

$$B_1^e(t) = A * sinc(\pi \Delta f t) \quad [1.32]$$

$$\Delta f = \frac{\gamma}{2\pi} G_z \Delta z \quad [1.33]$$

where A is the amplitude determined by the desired flip angle and Δf is the bandwidth. This sinc pulse is not possible in practice as it is infinite in length, and thus needs to be truncated. For a pulse of length τ_p, the envelope becomes

$$B_1^e(t) = A * sinc\left[\pi \Delta f \left(t - \frac{\tau_p}{2}\right)\right] \quad [1.34]$$

The resulting slice profile from the above shifted and truncated pulse (ignoring truncation effects) is

$$p(z) = \begin{cases} e^{i\gamma G_z (z - z_0)\tau_p/2} & |z - z_0| < \Delta z/2 \\ 0 & otherwise \end{cases} \quad [1.35]$$

Truncating the RF pulse produces an imperfect slice profile. To minimize the truncation effects, more sidelobes of the sinc pulse can be kept. The length of the pulse needed for n sidelobes is given by

$$\tau_p = \frac{4n\pi}{\gamma G_z \Delta z}. \quad [1.36]$$

The slice profile for an infinite sinc pulse is compared to a truncated pulse with 4 sidelobes in Figure 1.7a-b. Pulse truncation effects can also be minimized by multiplying the truncated pulse by a windowing function such as a Hamming window (32). The resulting slice profile is shown in Figure 1.7c. The effect of a given pulse on different gradient strengths is illustrated in Figure 1.8. Different gradients will excite spins in different locations and different slice thicknesses for the same RF pulse. The thinnest possible slice is limited by the maximum gradient strength available and the bandwidth of the RF pulse.

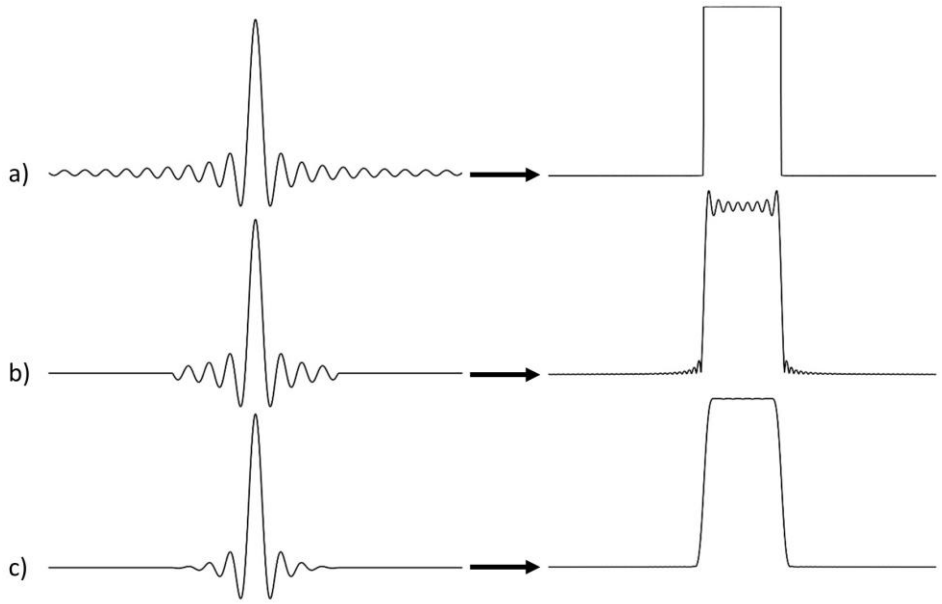

Figure 1.7. Pulse truncation effects. a) Infinite sinc pulse and its slice profile. b) Truncated sinc pulse with 4 sidelobes and its slice profile. c) Hamming windowed truncated sinc pulse with 4 sidelobes and its slice profile.

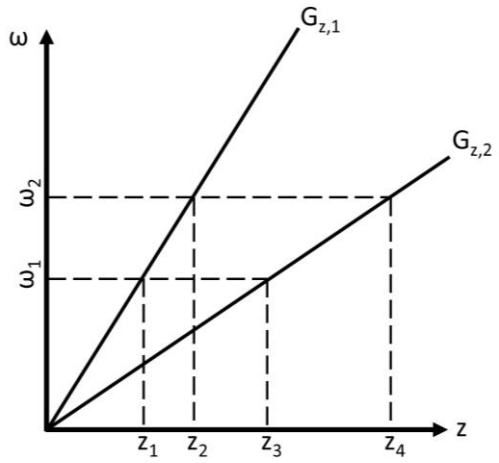

Figure 1.8. An RF pulse with a given bandwidth $\Delta\omega$. In the presence of $G_{z,1}$, a slice will be excited between $z_1 < z < z_2$, and in the presence of $G_{z,2}$, a slice will be excited between $z_3 < z < z_4$.

The slice select gradient will introduce a linear phase shift across the slice slice thickness as seen in Equation [1.35]. If it is not corrected, this phase shift will cause undesirable signal loss. The induced phase shift across the slice is related to the strength of the applied gradient and the time applied, and is given by

$$\Phi(z,\tau_p) = \int_0^{\frac{\tau_p}{2}} \gamma G_z(t)(z - z_0)dt. \quad [1.37]$$

Equation [1.37] is the area under the slice select gradient from the center of the pulse to the end. The phase shift is linear function of z. The spins across the slice can be rephrased by applying a gradient with the same area but opposite polarity.

1.3.2 Frequency Encoding

After the slice has been excited, the positions of spins within the slice need to be determined. This is done by applying a linear gradient along a direction, in this case the x-direction.

$$\omega(x) = \omega_0 + \gamma G_x x \quad [1.38]$$

The signal generated from a small region dx with spin density ρ(x), with the omission of the transverse relaxation effect, is

$$dS(x,t) = \rho(x)dxe^{-i\gamma(B_0+G_x x)t}. \quad [1.39]$$

$$dS(x,t) = \rho(x)dxe^{-i\gamma G_x xt}e^{-i\omega_0 t}. \quad [1.40]$$

The signal in Equation [1.40] is now frequency encoded, as the frequency of the signal depends on its position x. For the same reason, the gradient that produces the frequency encoding, in this case G_x, is called the frequency encoding gradient. After demodulating the signal by the carrier frequency ω_0, the total signal (ignoring receiver coil spatial sensitivity) is the summation over the entire excited region, which is the

integral of Equation [1.40]

$$S(t) = \int_{-\infty}^{\infty} \rho(x) e^{-i\gamma G_x x t} dx. \quad [1.41]$$

This type of encoding is only sufficient for imaging in one dimension. In order to create a 2D or 3D image, another kind of spatial encoding is necessary.

1.3.3 Phase Encoding

Phase encoding is similar to frequency encoding except that the gradient is played out before data acquisition. By applying the gradient for a short time before readout, the signal will acquire a specific phase based on its position. The phase encoding gradient is applied orthogonal to the frequency encoding direction, in this case, the y-direction. Similar to Equation [1.40], the signal after phase encoding is

$$dS(t) = \rho(y) dy e^{-i\gamma G_y y T_{PE}} e^{-i\omega_0 t} \quad [1.42]$$

where T_{PE} is the time the phase encoding gradient is turned on. After demodulating, the signal after phase encoding and during frequency encoding is

$$S(t) = \iint \rho(x,y) e^{-i\gamma G_y y T_{PE}} e^{-i\gamma G_x x t} dx dy \quad [1.43]$$

After the signal has been both frequency and phase encoded, every spin in a 2D plane can be localized due to its unique frequency and phase offset combination. Phase encoding can be performed along multiple directions. This allows for 3D imaging. The signal with two phase encoding directions is

$$S(t) = \iiint \rho(x,y,z) e^{-i\gamma G_y y T_{PE_y}} e^{-i\gamma G_z z T_{PE_z}} e^{-i\gamma G_x x t} dx dy dz \quad [1.44]$$

where T_{PE_y} is the time the y phase encoding is turned on, and T_{PE_z} is the time the z

phase encoding is turned on.

1.3.4 k-Space Formulation

It turns out that the acquired signal is actually in the spatial frequency domain of the object, known as k-space. This can be easily seen by making the substitution of the following variables

$$k_x = \frac{\gamma G_x t}{2\pi} \quad [1.45]$$

$$k_y = \frac{\gamma G_y T_{PE}}{2\pi} \quad [1.46]$$

Equation [1.43] then becomes

$$S(k_x, k_y) = \iint \rho(x, y) e^{-i2\pi(k_x x + k_y y)} dx dy. \quad [1.47]$$

The Fourier relationship between the encoded signal and the spin density function becomes obvious in Equation [1.47].

1.3.5 Sampling of k-Space

A simple, efficient way of viewing k-space sampling is to understand that the gradients move the data acquisition through k-space. This is shown in Figure 1.9. After the initial excitation RF pulse and slice rephrasing, the sampling position is at position 0, the center of k-space. Then the phase encoding gradient and readout prephasing gradient move the sampling position to position 1. The readout gradient is turned on to move towards position 2 and the signal is collected during the readout gradient using an analog to digital converter (ADC). This allows the acquisition of one line of k-space data after one excitation. In order to satisfy the sampling requirements to form a 2D

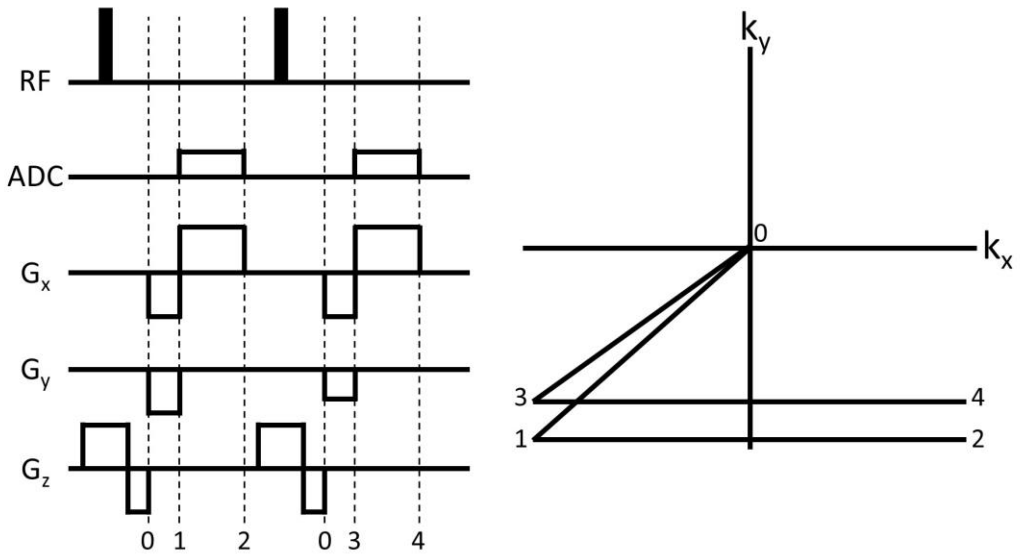

Figure 1.9. Pulse sequence timing diagram. After excitation, gradients move the sampling position of k-space.

image, the excitation is repeated where the phase encoding gradient is adjusted to begin the readout at location 3. This is repeated until a sufficient number of lines to reconstruct the image are acquired, which is described in Section 1.5.

1.4 Basic Pulse Sequences

This section will discuss some of the basic methods of acquiring k-space and their effects on image quality and contrast. One assumption made throughout this section is that the excitation occurs nearly instantaneously, meaning that no relaxation effects occur during excitation. For the following, TR (repetition time) is defined as the time between excitation pulses.

1.4.1 Gradient Echo

While a SE sequence uses gradient echoes in combination with a refocusing pulse, a sequence that only uses gradients to form the echoes are commonly referred

to as gradient recalled echo (GRE) sequences. The GRE does not use a refocusing pulse to refocus the spins. Instead, the spins are first dephased by a gradient, then all the dephasing done by the gradients is reversed by a gradient of opposite polarity as shown in Figure 1.10. The area of the first defocusing gradient must be equal to the area covered by the first half of the readout gradient in order to rephase the spins at the center of the readout. GRE sequences generally allow a shorter TE as no refocusing pulse is needed. Although the TE can be short, it is still weighted by the shorter T_2^*.

1.4.2 Spin-Echo

Phase encoding and readout gradients can be added to the pulse sequence diagram in Figure 1.6e allowing for the creation of an image that has been weighted by the T_2 and not T_2^* decay. Spin-echo (SE) sequences typically require a slightly longer TE, as time is required for the refocusing pulse.

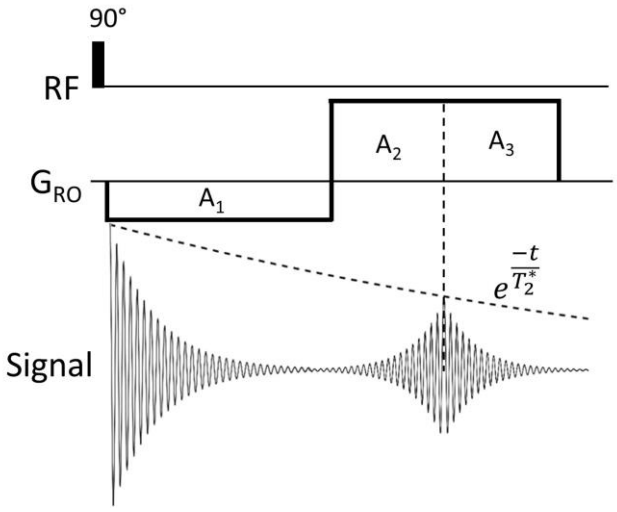

Figure 1.10. Gradient recalled echo timing diagram. The signal is refocused by a gradient area equal to the area of the defocusing gradient. $A_1 = A_2 = A_3$

1.4.3 Signal Contrast

Much of the information from this section is contained in Chapter 7 of (26). There are several factors that affect the signal strength of different tissue types. The first few factors are the three inherent properties of the tissue, proton density (PD), T_1 relaxation constant, and T_2 relaxation constant The other factors that affect signal strength, and therefore contrast, can be controlled by the imaging sequence and are the TR, TE, flip angle, voxel size, k-space trajectory, and type of pulse sequence used. Only the basic contrast options and how they are obtained will be discussed here. A simple definition of contrast is given as

$$C_{AB} = \frac{|S_A - S_B|}{S_A + S_B} \qquad [1.48]$$

where C_{AB} is the contrast between tissues A and B, and S_A and S_B are the signals from each tissue. In order to enhance image contrast, the differences in image intensity should be maximized. Image contrast is important, because the human eye has difficulty judging absolute intensity values, where a good example of this is shown in Figure 1.11. The main tissue property providing the largest weighting to the image contrast depends on the TE and TR values, and are displayed in Table 1.1. For

Figure 1.11. Example of visual illusion. The small squares in the middle have equal image intensity, but do not appear equally bright.

Table 1.1. Factors that determine signal weighting.

Weighting	TR Value	TE Value
T_1	<= T_1	<< T_2
T_2	>> T_1	>=T_2
PD	>> T_1	<<T_2

example, in order to obtain a T_1 weighted image the TR value must be larger than T_1 and the TE must be much shorter than T_2. Tissues with longer T_1, in a T_1 weighted image, will have lower signal. In a T_2 weighted image, tissues with shorter T_2 will have less signal. A PD weighted image will simply be brighter where there are more protons to produce signal. For any two tissue types, there is an optimal value of TE or TR to produce maximize contrast between the two tissues.

During most imaging methods, the inherent tissue properties, T_1, T_2, and PD, are constant, but it is possible to affect their properties in order to change the contrast. When a patient is injected with a contrast agent (33), the T_1 or T_2 relaxation constant of any tissues that absorb it will change depending on which contrast agent was injected. Different tissues will absorb at different rates. By acquiring images several times after injection, different contrast values can be obtained. This method is often used to make a tumor obvious in an image, as the surrounding tissue will absorb the contrast agent at a different rate, increasing the contrast between the tissue and tumor.

1.4.4 Echo Planar Imaging

The most significant portion of time required to acquire an image is in the phase encoding steps. Echo planar imaging (EPI) was developed to more rapidly acquire k-

space data. Instead of acquiring only one phase encoding line of k-space per TR, all or multiple lines can be acquired per TR. There are increased image artifacts when using EPI, but most of them can be overcome. A timing diagram is shown in Figure 1.12. After the first line is acquired and while the readout gradient is ramping down, the PE gradient is turned on for a short blip to move the phase encoding position to the start of the next line. The readout of the next line is done in the opposite direction. This is repeated until all the desired lines are acquired. This method allows for rapid acquisition of k-space. A single 2D slice image can be imaged several times per second.

One significant artifact that can arise from EPI readouts is due to the opposite readout directions. Inaccurate timing of the sampling relative to the switched gradient, or inhomogeneities in the static field cause phase errors and leads to ghosting in the phase encode direction. Ghosting artifacts will be discussed further in Section 1.5.3. These phase errors can be corrected by collecting at least two reference readouts without the phase encoding gradient before data acquisition. The reference scans can be used to estimate the timing error between the opposite directions and then adjust the phase of each k-space line to remove the offset. Another image artifact that is

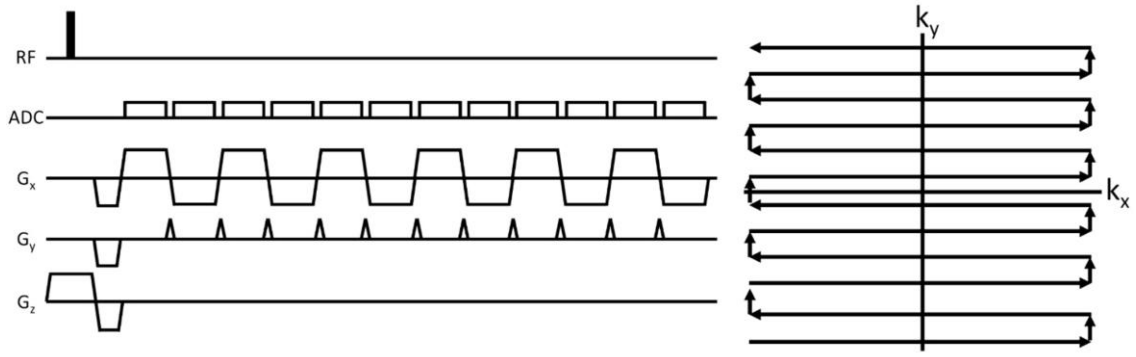

Figure 1.12. Timing diagram of EPI sequence. All lines of k-space are acquired during each TR.

produced through this method is due to the fact the entire sampling process needs to be completed on the order of T_2^*. The T_2^* decay while sampling along the PE direction leads to blurring in that direction. The blurring artifact in the PE direction can be reduced by spreading the acquisition over multiple TRs. This is referred to as a segmented EPI (seg-EPI) sequence. A seg-EPI sequence will typically interleave the acquisition of lines, as shown in Figure 1.13, instead of acquiring from top to bottom.

The next artifact that can cause problems is the chemical shift artifact. Chemical shift will be discussed further in Section 1.5.4. This artifact causes a shift in position between fat and water hydrogen. By reading in opposite directions, the shift changes directions between k-space lines, causing significant errors in the image domain. One solution is readout all lines in the same direction, as show in Figure 1.14. This will add a little time between readouts as the readout gradients must be completely unwound instead of being able to immediately begin reading again. This will cause the fat/water shift artifact to at least be in the same direction. Another option is to apply a fat saturation pulse before every TR (34) to remove any signal from fat tissue.

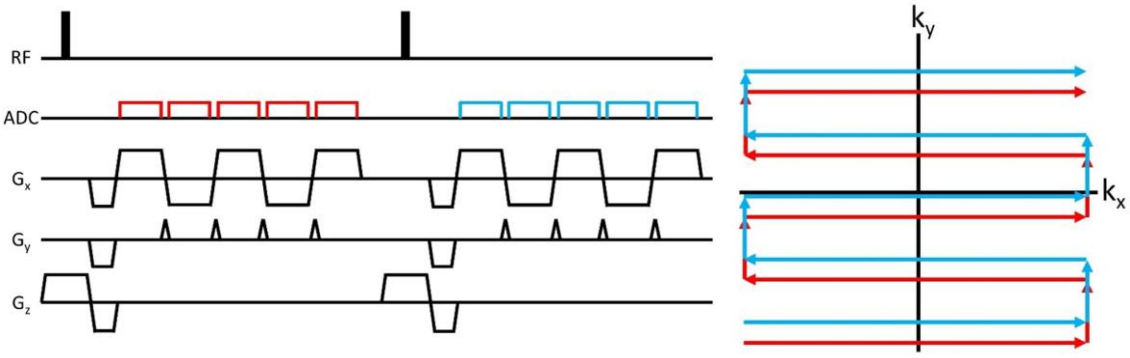

Figure 1.13. Timing diagram of seg-EPI sequence. Multiple lines of k-space are acquired during each TR. Lines are interleaved to reduce artifacts.

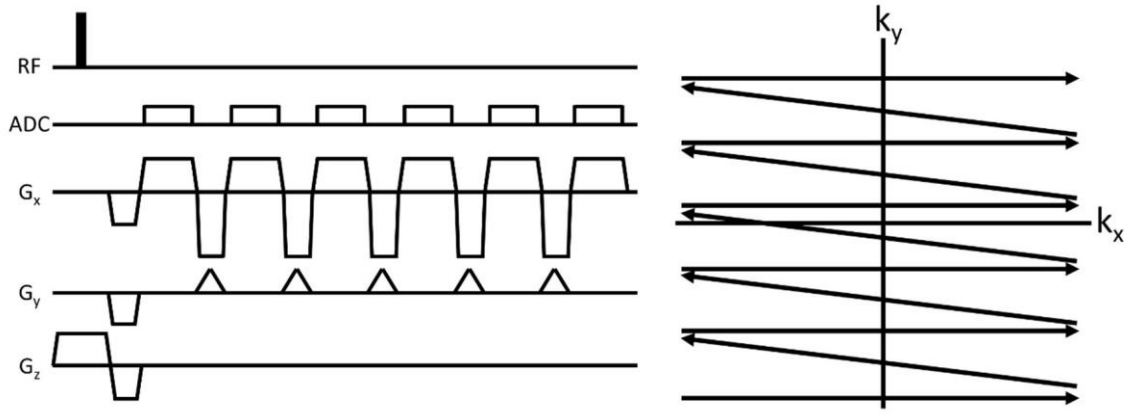

Figure 1.14 - Timing diagram of seg-EPI flyback sequence. Multiple lines of k-space are acquired in the same direction during each TR.

1.4.5 Radial (Non-Cartesian) Imaging

k-Space sampling is not limited to Cartesian trajectories. In fact, it can be sampled through any arbitrary trajectory. There are pros and cons to every trajectory. Cartesian trajectory offers simple reconstruction and easily understood artifacts. Non-Cartesian trajectories can offer efficient rapid coverage of k-space as well as robustness to motion. Reconstruction is more complicated, as discussed in Section 1.5.2, and produces different artifacts. Two commonly used non-Cartesian trajectories are radial (23,35) and spiral (9,36). Only the radial trajectory will be discussed here. Instead of turning on a phase encoding gradient before readout, both the G_x and G_y gradients can be turned on at the same time during readout. The overall gradient strength and angle θ are given by

$$G = \sqrt{G_x^2 + G_y^2} \text{ and } \theta = \arctan\left(\frac{G_y}{G_x}\right) \qquad [1.49]$$

In radial sampling, each line, now called radial views or projections, is a 1D profile of the object at the view angle θ. The k-space trajectory samples the center of k-space each TR. This offers robustness to motion, as the center is averaged many times. Averaging

the center also improves the signal to noise ratio (SNR) (37). A radial trajectory is compared to a Cartesian in Figure 1.15. Radial trajectories are also robust to large amounts of undersampling (38). Undersampling is when less k-space is acquired than meets the Nyquist criteria, which are given in Equations [1.62] and [1.63] (39).

Radial trajectories can either be acquired symmetrically or use any distribution of angles as desired. A popular angle to increment the view by is the golden angle (40). The golden angle is observed often in nature. It is related to the Fibonacci sequence and is equal to

$$\frac{360 - 180\left(3 - \sqrt{5}\right)}{2} \approx 111.2461° \qquad [1.50]$$

A golden angle distribution guarantees an optimal distribution for an arbitrary number of radial views (40). Radial sampling is discussed extensively in Chapter 7.

1.5 Image Reconstruction

The process of converting the raw k-space data to the image domain depends on how the k-space data was sampled. There are pros and cons to different methods, which can include the ease of reconstruction or the significance of image artifacts. This

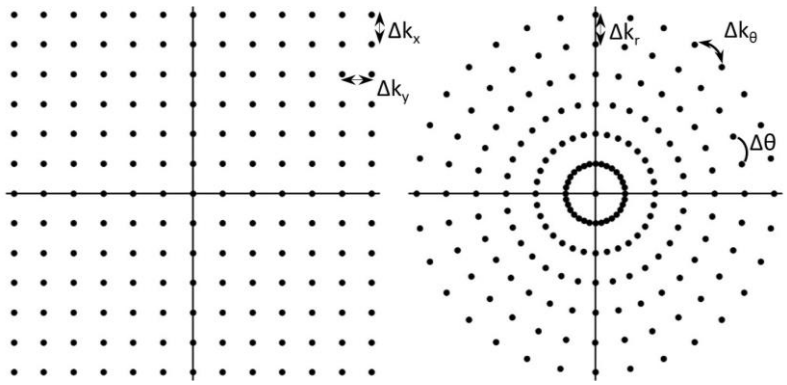

Figure 1.15. Cartesian vs. radial trajectory.

section discusses the prominent methods of image reconstruction as well as several of the most common image artifacts.

1.5.1 Cartesian Sampling

The most common form of sampling k-space is done with rectilinear Cartesian samples. The k-space signal equation for continuous sampling is given in Equation [1.47], which for a one-dimensional object is

$$S(k_x) = \int \rho(x) e^{-i2\pi k_x x} dx. \qquad [1.51]$$

The main problem in image reconstruction is how to obtain an accurate representation of $\rho(x)$ with a limited number of samples of $S(k_x)$. When uniformly sampling k-space, k_x can be replaced with $n\Delta k$, with n = …, -2, -1, 0, 1, 2, …

$$S[n] = S(n\Delta k) = \int \rho(x) e^{-i2\pi n \Delta k x} dx. \qquad [1.52]$$

The Fourier series of a finite object that is repeated with a period of $1/\Delta k$ is

$$\sum_{n=-\infty}^{\infty} S[n] e^{i2\pi n \Delta k \hat{x}} = \frac{1}{\Delta k} \sum_{n=-\infty}^{\infty} \rho\left(\hat{x} - \frac{n}{\Delta k}\right) \qquad [1.53]$$

where $\hat{x}$ are the reconstructed positions. As long as the object to be imaged is contained entirely within the imaged field of view (FOV), $|x| < FOV_x/2$, the object will not overlap with its periodic extension if $\Delta k < 1/FOV_x$. In this case, one period of the object can be accurately reconstructed from

$$\rho(\hat{x}) = \Delta k \sum_{n=-\infty}^{\infty} S[n] e^{i2\pi n \Delta k \hat{x}} \qquad [1.54]$$

An infinite number of samples is required to accurately reconstruct the object, which is clearly not feasible. In practice, a finite number of samples N are acquired:

$$\rho(\hat{x}) = \Delta k \sum_{n=-N/2}^{\frac{N}{2}-1} S[n] e^{i2\pi n \Delta k \hat{x}} \qquad [1.55]$$

Truncating the Fourier information leads to some inaccuracies in the reconstruction (41), such as the Gibbs ringing artifact, which is described further in Section 1.5.3. Truncation artifacts can be demonstrated by substituting the sampling Equation [1.52] into the reconstruction Equation [1.55].

$$\hat{\rho}(\hat{x}) = \Delta k \int \rho(x) \sum_{n=-N/2}^{\frac{N}{2}-1} e^{i2\pi n \Delta k (\hat{x}-x)} \, dx \qquad [1.56]$$

$$\hat{\rho}(\hat{x}) = \Delta k \int \rho(x) \, g(\hat{x} - x) dx \qquad [1.57]$$

Equation [1.57] shows that the reconstructed image is the original image convolved with the function $g(\hat{x} - x)$, which is known as the point spread function (PSF) and can be simplified to (26)

$$g(x) = \frac{\sin(\pi N \Delta k x)}{\sin(\pi \Delta k x)} e^{-i\pi \Delta k x} \qquad [1.58]$$

An example of the PSF is shown in Figure 1.16. The FOV in the image domain is the length of one period ($1/\Delta$k) and the Gibbs ringing comes from the convolution of the original object with the PSF.

Extending Equation [1.55] to 2D, the reconstructed image for Cartesian sampling is obtained by simply computing the inverse Fourier transform of the acquired k-space, which is

$$\rho(\hat{x}, \hat{y}) = \Delta k_x \Delta k_y \sum_{n=N_x/2}^{N_x/2-1} \sum_{m=N_y/2}^{N_y/2-1} S[k_{x,n}, k_{y,m}] e^{i2\pi (n \Delta k_x \hat{x} + m \Delta k_y \hat{y})}. \qquad [1.59]$$

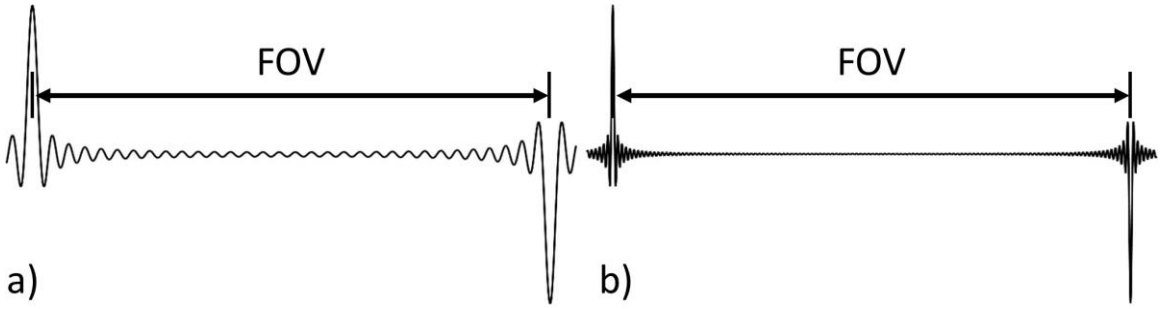

Figure 1.16. Point spread function with a) N = 64 and b) N = 256.

This is easily extended to three dimensions.

The reconstructed image will have a FOV and resolution that will depend on how much k-space was acquired. The FOV in the x and y directions are given by

$$FOV_x = N_x \Delta x = \frac{1}{\Delta k_x} \quad [1.60]$$

$$FOV_y = N_y \Delta y = \frac{1}{\Delta k_y} \quad [1.61]$$

where N_x and N_y are the number of sample points collected, Δx and Δy are the pixel sizes in the x and y directions, and Δk_x and Δk_y are the distances between k-space samples. The FOV in both directions is inversely proportional to the distance between k-space samples. The resolution is determined by how far out k-space is sampled.

$$\Delta x = \frac{1}{N_x \Delta k_x} \quad [1.62]$$

$$\Delta y = \frac{1}{N_y \Delta k_y} \quad [1.63]$$

Both the FOV and resolution are dependent on the distance between k-space samples, which for the readout (RO) and phase encoding (PE) directions are given by

$$\Delta k_{RO} = \frac{\gamma}{2\pi} |G_{RO}| \Delta t \quad [1.64]$$

$$\Delta k_{PE} = \frac{\gamma}{2\pi} |\Delta G_{PE}| T_{PE} \quad [1.65]$$

One difference between RO and PE directions that is evident from Equation [1.64], is that the distance between k-space samples in the RO direction is set by the time between ADC samples. This allows for the field of view in the RO direction to be as large or small as desired without any extra overall time required to sample.

1.5.2 Non-Cartesian Sampling

There are a few methods for reconstructing images from k-space that was not acquired on a Cartesian grid. The most basic method is to reconstruct using a back-projection reconstruction. In fact, the first MRI experiment was done using a projection reconstruction (23). Back-projection reconstruction requires the data to be sampled in a radial manner. For other k-space trajectories, the non-Cartesian data can be reconstructed using a demodulated point-by-point conjugate phase reconstruction (42). This provides an accurate reconstruction, but requires significant amounts of computation time. The most commonly used method is to interpolate the acquired k-space onto a grid and then simply compute the inverse Fourier transform (43). This process is commonly known as gridding. In the process of gridding, each sampled point is convolved with a convolution kernel at the nearby grid points and its contribution to that point is summed with the contribution from each convolved sample at that point. This method requires a sampling density correction to take into account the fact that k-space is not sampled uniformly (44). The main factors affecting the gridding reconstruction are the choice of convolution kernel, the density of the reconstruction grid, and the estimation of the sample density.

According to the sampling theorem, a signal can be reconstructed perfectly by convolving the signal with an infinite sinc function as long as the signal was sampled above the Nyquist frequency (45). Convolving with an infinite sinc is impossible in practice, so a different convolution kernel must be used. As convolution in the frequency domain is equivalent to multiplication in the spatial domain, any imperfect gridding kernel will produce apodization of the image intensity, mainly around the edges of the image. The most common convolution kernel is the Kaiser-Bessel function. The Kaiser-Bessel kernel provides a narrow apodization in image space, which reduces aliasing (46,47). The deapodization is done by simply dividing the image by the Fourier transform of the convolution kernel. The width of the convolution kernel determines the radius from each point to interpolate onto the grid. A larger kernel width will reduce gridding artifacts, but can significantly increase computation time (48).

The grid density on which to interpolate the original k-space data is arbitrary (48). This allows for great flexibility in the reconstruction. When the grid density is the same distance between sampled points, any aliasing artifacts from the convolution can easily be the same intensity of the apodized image at the edges of the image (48). This is obviously undesirable. By simply changing the grid density to be double the amount of grid points, the FOV is artificially doubled, as seen in Equation [1.60] where Δk is halved the FOV is doubled. This pushes any image artifacts and the heavier region of apodization to the now oversampled FOV, which can be simply cropped off. This also causes the aliased signal to be typically beneath the noise floor for most MRI images. Obviously, by increasing the gridding density, the memory requirements can be

significantly larger. For a simple 2D image with 2x oversampled gridding the memory requirements are 4 times larger. It has been shown that with the proper kernel and kernel width, oversampling factors as low as 1.25 are sufficient to drive any aliasing to be below the noise floor (48).

The density of sampled points must be taken into account in order to accurately reconstruct the image. For simple trajectories, like spirals and uniform radial, the density can be computed using simple geometry. The density of sampled points can be determined by simply calculating the area around each sample (49). Samples with high density will have smaller areas and therefore be weighted less individually. Density compensation is essentially an averaging process of the oversampled regions. The center of k-space is generally more oversampled and contains the low-frequency information. If it is not density corrected, significant blurring occurs in the image as seen in Figure 1.17.

1.5.3 Image Artifacts

There are many possible artifacts when acquiring MR images, and each will depend on the method of acquisition. There are several that are common between every imaging method. The simplest and most common is the Gibb's ringing artifact. Gibb's ringing occurs from the truncation of the Fourier series model (41). The ringing appears as variations in intensity parallel to a sharp intensity change in an image. The ringing artifact can be reduced by simply acquiring more k-space to a higher resolution as shown in Figure 1.16, or by applying a filter, such as the hamming window, to the k-space data. An example of Gibb's ringing is shown in Figure 1.18.

Another common artifact is aliasing. This occurs when the sampling

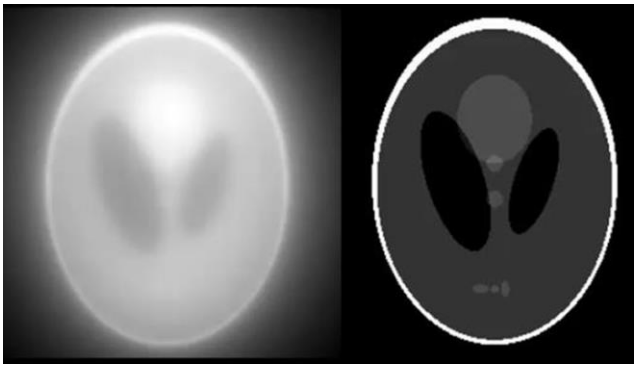

Figure 1.17. Example of density compensation effects. Left) Reconstructed image without density compensation has significant blurring. Right) Reconstructed image with density compensation.

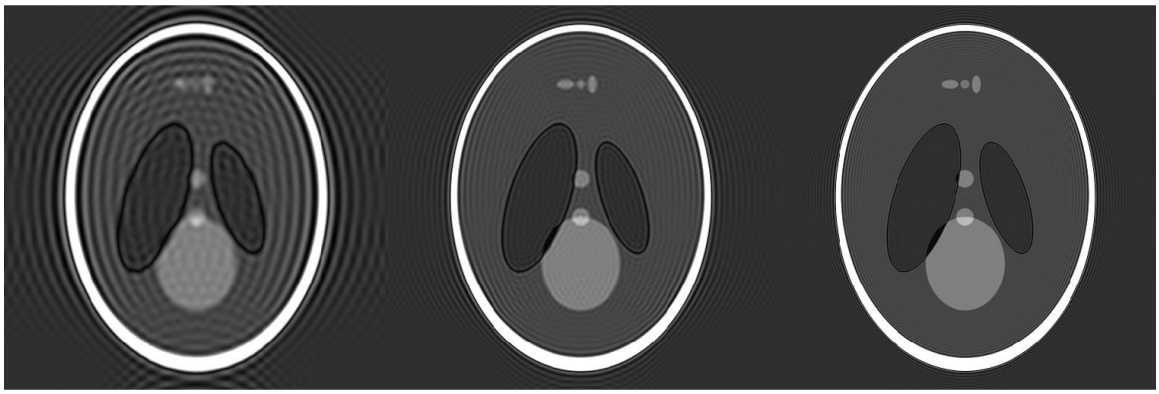

Figure 1.18. Example of Gibb's ringing. Left) Reconstructed image with 64 points along each direction. Middle) Reconstructed image with 128 points. Right) Reconstructed image with 256 points.

requirements to fully reconstruct an image are not met (50). The appearance of the aliasing artifact is strongly dependent on how sampling is done. For example, when the imaging field of view is undersampled in Cartesian imaging, the artifact appears as a wrap around of the image as shown in Figure 1.19. When imaging with radial projections, aliasing due to undersampling appears as a streaking artifact as shown in Figure 1.20.

Another very common artifact is the chemical shift artifact (50). Position in MRI is mapped using the frequency of hydrogen that can have slightly different frequencies depending on the environment the hydrogen is in. The most common chemical shift in MRI is the frequency difference between water and fat tissue. Water and fat have a chemical shift of 3.5 ppm, which at 3 T is equal to 440 Hz. This causes a misregistration in position of the fat. The shift in position is related to the frequency difference from water ($\Delta\omega_c$) and the frequency bandwidth of a pixel ($\Delta\omega_x$)

$$\delta_x = \frac{\Delta\omega_c}{\Delta\omega_x}. \qquad [1.66]$$

For example, for a readout bandwidth of 200 Hz/Px and the frequency shift of fat at

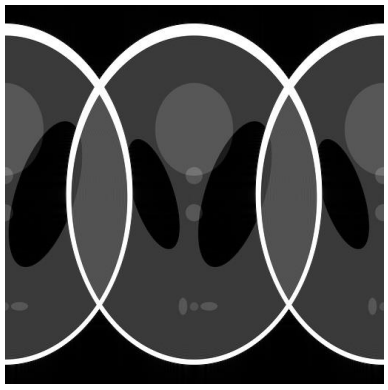

Figure 1.19. Aliasing artifact due to undersampling along the horizontal direction by a factor of 2.

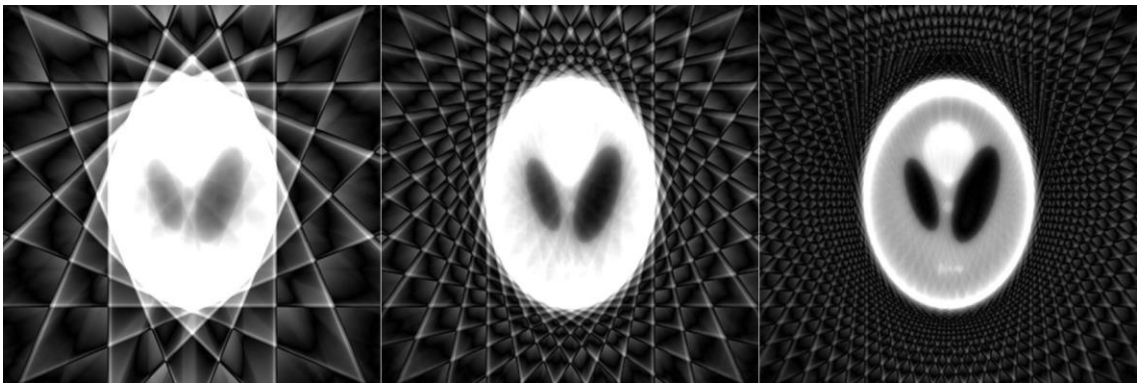

Figure 1.20. Simulated gridding reconstruction using radial projections taken uniformly from 0 to π for, Left) 8 projections, Middle) 16 projections, Right) 32 projections.

3 T (~440 Hz), the fat will be shifted 440/200 = 2.2 pixels (26). Standard imaging only exhibits the chemical shift in the readout direction, while EPI imaging has a very large chemical shift in the phase encoding direction due to the low bandwidth in the phase encoding direction. An example of chemical shift is shown in Figure 1.21. A region of artificial hyperintensity is seen in the direction the fat is shifted, while on the opposite side a dark band is seen where there is an artificial absence of signal.

Motion is a constant challenge in MRI and produces several different artifacts depending on the type (sudden or repeated) and severity of the motion (50,51). If the motion is small, simple image blurring can be seen. If the motion is repetitive and much larger, a ghosting artifact is present where multiple faint copies of the object can be seen. The artifact generated from motion, is also dependent on the k-space sampling trajectory. Projection MRI is typically motion robust because of the heavy oversampling of the center of k-space. Where severe ghosting would occur in a Cartesian acquisition, simple blurring would occur in a projection acquisition. In MR thermometry, motion can cause inaccurate temperature calculations, as well as

Figure 1.21. Example of chemical shift artifact. The position of fat is misregistered with respect to water due to a difference in frequency.

misregistration, which will be discussed in Chapter 5.

1.5.4 Water and Fat Separation

While the chemical shift artifact between fat and water is always present, it can be minimized effectively by increasing the sampling bandwidth to cause the shift to be a small fraction of a voxel. By acquiring images with appropriate TEs it becomes possible to generate water only and fat only images. The simplest method of generating these images is known as the three-point Dixon method (52). In the three-point Dixon method, images at 3 TEs are required, where the TEs must have the water and fat in phase, out of phase, then in phase again. At 3 T, these are at 2.46, 3.69, and 5.12 ms. When acquired at these TEs, the signal generated by these images is given by

$$\begin{aligned} m_1 &= \left(m_w + m_f\right) \\ m_2 &= \left(m_w - m_f\right)e^{i\Phi} \\ m_3 &= \left(m_w + m_f\right)e^{i2\Phi} \end{aligned} \qquad [1.67]$$

where m_n is the signal from the nth echo, m_w and m_f are the signals from water and fat, and Φ is the amount of phase accrued between the first and second images due to local field inhomogeneities and is referred to as the field map. The field map can be calculated using the first and third images by

$$2\hat{\phi} = \angle(m_1^* m_3) \qquad [1.68]$$

where $\hat{\phi}$ is the estimate of Φ, m_1^* is the complex conjugate of m_1 and $\angle$ is the angle operator. It is important to unwrap the estimate $2\hat{\phi}$ in order to ensure correct separation of water and fat (53). Water and fat images are acquired simply by correcting the off-resonance from the main field in the second image and then adding or subtracting the first two images and then averaging, as shown in the equations below. The three-point Dixon method is used in Chapters 5 and 7.

$$\begin{aligned} \hat{m}_w &= \frac{1}{2}\left(m_1 + m_2 e^{-i\hat{\phi}}\right) \\ \hat{m}_f &= \frac{1}{2}\left(m_1 - m_2 e^{-i\hat{\phi}}\right) \end{aligned} \qquad [1.69]$$

1.6 References

1. Furusawa H, Namba K, Thomsen S, Akiyama F, Bendet A, Tanaka C, Yasuda Y, Nakahara H. Magnetic resonance-guided focused ultrasound surgery of breast cancer: reliability and effectiveness. J Am Coll Surg 2006;203(1):54-63.

2. Kim YS, Bae DS, Kim BG, Lee JW, Kim TJ. A faster nonsurgical solution very large fibroid tumors yielded to a new ablation strategy. Am J Obstet Gynecol 2011;205(3):292 e291-295.

3. Sommer G, Bouley D, Gill H, Daniel B, Pauly KB, Diederich C. Focal ablation of prostate cancer: four roles for magnetic resonance imaging guidance. Can J Urol 2013;20(2):6672-6681.

4. Frenkel V, Etherington A, Greene M, Quijano J, Xie J, Hunter F, Dromi S, Li KC. Delivery of liposomal doxorubicin (Doxil) in a breast cancer tumor model:

investigation of potential enhancement by pulsed-high intensity focused ultrasound exposure. Acad Radiol 2006;13(4):469-479.

5. Rapoport N, Nam KH, Gupta R, Gao Z, Mohan P, Payne A, Todd N, Liu X, Kim T, Shea J, Scaife C, Parker DL, Jeong EK, Kennedy AM. Ultrasound-mediated tumor imaging and nanotherapy using drug loaded, block copolymer stabilized perfluorocarbon nanoemulsions. J Control Release 2011;153(1):4-15.

6. Kneidl B, Peller M, Winter G, Lindner LH, Hossann M. Thermosensitive liposomal drug delivery systems: state of the art review. Int J Nanomedicine 2014;9:4387-4398.

7. Elias WJ, Huss D, Voss T, Loomba J, Khaled M, Zadicario E, Frysinger RC, Sperling SA, Wylie S, Monteith SJ, Druzgal J, Shah BB, Harrison M, Wintermark M. A pilot study of focused ultrasound thalamotomy for essential tremor. N Engl J Med 2013;369(7):640-648.

8. Suffredini G, Levy LM. MR-guided, focused ultrasound: applications to essential tremor and other neurologic conditions. AJNR Am J Neuroradiol 2014;35(5):829-831.

9. Fielden S, Zhao L, Miller W, Feng X, Wintermark M, Pauly KB, Meyer C. Spiral-based 3D MR thermometry. J Ther Ultrasound 2015;3(1):P18.

10. Gallay MN, Moser D, Rossi F, Pourtehrani P, Magara AE, Kowalski M, Arnold A, Jeanmonod D. Incisionless transcranial MR-guided focused ultrasound in essential tremor: cerebellothalamic tractotomy. J Ther Ultrasound 2016;4:5.

11. Jolesz FA. MRI-guided focused ultrasound surgery. Annu Rev Med 2009;60:417-430.

12. Magara A, Buhler R, Moser D, Kowalski M, Pourtehrani P, Jeanmonod D. First experience with MR-guided focused ultrasound in the treatment of Parkinson's disease. J Ther Ultrasound 2014;2:11.

13. McDannold N, Clement GT, Black P, Jolesz F, Hynynen K. Transcranial magnetic resonance imaging- guided focused ultrasound surgery of brain tumors: initial findings in 3 patients. Neurosurgery 2010;66(2):323-332; discussion 332.

14. Medel R, Monteith SJ, Elias WJ, Eames M, Snell J, Sheehan JP, Wintermark M, Jolesz FA, Kassell NF. Magnetic resonance-guided focused ultrasound surgery: Part 2: A review of current and future applications. Neurosurgery 2012;71(4):755-763.

15. Schlesinger D, Benedict S, Diederich C, Gedroyc W, Klibanov A, Larner J. MR-guided focused ultrasound surgery, present and future. Med Phys 2013;40(8):080901.

16. Weintraub D, Elias WJ. The emerging role of transcranial magnetic resonance imaging-guided focused ultrasound in functional neurosurgery. Mov Disord 2016;32(1):20-27.

17. Todd N, Vyas U, de Bever J, Payne A, Parker DL. The effects of spatial sampling choices on MR temperature measurements. Magn Reson Med 2011;65(2):515-521.

18. Parker DL, Du YP, Davis WL. The voxel sensitivity function in fourier transform imaging: applications to magnetic resonance angiography. Magn Reson Med 1995;33(2):156-162.

19. Gerlach W, Stern O. Der experimentelle nachweis der richtungsquantelung im magnetfeld. Z Phys 1922;9(1):349-352.

20. Breit G, Rabi II. On the interpretation of present values of nuclear moments. Phys Rev 1934;46(3):230-231.

21. Bloch F, Hansen WW, Packard M. Nuclear induction. Phys Rev 1946;69(3-4):127-127.

22. Purcell EM, Torrey HC, Pound RV. Resonance absorption by nuclear magnetic moments in a solid. Phys Rev 1946;69(1-2):37-38.

23. Lauterbur PC. Image formation by induced local interactions: examples employing nuclear magnetic resonance. Nature 1973;242(5394):190-191.

24. Mansfield P. Multi-planar image formation using NMR spin echoes. Journal of Physics C: Solid State Physics 1977;10(3):L55.

25. Kumar A, Welti D, Ernst RR. NMR fourier zeugmatography. 1975. J Magn Reson 2011;213(2):495-509.

26. Liang Z-P, Lauterbur PC, IEEE Engineering in Medicine and Biology Society. Principles of magnetic resonance imaging : a signal processing perspective. Bellingham, Wash. New York: SPIE Optical Engineering Press ; IEEE Press; 2000. xv, 416 p.

27. Slichter CP. Principles of magnetic resonance. Berlin ; New York: Springer; 1996. xi, 655 p.

28. Redfield AG. On the theory of relaxation processes. IBM J Res Dev

1957;1(1):19-31.

29. Hahn EL. Spin echoes. Phys Rev 1950;80(4):580-594.

30. Frahm J, Merboldt KD, Hänicke W, Haase A. Stimulated echo imaging. J Magn Reson (1969) 1985;64(1):81-93.

31. Stockmann JP, Ciris PA, Galiana G, Tam L, Constable RT. O-space imaging: Highly efficient parallel imaging using second-order nonlinear fields as encoding gradients with no phase encoding. Magn Reson Med 2010;64(2):447-456.

32. Pauly J, Nishimura D, Macovski A. A k-space analysis of small-tip-angle excitation. J Magn Reson 2011;213(2):544-557.

33. Gustav JS, Willem JMM, Geralda AFvT, Klaas N. MRI Contrast agents: current status and future perspectives. Anticancer Agents Med Chem 2007;7(3):291-305.

34. Delfaut EM, Beltran J, Johnson G, Rousseau J, Marchandise X, Cotten A. Fat suppression in MR imaging: techniques and pitfalls. Radiographics 1999;19(2):373-382.

35. Block KT, Chandarana H, Milla S, Bruno M, Mulholland T, Fatterpekar G, Hagiwara M, Grimm R, Geppert C, Kiefer B, Sodickson DK. Towards routine clinical use of radial stack-of-stars 3D gradient-echo sequences for reducing motion sensitivity. J Korean Soc Magn Reson Med 2014;18(2):87-106.

36. Delattre BMA, Heidemann RM, Crowe LA, Vallée J-P, Hyacinthe J-N. Spiral demystified. Magn Reson Imaging;28(6):862-881.

37. Mosquera C, Irarrazabal P, Nishimura DG. Noise behavior in gridding reconstruction. 1995 9-12 May 1995. p 2281-2284 vol.2284.

38. Feng L, Axel L, Chandarana H, Block KT, Sodickson DK, Otazo R. XD-GRASP: Golden-angle radial MRI with reconstruction of extra motion-state dimensions using compressed sensing. Magn Reson Med 2016;75(2):775-788.

39. Griswold MA, Jakob PM, Heidemann RM, Nittka M, Jellus V, Wang J, Kiefer B, Haase A. Generalized autocalibrating partially parallel acquisitions (GRAPPA). Magn Reson Med 2002;47(6):1202-1210.

40. Winkelmann S, Schaeffter T, Koehler T, Eggers H, Doessel O. An optimal radial profile order based on the Golden Ratio for time-resolved MRI. IEEE Trans Med Imaging 2007;26(1):68-76.

41. Wood ML, Henkelman RM. Truncation artifacts in magnetic resonance imaging. Magn Reson Med 1985;2(6):517-526.

42. Noll DC, Fessler JA, Sutton BP. Conjugate phase MRI reconstruction with spatially variant sample density correction. IEEE Trans Med Imaging 2005;24(3):325-336.

43. Fessler JA, Sutton BP. Nonuniform fast Fourier transforms using min-max interpolation. IEEE Trans Sig Process 2003;51(2):560-574.

44. Pipe JG, Menon P. Sampling density compensation in MRI: Rationale and an iterative numerical solution. Magn Reson Med 1999;41(1):179-186.

45. Shannon CE. A mathematical theory of communication. The Bell System Technical Journal 1948;27(3):379-423.

46. Jackson JI, Meyer CH, Nishimura DG, Macovski A. Selection of a convolution function for Fourier inversion using gridding [computerised tomography application]. IEEE Trans Med Imaging 1991;10(3):473-478.

47. Sedarat H, Nishimura DG. On the optimality of the gridding reconstruction algorithm. IEEE Trans Med Imaging 2000;19(4):306-317.

48. Beatty PJ, Nishimura DG, Pauly JM. Rapid gridding reconstruction with a minimal oversampling ratio. IEEE Trans Med Imaging 2005;24(6):799-808.

49. Rasche V, Proksa R, Sinkus R, Bornert P, Eggers H. Resampling of data between arbitrary grids using convolution interpolation. IEEE Trans Med Imaging 1999;18(5):385-392.

50. Krupa K, Bekiesińska-Figatowska M. Artifacts in magnetic resonance imaging. Pol J Radiol 2015;80:93-106.

51. Wood ML, Henkelman RM. MR image artifacts from periodic motion. Med Phys 1985;12(2):143-151.

52. Dixon WT. Simple proton spectroscopic imaging. Radiology 1984;153(1):189-194.

53. Glover GH, Schneider E. Three-point Dixon technique for true water/fat decomposition with B0 inhomogeneity correction. Magn Reson Med 1991;18(2):371-383.

54. Pykett IL, Rzedzian RR. Instant images of the body by magnetic resonance. Magn Reson Med 1987;5(6):563-571.

55. Stark DD, Bradley WG. Magnetic resonance imaging. St. Louis: C.V. Mosby Co.; 1988. xxx, 1516 p. p.

56. Farzaneh F, Riederer SJ, Pelc NJ. Analysis of T2 limitations and off-resonance effects on spatial resolution and artifacts in echo-planar imaging. Magn Reson Med 1990;14(1):123-139.

57. Bydder GM. Clinical applications of contrast agents in body imaging. Top Magn Reson Imaging 1991;3(2):74-84.

58. Cohen MS, Weisskoff RM. Ultra-fast imaging. Magn Reson Imaging 1991;9(1):1-37.

59. Bruder H, Fischer H, Reinfelder HE, Schmitt F. Image reconstruction for echo planar imaging with nonequidistant k-space sampling. Magn Reson Med 1992;23(2):311-323.

60. Schomberg H, Timmer J. The gridding method for image reconstruction by Fourier transformation. IEEE Trans Med Imaging 1995;14(3):596-607.

61. Buonocore MH, Gao L. Ghost artifact reduction for echo planar imaging using image phase correction. Magn Reson Med 1997;38(1):89-100.

62. Haacke EM. Magnetic resonance imaging : physical principles and sequence design. New York: Wiley; 1999. xxvii, 914 p. p.

CHAPTER 2

MAGNETIC RESONANCE THERMOMETRY

2.1 Introduction

This chapter will provide the basic theories behind MR thermometry. Nearly every measurable parameter in MRI is temperature dependent to some degree. The T_1 relaxation constant (1-3), T_2 relaxation constant (4,5), and the proton resonance frequency (PRF) (6-8) are some of the most common measured parameters. The ability to measure the temperature dependence of many of the parameters with a level of confidence or in a short enough time that it can actually be used can be quite difficult. The typical methods for measuring each parameter will be presented and difficulties with each method will also be discussed.

2.2 T_1 Relaxation Time

The first method for measuring temperature dependence with MRI was published in 1983 and was based on the temperature dependence of the T_1 relaxation time (3). The T_1 relaxation mechanism is due to dipole interactions of molecules that arise from their translational and rotational motion, which is related to the correlation time (9). These translational and rotational motions are temperature dependent, and changes in the motion will be reflected in the change in T_1 relaxation time. The temperature dependence is linear over the small temperature ranges typically seen in

thermal therapies. The gold standard method of measuring T_1 is the inversion recovery method and is very time consuming (10). The magnetization is first inverted with a preparatory 180° pulse. This inversion does not create any signal in the transverse plane, but does induce T_1 relaxation. After the 180° preparatory pulse, the magnetization is described by the Bloch equation in Equation [1.22] with $M_z(0) = -M_z^0$, which is

$$M_z(t) = M_z^0\left(1 - 2e^{\frac{-t}{T_1}}\right). \quad [2.1]$$

The magnetization after an inversion time (TI) is

$$M_z(TI) = M_z^0\left(1 - 2e^{\frac{-TI}{T_1}}\right). \quad [2.2]$$

By varying the TI, the signal values will change depending on the T_1 of the object. By properly setting the TI, TI = $-T_1\ln(½)$, signal from tissues with specific T_1 values can be completely nulled. The simplest method of inversion recovery calculations of T_1, described in the rest of this paragraph, requires the magnetization to be fully relaxed before every inversion, meaning that the TR needs to be at least 5-6 times the length of the T_1 to be measured, which can typically be anywhere from 500-1500 ms. For the inversion recovery method, images are acquired for at least two TI. A two-parameter fit to Equation [2.1] is calculated for each pixel to acquire the T_1 relaxation constant. Acquiring a single readout line every 5 s TR would take over 10 min to acquire 128 phase encodes. This would require over 20 min to acquire two images with different TI. This is much too long for practical use. Even acquiring all the lines with an EPI readout would require 5 s for each TI dataset, which is still typically too long as several TI are required to accurately calculate T_1. The image quality will also suffer from the

EPI type acquisition (11). Other methods that are meant to decrease the time needed to gather the necessary data for T_1 calculation include Look-Locker (12), and modified Look-Locker inversion recovery (MOLLI) (13).

T_1 can also be measured using the variable flip angle (VFA) method (14), also known as the driven equilibrium single-pulse observation of T_1 (DESPOT-1) (15) method. The VFA method uses the spoiled steady state signal equation to calculate T_1. The steady state equation is derived from Equation [1.22] by calculating the magnetization after many RF pulses, where at the end of every TR any remaining transverse magnetization is spoiled (16) to remove any cross-talk between excitations. The longitudinal spoiled steady state magnetization is given by (14)

$$M_z = M_z^0 \frac{\left(1 - e^{\frac{-TR}{T_1}}\right)}{\left(1 - \cos\alpha\, e^{\frac{-TR}{T_1}}\right)} \qquad [2.3]$$

where α is the RF flip angle. The transverse magnetization in steady state is given by

$$M_{xy}(t) = M_z^0 \frac{\left(1 - e^{\frac{-TR}{T_1}}\right)\sin\alpha}{\left(1 - \cos\alpha\, e^{\frac{-TR}{T_1}}\right)} e^{\frac{-t}{T_2}}. \qquad [2.4]$$

Equation [2.4] can be linearized to have the following form

$$\frac{M_{xy}(t)}{\sin\alpha} = e^{\frac{-TR}{T_1}} \frac{M_{xy}(t)}{\tan\alpha} + M_z^0 \left(1 - e^{\frac{-TR}{T_1}}\right) e^{\frac{-t}{T_2}} \qquad [2.5]$$

After linearization, a simple linear fit of $\frac{M_{xy}(t)}{\sin\alpha}$ vs. $\frac{M_{xy}(t)}{\tan\alpha}$ can be calculated. T_1 is then calculated from the slope m of the fit

$$T_1 = \frac{-TR}{\ln m}. \qquad [2.6]$$

The accuracy of the T_1 estimate is increased with more flip angles, while the minimum

number of flip angles is obviously two. As shown in Equation [2.4], the signal at steady state is dependent on the flip angle used. By taking the derivative of Equation [2.4] with respect to the flip angle α and setting equal to zero, it can be shown that the maximum signal is obtained when (17)

$$\alpha = \arccos\left(e^{\frac{-TR}{T_1}}\right). \qquad [2.7]$$

The angle that gives maximum signal in a spoiled steady state sequence is known as the Ernst angle (17). It has been shown through propagation of errors (18) that by using the two angles that provide approximately 70% of the maximum signal on either side of the Ernst angle, the estimation error in T1 is minimized.

There are several difficulties involved with the VFA method. The first difficulty comes from inhomogeneity in the B_1 excitation throughout the excited volume. Due to differences in tissue susceptibility or abrupt changes in susceptibility, such as an air/tissue interface, the RF pulse is not homogeneous over the excited volume. This means that some regions will experience a different flip angle than desired. It is possible to map and account for the RF inhomogeneity (19). Another difficulty is the slice profile. Spins across the slice profile experience a flip angle that varies from zero to the desired angle and back to zero, giving a wide variation in flip angle within each single voxel. This becomes especially problematic in 2D imaging as the edges of the profile can contribute significant signal that has a different flip angle, which leads to errors in the T_1 measurement (20). The slice profile problem is discussed extensively in Chapter 4. The slice profile is less of a problem in 3D imaging as only the edge slices will experience the lower flip angle due to the profile.

It is possible to measure temperature changes through the change in signal

magnitude, which is directly related to the changes in T_1. If the T_1 temperature dependence is linear, the exponential term in Equation [2.4] can be rewritten as

$$E_1 = \exp\left[\frac{-TR}{T_1(T_{ref}) + m(T - T_{ref})}\right] \quad [2.8]$$

where T_{ref} is the reference temperature. Both M_0 and T_1 are temperature dependent and both of their contributions must be taken into account when considering the temperature dependence of the signal. The signal decreases with temperature because both the relaxation time increases and the magnetization decreases. The relative temperature sensitivity of the magnitude dS/SdT is related to the rate of signal change with relaxation and change in equilibrium magnetization by the following equation (21)

$$\frac{dS}{dT} = m \cdot \frac{dS}{dT_1} - \frac{S}{T} \quad [2.9]$$

where S is the signal magnetization, T is the temperature, and $m = dT_1/dT$. The temperature dependence of T_1 must be determined empirically for each tissue (22). The second term on the right-hand side represents the decrease in equilibrium magnetization with increasing temperature as shown in Equation [1.10]. Using Equations [2.4] and [2.9] the temperature sensitivity (at the reference temperature, T_{ref}) is given by (21)

$$\frac{dS}{SdT} = -\frac{mTR(1-\cos\alpha)E_1}{\left(T_1(T_{ref})\right)^2(1-E_1)(1-\cos\alpha\, E_1)} - \frac{1}{T_{ref}}. \quad [2.10]$$

This approach to measuring T1 dependent signal changes has the advantage that a standard imaging sequence can be used, and is discussed further in Chapter 7. This can greatly increase the SNR and temporal resolution of temperature changes.

No matter how the change of T_1 is measured, a number of challenges remain in order to use T_1 to map temperature. The temperature dependence is tissue dependent and empirical calibration of the T_1 value vs. temperature is necessary for every tissue type. Ultrasound ablation causes irreversible changes to tissue properties (23,24), as well as irreversible changes to T_1 (25). Partial volume effects can also lead to inaccurate temperature measurements when the voxel size is large enough to have a strong temperature gradient across the voxel (26). Partial volume effects when a voxel contains two different tissue types with differing T_1 temperature dependence can also be a problem.

2.3 T_2 Relaxation Time

The T_2 relaxation time also changes with temperature, where much of the theoretical nature on T_2 is given in Chapters 2 and 5 of (27), as well as in (28). Similar to T_1 measurements, measurements of the T_2 relaxation time can be time consuming. In order to accurately measure T_2, signal must be acquired with a minimum of two TEs and then either fit the exponential or linearly fit the natural log of the signal. A spin-echo sequence must be used to measure T_2 instead of T_2^*, as described in Section 1.2.4. Measuring the T_2 dependence on signal change can be difficult, as its effects can easily be masked by other factors such as the T_1 change. As T_2^* is based on the T_2 value, it could possibly be used as a measure of temperature as well. T_2^* also depends on the local field inhomogeneity, Equation [1.30]. If there is a large temperature gradient across the voxel, intra-voxel dephasing can be significant and will cause a decrease in the measured T_2^*, while the underlying T_2 is increasing. This makes T_2^* temperature measurements less reliable and would at least require high resolution to minimize the

intra-voxel dephasing.

It has been shown that the T_2 temperature dependence is linear in adipose tissue over a small range of temperatures from 25 to 45 °C (4). As T_2 measurements require more time to collect, the use of T_2 based temperature measurements have mainly been focused on monitoring near field heating (4,5), where T_2 measurements would be made between sonications to monitor near field adipose tissue heating. As long as tissue damage and coagulation hasn't occurred, the T_2 change is reversible (29). This can be a characteristic of irreversible tissue damage and provide a measure of monitoring tissue damage.

2.4 Proton Resonance Frequency Shift

The temperature dependence of the proton resonance frequency (PRF) was first observed by Hindman in 1966 (7) while studying the intermolecular forces and hydrogen bond formation between water molecules. It was adapted for MR thermometry by Ishihara et al. (8) and De Poorter et al. (6). The magnetic field that a nucleus experiences can be written as

$$B_{loc} = (1 - s)B_0 \qquad [2.11]$$

where s is the shielding constant. As a result of any shielding from the nucleus' environment the resonance frequency of the nucleus will shift and become

$$\omega = \gamma B_0(1 - s). \qquad [2.12]$$

When an H_2O molecule is hydrogen bonded to another H_2O the shielding by the electron cloud is lower than if the H_2O molecule were free. The nature of the hydrogen bonds in water varies with temperature (30). As the temperature increases, the hydrogen bonds bend (7) and break (31) and as a result the molecules spend less time

bonded. This means that the screening increases and the resonance frequency decreases. The temperature dependent nature of the electron shielding is linear over a wide range in temperatures from -15 to 100 °C (7).

MR temperature maps using the PRF shift method are generated from the phase information of the images. After excitation, local B_0 inhomogeneities will cause the phase to change linearly with time. In order to remove the phase changes due to B_0 inhomogeneities and single out the differences due to temperature, a reference phase map is subtracted from the current phase map. The phase difference images are proportional to the temperature dependent PRF shift and the TE and can be converted to a temperature map by

$$\Delta T = \frac{\Phi(T) - \Phi(T_0)}{\alpha \gamma B_0 TE} \qquad [2.13]$$

where $\Phi(T)$ is the phase of the current image, $\Phi(T_0)$ is the phase of the reference image at a known temperature, and α is the PRF coefficient that relates the change in frequency to temperature. An example of phase difference images are shown in Figure 2.1. Except for adipose tissue, the PRF coefficient has been shown to be tissue independent (32). Calibration experiments have been performed for many tissue types and have found values ranging from -0.009 and -0.01 ppm/°C (32), which agrees with the value, -0.01 ppm/°C for pure water (21). The PRF shift is based on the shielding changing due to the amount of time spent hydrogen bonded changing. Adipose (fatty) tissue does not exhibit hydrogen bonding and therefore does not exhibit any frequency shift with temperature. This limits the PRF method to nonadipose tissue.

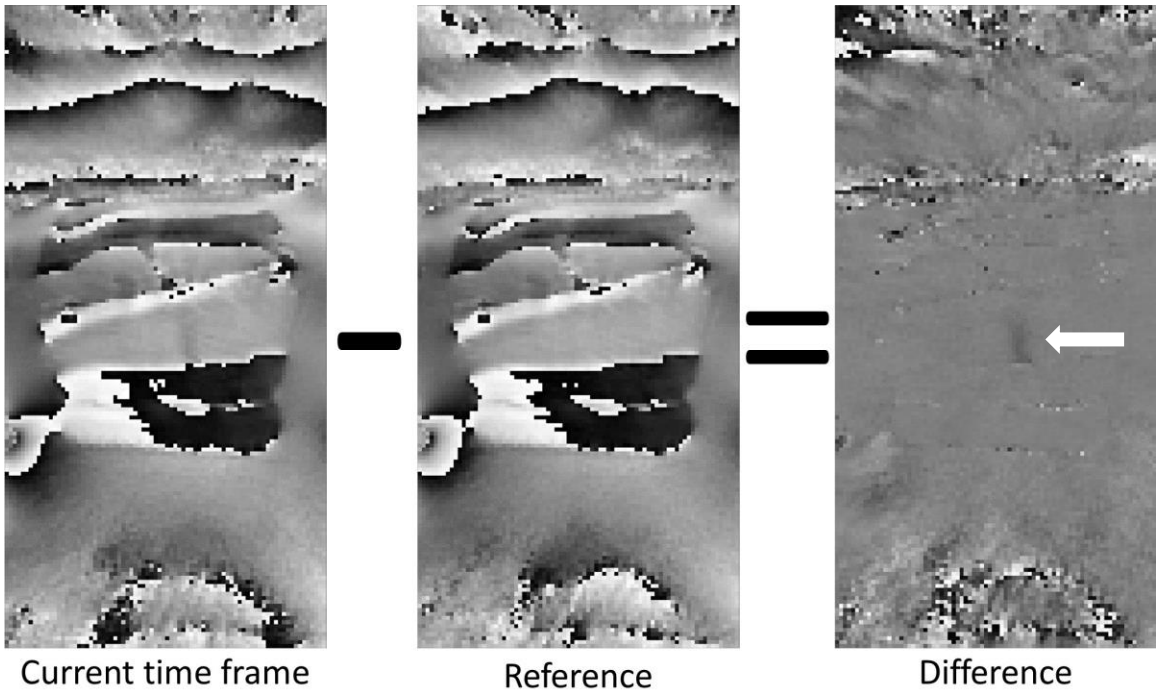

Figure 2.1. Phase images from the current time frame during heating and from a reference time before heating. The phase difference is proportional to the temperature change. The arrow indicates the location of the temperature increase.

2.4.1 Factors Affecting PRF Accuracy

According to Equation [2.13] the temperature measurements depend on the TE of the acquired images. The TE can be optimized to increase the SNR of the temperature measurements. The temperature dependent phase difference $SNR_{\Delta\Phi}$, is estimated by

$$SNR_{\Delta\Phi} = \frac{|\Delta\Phi|}{\sigma_{\Delta\Phi}} \qquad [2.14]$$

where $\Delta\Phi$ is the phase difference and $\sigma_{\Delta\Phi}$ is the standard deviation of the phase difference image. The standard deviation of the phase is equal to (33)

$$\sigma_{\Delta\Phi} = \frac{\sigma}{M} \qquad [2.15]$$

where σ is the standard deviation of the magnitude and M is the signal magnitude.

This means that the SNR is directly proportional to the signal intensity

$$SNR_{\Delta\Phi} \propto |\Delta\Phi| \cdot M \quad [2.16]$$

As the phase shift increases linearly with TE and the magnitude decays exponentially with time constant T_2^*, the SNR's dependence on the TE can be written as

$$SNR_{\Delta\Phi} \propto TE e^{-\frac{TE}{T_2^*}}. \quad [2.17]$$

Differentiating Equation [2.17] with respect to TE gives the optimal TE for the best temperature phase difference measurement to be $TE=T_2^*$ (34).

The PRF temperature method equates any phase change with a temperature difference. This means that any artifacts present in the phase images will cause errors in the temperature measurements. A common source of error is main field drift. The strength of the main magnetic field drifts slowly over time, changing the resonant frequency a few Hertz per minute (35). This will cause the calculated temperature to drift a few degrees Celsius (°C) over treatments lasting a few minutes. The external field drift can be measured and corrected using phase navigator readouts (36). Another common source of phase errors comes from respiration motion. Even when motion occurs outside the imaging volume, the change in the distribution of susceptible material will cause the local field within the imaging volume to change. This will cause artifacts in the temperature measurements. It is possible to measure and correct the phase offsets due to respiration through the use of multi-baseline libraries (37-39), with navigator readouts (36), or self-navigation (40,41).

The next most common difficulty is motion within the imaging volume itself. Motion will cause ghosting artifacts and misregistration of position. Both will cause errors in temperature measurements. This is especially problematic when targeting

anything in the central region of the body (e.g., liver) where diaphragm motion is constant. One solution is to use a pencil navigator to measure the position of the diaphragm and create a multibaseline library based on that motion to use a baseline phase that had the diaphragm in the same position (42,43).

The spatial and temporal resolutions play a considerable role in the accuracy of temperature measurements. Trade-offs must be made between SNR, spatial resolution, temporal resolution and FOV. There has been a lot of work into improving the temporal resolution while not sacrificing SNR (44,45).

2.5 References

1. Bottomley PA, Foster TH, Argersinger RE, Pfeifer LM. A review of normal tissue hydrogen NMR relaxation times and relaxation mechanisms from 1-100 MHz: dependence on tissue type, NMR frequency, temperature, species, excision, and age. Med Phys 1984;11(4):425-448.

2. Cline HE, Hynynen K, Hardy CJ, Watkins RD, Schenck JF, Jolesz FA. MR temperature mapping of focused ultrasound surgery. Magn Reson Med 1994;31(6):628-636.

3. Parker DL. Applications of NMR imaging in hyperthermia: an evaluation of the potential for localized tissue heating and noninvasive temperature monitoring. IEEE Trans Biomed Eng 1984;31(1):161-167.

4. Baron P, Ries M, Deckers R, de Greef M, Tanttu J, Kohler M, Viergever MA, Moonen CT, Bartels LW. In vivo T2 -based MR thermometry in adipose tissue layers for high-intensity focused ultrasound near-field monitoring. Magn Reson Med 2014;72(4):1057-1064.

5. Ozhinsky E, Kohi MP, Ghanouni P, Rieke V. T2-based temperature monitoring in abdominal fat during MR-guided focused ultrasound treatment of patients with uterine fibroids. J Ther Ultrasound 2015;3:15.

6. De Poorter J, De Wagter C, De Deene Y, Thomsen C, Stahlberg F, Achten E. Noninvasive MRI thermometry with the proton resonance frequency (PRF) method: in vivo results in human muscle. Magn Reson Med 1995;33(1):74-81.

7. Hindman JC. Proton resonance shift of water in the gas and liquid states. J

Chem Phys 1966;44(12):4582-4592.

8. Ishihara Y, Calderon A, Watanabe H, Okamoto K, Suzuki Y, Kuroda K, Suzuki Y. A precise and fast temperature mapping using water proton chemical shift. Magn Reson Med 1995;34(6):814-823.

9. Bloembergen N, Purcell EM, Pound RV. Relaxation effects in nuclear magnetic resonance absorption. Phys Rev 1948;73(7):679-712.

10. Bydder GM, Young IR. MR imaging: clinical use of the inversion recovery sequence. J Comput Assist Tomogr 1985;9(4):659-675.

11. Reeder SB, Atalar E, Bolster BD, McVeigh ER. Quantification and reduction of ghosting artifacts in interleaved echo-planar imaging. Magn Reson Med 1997;38(3):429-439.

12. Karlsson M, Nordell B. Phantom and in vivo study of the Look-Locher T1 mapping method. Magn Reson Imaging 1999;17(10):1481-1488.

13. Messroghli DR, Radjenovic A, Kozerke S, Higgins DM, Sivananthan MU, Ridgway JP. Modified Look-Locker inversion recovery (MOLLI) for high-resolution T1 mapping of the heart. Magn Reson Med 2004;52(1):141-146.

14. Fram EK, Herfkens RJ, Johnson GA, Glover GH, Karis JP, Shimakawa A, Perkins TG, Pelc NJ. Rapid calculation of T1 using variable flip angle gradient refocused imaging. Magn Reson Imaging 1987;5(3):201-208.

15. Homer J, Beevers MS. Driven-equilibrium single-pulse observation of T1 relaxation. A reevaluation of a rapid "new" method for determining NMR spin-lattice relaxation times. J Magn Reson (1969) 1985;63(2):287-297.

16. Zur Y, Wood ML, Neuringer LJ. Spoiling of transverse magnetization in steady-state sequences. Magn Reson Med 1991;21(2):251-263.

17. Ernst RR, Anderson WA. Application of fourier transform spectroscopy to magnetic resonance. Rev Sci Instrum 1966;37(1):93-102.

18. Matthias CS, Glen RM. Uncertainty in T 1 mapping using the variable flip angle method with two flip angles. Phys Med Biol 2009;54(1):N1.

19. Deoni SC. Correction of main and transmit magnetic field (B0 and B1) inhomogeneity effects in multicomponent-driven equilibrium single-pulse observation of T1 and T2. Magn Reson Med 2011;65(4):1021-1035.

20. Svedin BT, Parker D. The effect of 2D excitation profile on T1 measurement accuracy using the variable flip angle method. In Proceedings of the 22nd

Annual Meeting of ISMRM, Milan, Italy, 2014. p. 1475.

21. Rieke V, Butts Pauly K. MR thermometry. J Magn Reson Imaging 2008;27(2):376-390.

22. Cline HE, Schenck JF, Watkins RD, Hynynen K, Jolesz FA. Magnetic resonance-guided thermal surgery. Magn Reson Med 1993;30(1):98-106.

23. Graham SJ, Stanisz GJ, Kecojevic A, Bronskill MJ, Henkelman RM. Analysis of changes in MR properties of tissues after heat treatment. Magn Reson Med 1999;42(6):1061-1071.

24. Merckel LG, Deckers R, Baron P, Bleys RLAW, van Diest PJ, Moonen CTW, Mali WPTM, van den Bosch MAAJ, Bartels LW. The effects of magnetic resonance imaging-guided high-intensity focused ultrasound ablation on human cadaver breast tissue. Eur J Pharmacol 2013;717(1–3):21-30.

25. Diakite M, Payne A, Todd N, Parker DL. Irreversible change in the T1 temperature dependence with thermal dose using the proton resonance frequency-T1 technique. Magn Reson Med 2013;69(4):1122-1130.

26. Todd N, Vyas U, de Bever J, Payne A, Parker DL. The effects of spatial sampling choices on MR temperature measurements. Magn Reson Med 2011;65(2):515-521.

27. Slichter CP. Principles of magnetic resonance. Berlin ; New York: Springer; 1996. xi, 655 p.

28. Redfield AG. On the theory of relaxation processes. IBM J Res Dev 1957;1(1):19-31.

29. Graham SJ, Bronskill MJ, Henkelman RM. Time and temperature dependence of MR parameters during thermal coagulation of ex vivo rabbit muscle. Magn Reson Med 1998;39(2):198-203.

30. Némethy G, Scheraga HA. The structure of water and hydrophobic bonding in proteins. 1. the thermodynamic properties of hydrophobic bonds in proteins. J Phys Chem 1962;66(10):1773-1789.

31. Schneider WG, Bernstein HJ, Pople JA. Proton magnetic resonance chemical shift of free (gaseous) and associated (liquid) hydride molecules. J Chem Phys 1958;28(4):601-607.

32. McDannold N. Quantitative MRI-based temperature mapping based on the proton resonant frequency shift: review of validation studies. Int J Hyperthermia 2005;21(6):533-546.

33. Gudbjartsson H, Patz S. The rician distribution of noisy MRI data. Magn Reson Med 1995;34(6):910-914.

34. Cline HE, Hynynen K, Schneider E, Hardy CJ, Maier SE, Watkins RD, Jolesz FA. Simultaneous magnetic resonance phase and magnitude temperature maps in muscle. Magn Reson Med 1996;35(3):309-315.

35. Dadakova T, Krafft, A. J., Korvink, J. G., Meckel, S., Bock, M. PRF thermometry for monitoring small temperature changes during very long thermal therapies: field drift compensation using FID navigators. In Proceedings of the 24th Annual Meeting of ISMRM, Singapore, 2016. p. 3600.

36. Svedin BT, Payne A, Parker DL. Respiration artifact correction in three-dimensional proton resonance frequency MR thermometry using phase navigators. Magn Reson Med 2015.

37. Hey S, Maclair G, de Senneville BD, Lepetit-Coiffe M, Berber Y, Kohler MO, Quesson B, Moonen CT, Ries M. Online correction of respiratory-induced field disturbances for continuous MR-thermometry in the breast. Magn Reson Med 2009;61(6):1494-1499.

38. Shmatukha AV, Bakker CJ. Correction of proton resonance frequency shift temperature maps for magnetic field disturbances caused by breathing. Phys Med Biol 2006;51(18):4689-4705.

39. Vigen KK, Daniel BL, Pauly JM, Butts K. Triggered, navigated, multi-baseline method for proton resonance frequency temperature mapping with respiratory motion. Magn Reson Med 2003;50(5):1003-1010.

40. Durand E, van de Moortele PF, Pachot-Clouard M, Le Bihan D. Artifact due to B(0) fluctuations in fMRI: correction using the k-space central line. Magn Reson Med 2001;46(1):198-201.

41. Le TH, Hu X. Retrospective estimation and correction of physiological artifacts in fMRI by direct extraction of physiological activity from MR data. Magn Reson Med 1996;35(3):290-298.

42. Ehman RL, Felmlee JP. Adaptive technique for high-definition MR imaging of moving structures. Radiology 1989;173(1):255-263.

43. Hu X, Kim SG. Reduction of signal fluctuation in functional MRI using navigator echoes. Magn Reson Med 1994;31(5):495-503.

44. Griswold MA, Jakob PM, Heidemann RM, Nittka M, Jellus V, Wang J, Kiefer B, Haase A. Generalized autocalibrating partially parallel acquisitions (GRAPPA). Magn Reson Med 2002;47(6):1202-1210.

45. Todd N, Adluru G, Payne A, DiBella EV, Parker D. Temporally constrained reconstruction applied to MRI temperature data. Magn Reson Med 2009;62(2):406-419.

CHAPTER 3

FOCUSED ULTRASOUND

3.1 Introduction

This chapter will provide the basic principles and theoretical basis behind high-intensity focused ultrasound (HIFU) also referred to as focused ultrasound (FUS) (1). HIFU has the unique ability to heat very localized regions within the body completely noninvasively. The ability for HIFU to treat patients with low impact and quick recovery time makes it ideal for treatment of certain cancers, including the uterus, liver, kidney, pancreas, bone, breast, prostate, and brain (2-10). It has also had success in treating essential tremor and Parkinsons disease (11). The noninvasive nature of HIFU and the fact that it utilizes no ionizing radiation mean that multiple treatments are possible without an accumulated radiation dose. HIFU has the ability to deliver large amounts of energy to a very localized region within a short amount of time. MRI has been utilized to successfully plan and monitor treatments and when combined is referred to as MR-guided HIFU (MRgHIFU or MRgFUS). MRI provides the ability to visualize where the FUS is targeting as well as monitor temperature at the focal zone. The methods of monitoring temperature with MRI were described in Chapter 2. Unless otherwise noted, the material found is this chapter is taken from (1).

3.2 Ultrasound Physics

Ultrasound has a frequency above the range of human hearing, meaning above 20 kHz, and for typical HIFU applications will have frequencies ranging from a few hundred kHz to several MHz. The ultrasound wave is produced using a piezoelectric material. When a voltage is applied to a piezoelectric material, the shape will deform. By applying an alternating voltage at the correct frequency, a sound wave of the same frequency is produced. These piezoelectric devices are called ultrasound transducers because they convert electric energy into mechanical energy (ultrasound). The energy transduction also works in reverse. Any deformation of the piezoelectric by in incoming pressure wave will generate a voltage. This is the underlying basis for ultrasound detection and imaging with ultrasound.

As ultrasound travels from the transducer, it will be affected by the material it passes through. The physical properties affecting the ultrasound propagation include the acoustic impedance, Z, absorption coefficient, μ, and the speed of sound, c. The mechanical vibrations along the beam propagation path will create a pressure, p, and results in a particle velocity, u. The particles have no net motion, they move in an oscillatory motion about their central position. The speed of sound will vary between tissue types and is related to the acoustic impedance by the following equation

$$Z = \frac{p}{u} = \rho c \qquad [3.1]$$

where ρ is the density of the tissue. For most soft tissues, the speed of sound is close to that of water, $c_w = 1500\ m/s$. The wavelength, λ, of the ultrasound beam through a medium is given by

$$\lambda = \frac{c}{f} \qquad [3.2]$$

where *f* is the frequency of the wave. An ultrasound beam traveling in water with a frequency of 1 MHz would have a wavelength of $\lambda = 0.15$ cm. The power density of a wave is defined as

$$I = \frac{p^2}{Z}. \qquad [3.3]$$

As the ultrasound beam propagates through a material, the intensity will dissipate due to several factors, which include absorption, scattering and reflections from interfaces. The absorption and scattering contributions are generally combined into a single attenuation coefficient α, (not to be confused with the PRF coefficient, which also uses α), which will vary with tissue type and will increase with frequency. When a wave enters a tissue with an initial pressure p_0 and the associated power density I_0, it will have an attenuated pressure and power density after traveling a distance z through the tissue as shown in Equation [3.4]

$$p(z) = p_0 e^{-\alpha z} \qquad I(z) = I_0 e^{-2\alpha z} \qquad [3.4]$$

At every interface between materials with different acoustic impedances, some percentage of the ultrasound will be transmitted and reflected depending on the difference in impedance as shown in Figure 3.1. The transmitted wave will be refracted at the angle that is given by Snell's law, which applies for ultrasound waves just as it does for electromagnetic waves

$$\frac{\sin\theta_i}{c_1} = \frac{\sin\theta_t}{c_2} \qquad [3.5]$$

where θ_i and θ_t are the angles of the incident and transmitted waves, and c_1 and c_2 are the respective speeds of sound. The reflection coefficient, R, defined as the ratio of

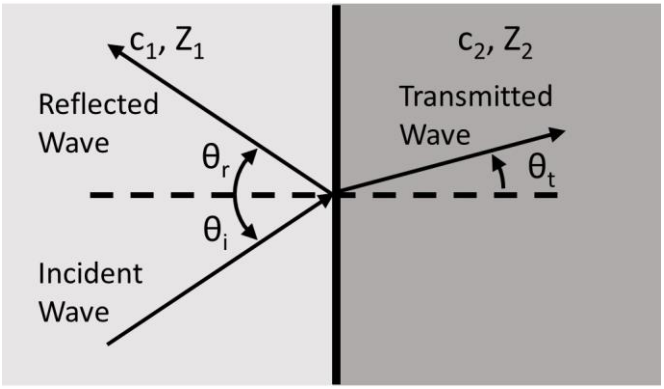

Figure 3.1. Reflection and refraction of incident wave at interface between two mediums, in this case, $c_1 > c_2$.

the reflected and transmitted pressure waves at an interface, is given by the following equation (1)

$$R = \frac{p_r}{p_i} = \frac{\left(\frac{Z_2}{\cos\theta_t}\right) - \left(\frac{Z_1}{\cos\theta_i}\right)}{\left(\frac{Z_2}{\cos\theta_t}\right) + \left(\frac{Z_1}{\cos\theta_i}\right)} \quad [3.6]$$

where Z_1 and Z_2 are the acoustic impedances of the two materials. For an incident wave with normal incident, or a wave with small incidence angle ($\theta_i \approx 0°$), the reflection coefficient will be exactly equal or approximately equal to

$$R = \frac{Z_2 - Z_1}{Z_2 + Z_1} \quad [3.7]$$

The reflection coefficient is related to the reflected power through Equation [3.3].

$$\frac{I_r}{I_i} = \frac{p_r^2/Z_1}{p_i^2/Z_1} = R^2 \quad [3.8]$$

For the transmitted wave the fraction of transmitted power is

$$\frac{I_t}{I_i} = \frac{(1 + p_r/p_i)^2 Z_1}{Z_2} = (1+R)^2 \frac{Z_1}{Z_2} \quad [3.9]$$

Any interface with a large impedance mismatch, such as tissue and air, will cause the vast majority of ultrasound to be reflected. This must be taken into account when

positioning the transducer to treat the patient. Any tissue/air interfaces in the far field can cause skin burns when the ultrasound is reflected.

In order to create an intense heating at the tissue to apply a thermal treatment, the ultrasound wave must be concentrated into a focus. It is possible to shape the face of the transducer into a spherical shape which will have a natural geometric focus determined by the radius of curvature. This can either be done with a single transducer face, or to break up the surface of the sphere into many individually controlled transducer elements. This is called a phased-array transducer. A phased-array transducer has several advantages over a single element of the same size. The amplitude and phase of each element can be controlled individually and certain elements can be turned off if necessary, (e.g., if the incidence angle with the skull is too large) without sacrificing the ability to treat the patient. It is possible to move the focus of a phased-array transducer by adjusting the phase of each element. This provides a significant advantage, as the physical location of the transducer does not need to be adjusted in order to treat a larger volume. Any motion within the MRI can cause significant artifacts in the temperature measurements, as was described in Chapter 2. The ability to move the focus without physically moving the transducer also improves the monitoring ability and adds the capability to use complex heating trajectories. A phased-array does add complexity (and therefore cost) to the ultrasound system. Power is also lost to secondary grating lobes, which is power deposited outside the focus. The grating lobes can be decreased by placing the individual elements of the transducer no further apart than half the ultrasound wavelength or to randomly place the elements on the transducer face. Random placement will limit the number of

locations with constructive interference.

The focal spot of a transducer is ellipsoidal in shape. The exact size and shape of the focus depends on the size, shape and frequency of the transducer. For a spherical transducer, the pressure pattern at the focal plane is related to the first-order Bessel function of the first kind with a focal spot diameter, d, given by (1)

$$d = 2.44\left(\frac{l_f}{D}\right)\lambda \qquad [3.10]$$

where l_f is the focal length, D is the diameter of the transducer and λ is the wavelength of the ultrasound as shown in Figure 3.2. A lower frequency will have a larger wavelength and thus a larger focal diameter.

3.3 Difficulties in FUS

The ability of FUS to deliver energy was first demonstrated in the 1940s (12). The main obstacle to widespread adoption of the technology was the lack of ability to

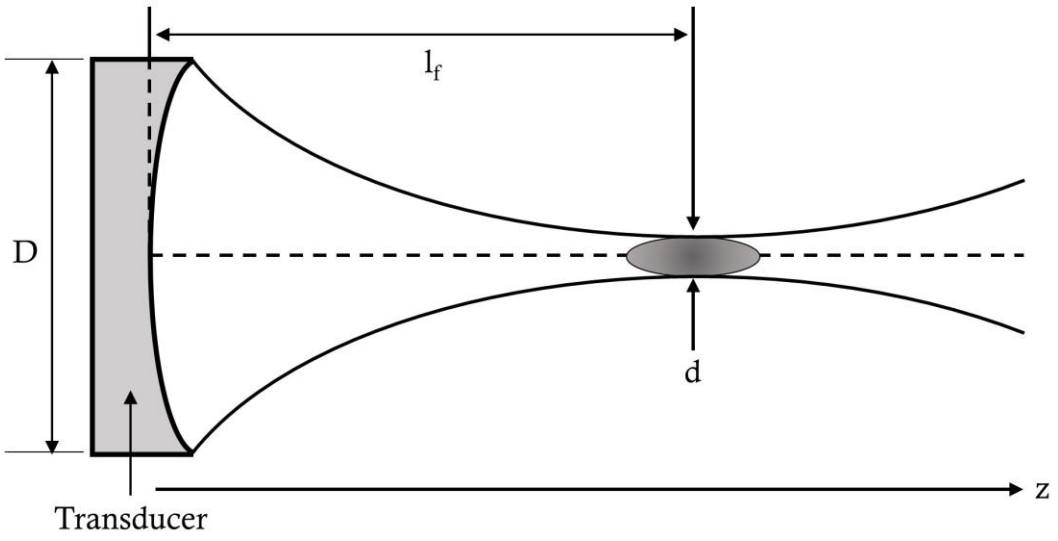

Figure 3.2. Schematic diagram of ultrasound transducer with diameter D, focal length l_f, and focus diameter d.

monitor in real-time the energy deposition. The rise of MR thermometry and rapid imaging techniques has filled this need. Treatment of a large volume requires multiple sonications with time allowed for cooling between sonications. The focal region will experience the largest temperature rise, while some energy is still deposited in the near and far fields. If insufficient time is allowed for cooling, the energy deposition in the near field can cause significant temperature rises, especially if there is fatty tissue in the near field. Fatty tissue will hold on to the increase in temperature for a longer time than aqueous tissue for several reasons. While fatty tissue has a lower specific heat capacity than muscle, it also has a lower thermal conductivity (13), meaning it takes longer to disperse the heat energy. Fatty tissue will also typically have less blood flow to carry away extra heat. An inhomogeneous mixture of tissue in the ultrasound near field will distort the beam path, causing the focus to blur and shift from the intended location (14). While it is possible to correct the beam aberration (14), it requires accurate 3D models and segmentation of the tissue.

Bone has a large difference in impedance and speed of sound when compared to tissue and a higher absorption coefficient, meaning that much of the ultrasound will be reflected at both sides of the bone interface as well as absorbed by the bone (15). In order to treat the brain, a large ultrasound transducer with many (around 1000) individual elements is used to spread the energy paths over as much of the skull as possible. Beam aberration correction can significantly improve the efficacy of energy delivered to the focus through the skull (16). It is also difficult to measure temperature in bone due to its low water content and short T_2^* (17,18). Another simple difficulty can be to simply determine where the focus is located. When the transducer has

multiple degrees of freedom, it can be difficult to locate the geometric focus in MR coordinates. This particular difficulty is discussed at length in Chapter 6.

3.4 References

1. Christensen DA. Ultrasonic bioinstrumentation. New York: Wiley; 1988. xiii, 235 p.

2. Diederich CJ, Stafford RJ, Nau WH, Burdette EC, Price RE, Hazle JD. Transurethral ultrasound applicators with directional heating patterns for prostate thermal therapy: in vivo evaluation using magnetic resonance thermometry. Med Phys 2004;31(2):405-413.

3. Gianfelice D, Khiat A, Amara M, Belblidia A, Boulanger Y. MR imaging-guided focused ultrasound surgery of breast cancer: correlation of dynamic contrast-enhanced MRI with histopathologic findings. Breast Cancer Res Treat 2003;82(2):93-101.

4. Gianfelice D, Khiat A, Amara M, Belblidia A, Boulanger Y. MR imaging-guided focused US ablation of breast cancer: histopathologic assessment of effectiveness-- initial experience. Radiology 2003;227(3):849-855.

5. Huber PE, Jenne JW, Rastert R, Simiantonakis I, Sinn HP, Strittmatter HJ, von Fournier D, Wannenmacher MF, Debus J. A new noninvasive approach in breast cancer therapy using magnetic resonance imaging-guided focused ultrasound surgery. Cancer Res 2001;61(23):8441-8447.

6. Hynynen K, McDannold N, Vykhodtseva N, Jolesz FA. Noninvasive MR imaging-guided focal opening of the blood-brain barrier in rabbits. Radiology 2001;220(3):640-646.

7. Hynynen K, Vykhodtseva NI, Chung AH, Sorrentino V, Colucci V, Jolesz FA. Thermal effects of focused ultrasound on the brain: determination with MR imaging. Radiology 1997;204(1):247-253.

8. Illing RO, Kennedy JE, Wu F, ter Haar GR, Protheroe AS, Friend PJ, Gleeson FV, Cranston DW, Phillips RR, Middleton MR. The safety and feasibility of extracorporeal high-intensity focused ultrasound (HIFU) for the treatment of liver and kidney tumours in a Western population. Br J Cancer 2005;93(8):890-895.

9. Sanghvi NT, Foster RS, Bihrle R, Casey R, Uchida T, Phillips MH, Syrus J, Zaitsev AV, Marich KW, Fry FJ. Noninvasive surgery of prostate tissue by high intensity focused ultrasound: an updated report. Eur J Ultrasound

1999;9(1):19-29.

10. Wu F, Wang ZB, Zhu H, Chen WZ, Zou JZ, Bai J, Li KQ, Jin CB, Xie FL, Su HB. Feasibility of US-guided high-intensity focused ultrasound treatment in patients with advanced pancreatic cancer: initial experience. Radiology 2005;236(3):1034-1040.

11. Weintraub D, Elias WJ. The emerging role of transcranial magnetic resonance imaging-guided focused ultrasound in functional neurosurgery. Mov Disord 2016.

12. Lynn JG, Zwemer RL, Chick AJ, Miller AE. A new method for the generation and use of focused ultrasound in experimental biology. J Gen Physiol 1942;26(2):179-193.

13. Giering K, Lamprecht I, Minet O. Specific heat capacities of human and animal tissues. 1996. p 188-197.

14. Hinkelman LM, Liu DL, Waag RC, Zhu Q, Steinberg BD. Measurement and correction of ultrasonic pulse distortion produced by the human breast. J Acoust Soc Am 1995;97(3):1958-1969.

15. Pinton G, Aubry JF, Bossy E, Muller M, Pernot M, Tanter M. Attenuation, scattering, and absorption of ultrasound in the skull bone. Med Phys 2012;39(1):299-307.

16. Vyas U, Kaye E, Pauly KB. Transcranial phase aberration correction using beam simulations and MR-ARFI. Med Phys 2014;41(3):032901.

17. Techawiboonwong A, Song HK, Leonard MB, Wehrli FW. Cortical bone water: in vivo quantification with ultrashort echo-time MR imaging. Radiology 2008;248(3):824-833.

18. Tyler DJ, Robson MD, Henkelman RM, Young IR, Bydder GM. Magnetic resonance imaging with ultrashort TE (UTE) PULSE sequences: technical considerations. J Magn Reson Imaging 2007;25(2):279-289.

CHAPTER 4

THE EFFECT OF 2D EXCITATION PROFILE ON T_1 MEASUREMENT ACCURACY USING THE VARIABLE FLIP ANGLE METHOD

This chapter is based on a conference poster titled, "The Effect of 2D Excitation Profile on T_1 Measurement Accuracy Using the Variable Flip Angle Method" authored by Bryant T. Svedin and Dennis L. Parker. This poster was presented at the International Society for Magnetic Resonance in Medicine in Milan, Italy; May, 2014.

4.1 Introduction

The longitudinal relaxation time (T_1) is an intrinsic property of tissues and changes with water content, temperature, relaxation agents, local molecular environment, and main magnetic field strength (1,2). The dependence of T_1 on different physical properties make T_1 mapping useful for several fields of interest including dynamic contrast-enhanced studies of tissue perfusion (3,4), diagnosis of neurological diseases (5), MRI thermometry (6), and digestive transport (7).

There are several methods for T_1 measurement, most of which are relatively slow, e.g., (8-10). The method examined in this work is the Variable Flip Angle (VFA) method, which is based on the steady state relationship of the measured signal to repetition time (TR), T_1, and flip angle (11). The basic implementation of this method is to acquire signal from two scans with the exact same parameters, except flip angle,

and then use the spoiled gradient recalled (SPGR) steady state signal equation to calculate T_1 as explained below in the Theory section. The first implementation of the VFA method was performed using a 2D acquisition (11). Most VFA T_1 measurement studies have been performed using 3D acquisitions, e.g., (12-16), but to decrease acquisition time the VFA method could be performed in 2D. A major source of error when using VFA method are variations in transmit radiofrequency (RF) field (B1+), which occur from tissue dielectric effects (17). It is assumed that the actual flip angle is linearly dependent on the strength of the transmit RF field, and therefore a linear correction can be used.

In addition to variations in the transmit RF field, another major source of error in 2D acquisitions is the nonuniform slice excitation profile which causes a large variation in flip angle within every single voxel. For flip angles larger than the Ernst angle, this creates a steady state slice profile with significant signal contribution from the edges of the slice, which experienced less than the desired flip angle. The variation in RF excitation profile is less of a problem in 3D acquisitions, because as long as the slice is near the center of the slab, so as to have received the desired flip angle, the signal will follow the theoretical SPGR relationship. The nonuniform slice excitation profile problem was examined by Parker et al. (18) as they studied measuring T_1 in 2D acquisitions using a dual acquisition method similar to VFA where TR was varied instead of flip angle. They created a lookup table to map the transmit RF field, and a lookup table to calculate T_1 based on a ratio of the signal magnitudes from the two different TR scans. Their method required one of the TR values to be much longer than the other, increasing total scan time, as well as creating a lookup table for RF

field and a lookup table for the signal ratios using the two TR values. If different TR values are used, a new lookup table would be required.

In an attempt to deal with the nonuniform excitation profile across the slice in the VFA method, it can be assumed that the signal depends on an average flip angle, and therefore is corrected at the same time as the transmit RF error using the same technique. The assumption of an average flip angle may work well for small angles, but the accuracy will decrease as the angle increases and will be poor for angles that exceed the Ernst angle due to the extra signal contribution from edges of the slice. When the nominal flip angle is larger than the Ernst angle, there are spins near both edges of the slice profile which will experience the Ernst angle and contribute significant signal. The amount of extra signal depends on the shape of the slice profile, which depends on the RF pulse properties. In 3D acquisitions, the optimal flip angles are those that give approximately 71% of the maximum signal at the Ernst angle (16). This is not the case in 2D, because the nonuniform excitation profile creates a signal vs. flip angle relationship which does not follow the theoretical SPGR signal dependence.

The purpose of this study was to evaluate the dependence of the signal equation on the excitation profile and determine the resulting accuracy and precision in T_1 measurements in 2D acquisitions. The slice excitation profile was simulated using numerical solutions of the Bloch equations to develop a model of the signal dependence to the RF excitation pulse properties. This model was tested with simulations and experiments.

4.2 Theory

The VFA method for measuring T_1 makes use of the spoiled gradient recalled (SPGR) steady state signal equation

$$S = M_0 \frac{(1 - E_1)\sin(\alpha)}{1 - E_1\cos(\alpha)} E_2 \qquad [4.1]$$

where E_1 = exp(-TR/T_1) and E_2 = exp(-TE/T_2^*). Here, M_0 is the equilibrium magnetization, α is the flip angle, TR is the pulse repetition time, TE is the sequence echo time, T_1 and T_2^* are the longitudinal and transverse relaxation times. This equation is derived assuming that TR >> T_2^*, or adequate spoiling is used to ensure that negligible transverse signal remains before subsequent excitations. If these conditions are not met, Equation [4.1] will not accurately describe the signal, and significant errors in T_1 calculation will occur. Equation [4.1] rewritten in linear form is (11)

$$\frac{S}{\sin(\alpha)} = E_1 \frac{S}{\tan(\alpha)} + M_0(1 - E_1)E_2\,. \qquad [4.2]$$

Calculation of T_1 is done by acquiring the signal at two different flip angles and fitting a line to $S/\sin(\alpha)$ versus $S/\tan(\alpha)$ to determine the slope m. This slope is equal to E_1 and thus T_1 is calculated using

$$T_1 = \frac{-\mathrm{TR}}{\ln(m)} \qquad [4.3]$$

4.3 Methods

4.3.1 Simulations

Simulations were performed to analyze the effects of the slice excitation profile on the accuracy of T_1 measurements using the VFA method. The initial excited

magnetization profile was calculated using a numerical implementation of the Bloch equations to simulate the effects of the excitation pulse and slice select gradient. The shape of the magnetization profile after excitation is dependent on several factors including the desired flip angle α, the TR/T_1 ratio, and the time-bandwidth product (TBP) of the excitation pulse. (TBP is defined as the product of the pulse bandwidth and pulse duration.) Therefore, simulations were performed for flip angles 1° through 90° in 1° increments, for TBP 2, 4, 6, 8, 10, and T_1 = 280, 740 ms (values chosen to match the experiment described below). All simulations use a TR of 20 ms, slice thickness of 3 mm, and RF pulse duration of 4 ms. To maintain RF pulse duration and slice thickness as constant, the desired TBP was achieved by changing the bandwidth and amplitude of the RF pulse as well as the amplitude of the slice selection gradient, which is what is typically done in practice.

To simulate the excitation profile, the free precession and rotation caused by the Hamming windowed sinc excitation pulse and slice select gradient were simulated as they are played out in time, for each position in the slice. The magnetization's dependence on T_1 and T_2 are assumed to be negligible during the time the of RF pulse. Because the nominal (desired) flip angle is only achieved near the center of the slice, the actual flip angle achieved for each slice position is found by

$$\alpha(z) = tan^{-1}\frac{\sqrt{M_x(z)^2 + M_y(z)^2}}{M_z(z)} \qquad [4.4]$$

where $M_x(z), M_y(z), M_z(z)$ are the x, y, and z components of the magnetization vector.

Simulation of the steady state signal for each magnetization profile was done

using the same method as (18). The total signal measured is the integral of Equation [4.1] over the whole slice thickness, but because there is significant signal contribution from both the $M_x(z)$ and $M_y(z)$, Equation [4.1] must be modified to include the phase of the transverse magnetization $\Phi(z)$,

$$M_x = A\int_{slice}\left\{\frac{(1-E_1)\sin(\alpha(z))\cos(\Phi(z))}{1-E_1\cos(\alpha(z))}\right\}dz \qquad [4.5]$$

$$M_y = A\int_{slice}\left\{\frac{(1-E_1)\sin(\alpha(z))\sin(\Phi(z))}{1-E_1\cos(\alpha(z))}\right\}dz \qquad [4.6]$$

where A is a constant of proportionality. This integral can be discretized over the slice profile, and because signal is directly proportional to transverse magnetization we get

$$S_x = A\sum_{n=1}^{N}\left\{\frac{(1-E_1)\sin(\alpha(n))\cos(\Phi(n))}{1-E_1\cos(\alpha(n))}\right\}\Delta z \qquad [4.7]$$

$$S_y = A\sum_{n=1}^{N}\left\{\frac{(1-E_1)\sin(\alpha(n))\sin(\Phi(n))}{1-E_1\cos(\alpha(n))}\right\}\Delta z \qquad [4.8]$$

where S_x and S_y are the real and imaginary components of the signal, N is the number of equally spaced discrete samples indexed by n, and Δz is the spacing between samples. For this study, we used N = 1201 over a slice profile from $z = -6\ mm$ to $z = +6\ mm$. The total signal is

$$S = \sqrt{{S_x}^2 + {S_y}^2}. \qquad [4.9]$$

The integrated signal for the imaginary components, Equations [4.6] and [4.8], is equal to zero for the pulse used, because the imaginary component is antisymmetric as seen in Figure 4.1. This is not always the case, as it depends on the axis of rotation and the properties of the RF pulse.

T_1 values were calculated for simulation and experimental data using the VFA

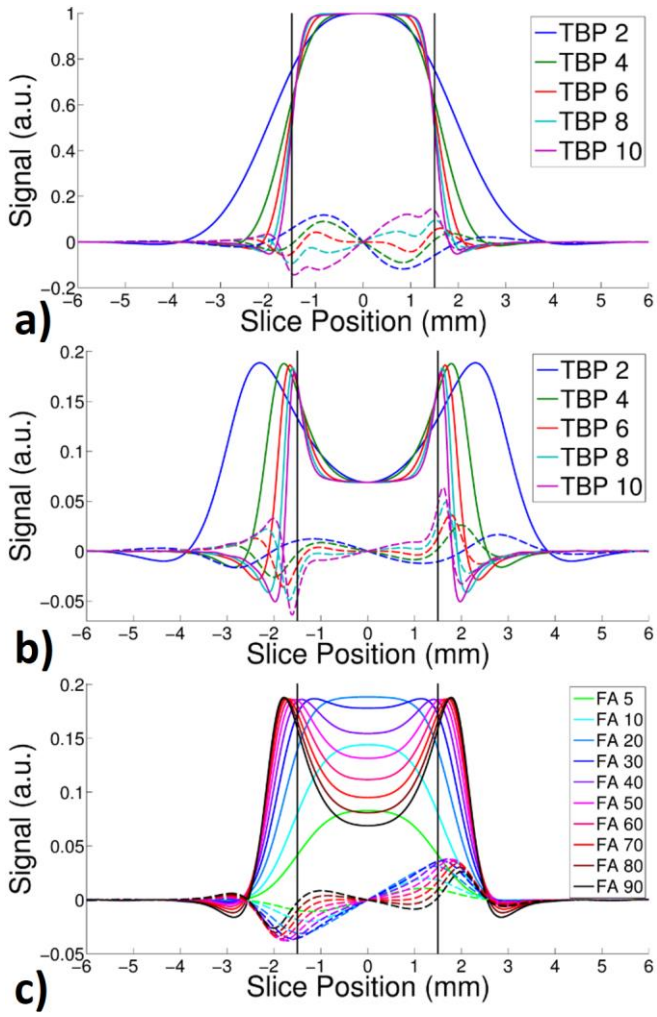

Figure 4.1 – Excitation profile simulation results. Real component (solid) and imaginary (dashed). Black vertical bars show desired slice thickness of 3 mm. Comparison of TBP 2, 4, 6, 8, 10, at 90° flip angle, TR = 20 ms, T_1 = 280 ms for a) initial excitation profile b) and steady state profiles. c) Comparison of steady state profile for TBP 4 at various flip angles.

method for every combination of flip angles and compared to the true values. A flip angle correction technique was used to calculate a correction value c, as described below, and T_1 values were calculated again using the VFA method but with corrected flip angle $c \cdot \alpha$ and compared to true values.

To simulate the sensitivity of T_1 measurements to errors, noisy measurements were simulated using a Monte Carlo technique. Complex white Gaussian noise of

constant power was added to the complex signal profile before integration. 3000 noisy signals were generated, and T_1 estimates were calculated for every combination of flip angle, using the flip angle correction technique described below, for each noisy signal. The standard deviation (σ_{T1}) at each flip angle combination was calculated from the 3000 estimates. The noise power is the same for all realizations, but the lower TBP will have a higher signal to noise ratio (SNR) than higher TBPs in 2D, because the imperfect excitation profile produces a thicker slice leading to more signal contribution. Therefore, to normalize the results to SNR, the fractional error (σ_{T1}/T_1) is multiplied by the maximum SNR (at the Ernst Angle). This same technique was also applied to the ideal SPGR signal for comparison.

4.3.2 Experiment

An experiment was performed to acquire signal vs. flip angle data for TBP 2, 4, 6, 8, 10 in 2D using a homogeneous gelatin phantom and excised human breast fat at flip angles in 5° degree increments from 5° to 90°. A GRE sequence capable of changing TBP while maintaining constant pulse duration was used (scan parameters: 2x2x3 mm resolution; TR/TE = 20/5 ms; FOV 128x128 mm; 4 averages). Signal values were averaged over a 3x3 ROI near the center of both the gelatin and breast fat. Multiple inversion time inversion recovery (IR) data (1x1x3 mm resolution; TR/TI = 6000/25, 100, 300, 500, 700, 1200, 3000, 5500 ms; FOV 128x128 mm) was collected to accurately calculate T_1 using the inversion recovery (IR) method to compare with values calculated using VFA method, and for use in the flip angle correction.

4.3.3 Flip Angle Correction Method

A 2D flip angle correction method was implemented to correct for both B1+ inhomogeneity and average flip angle across the slice profile. This is the same method employed by (19). For experimental data, a reference T_1 map was obtained using the IR method. The signal vs. flip angle data for both simulation and experiment (voxel-by-voxel) were fit to Equation [4.1] using a least-squares fit with the known/measured T_1 values and user defined TR value with free parameters M0 and c, where c is defined by $\alpha_a = c \cdot \alpha_d$, where α_a is the estimate of the actual/average flip angle, α_d is the desired flip angle and c is the flip angle correction value. An accurate estimate of T_1 is required for this fit. Because this method assumes a linear relation between the desired and actual flip angles, it works well for B1+ inhomogeneity, but is only an approximation for the nonlinear relationship due to the excitation profile within a voxel across the slice.

4.4 Results

The real and imaginary excitation profile simulation results are shown in Figure 4.1. For flip angles larger than the Ernst angle, the imperfect slice profile leads to significant signal contribution from the outer regions of the slice which experienced flip angles less than the desired flip angle. This anomalous increased signal for large flip angles leads to errors in calculations of T_1. A larger TBP gives a more rectangular excitation profile leading to less erroneous signal and better T_1 estimates as discussed in the next section. A larger TBP requires a larger amplitude RF pulse and a larger slice select gradient to achieve the same desired slice thickness using the same pulse duration. As SAR increases with the square of the pulse amplitude, a tradeoff between

desired slice profile and SAR needs to always be considered.

In comparing the simulation and experiment, both the breast fat and gelatin phantom experienced B1+ inhomogeneity across the slice as can be seen in Figure 4.2 (a-b) where the signal from the simulation and experiments do not agree. This effect of the B1+ inhomogeneity was corrected to a large measure using the flip angle correction technique and the improved comparison signal curves are shown in Figure 4.2 (c-d).

Figure 4.3 (a-b) shows the signal normalized to maximum value vs. flip angle for simulations with TBP 2, 4, 6, 8, and 10 as well as the expected SPGR steady state signal, Equation [4.1]. Equation [4.1] does not accurately describe the total signal as a function of flip angle in 2D acquisitions. Using the assumption of the total signal being dependent on the average flip angle in the slice and the flip angle correction technique, the total signal vs. corrected flip angle is shown in Figure 4.3 (c-d). The 2D signal vs. flip angle profiles are much closer to the steady state equation when the flip angle correction is used.

Figure 4.4 shows the T_1 estimates calculated without flip angle correction. For low TBP (TBP = 2 in parts a and d) these calculations underestimate T_1 for all flip angle combinations. The amount of underestimation increases with flip angle. As TBP increases (TBP = 6 in parts b and e) the underestimation of T_1 is reduced. At higher TBP (TBP = 10 in parts c and f) the underestimation of T_1 is further reduced for lower flip angles, and shows a band of overestimation using larger flip angles. While some combinations in this band produce accurate T_1 estimates, it should be noted that no noise has been added to the simulations at this point. Once noise is added,

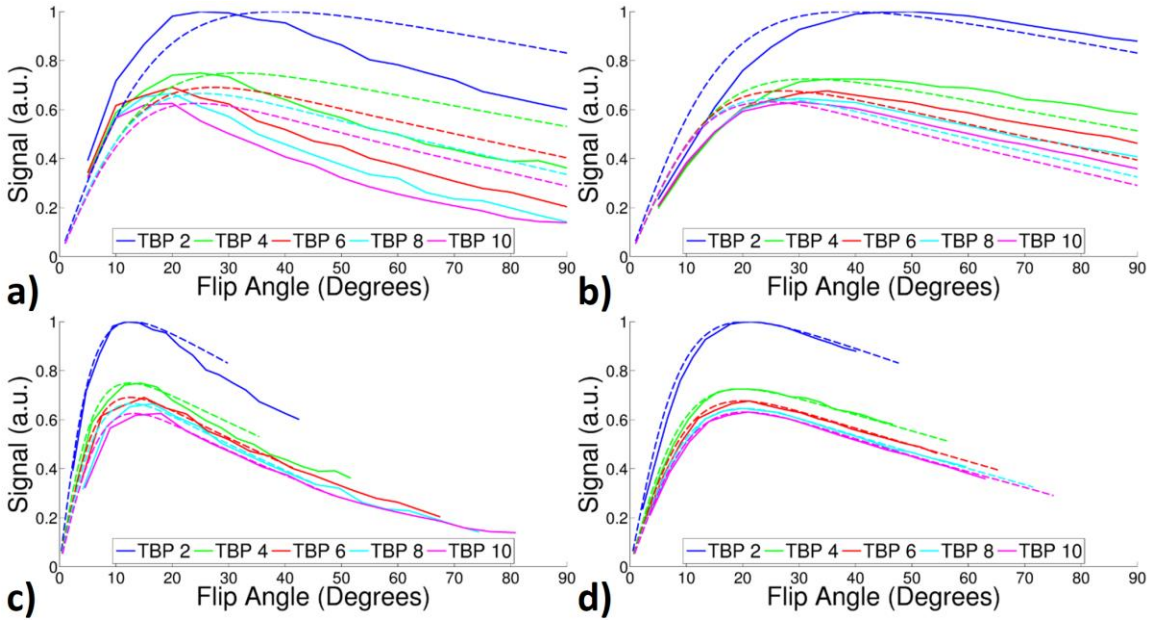

Figure 4.2 - Comparison of total signal vs. flip angle from Bloch simulations (dash) to experiment (solid) for TBP 2, 4, 6, 8, and 10 using (a) gelatin phantom (T_1 = 741±3 ms) and (b) breast fat (T_1 = 278±8 ms). Signal vs. flip angle using calculated flip angle correction values for (c) gelatin phantom and (d) breast fat.

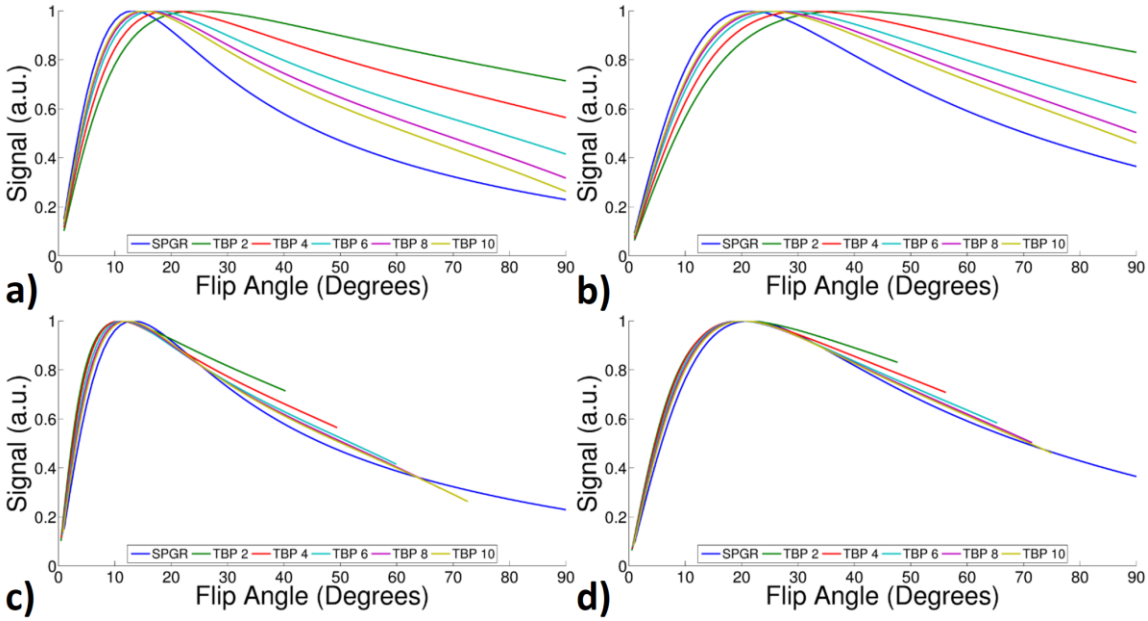

Figure 4.3 – Normalized total signal vs. flip angle from Bloch simulations for TBP 2, 4, 6, 8, 10 compared to normalized SPGR signal Eq. [4.1] at a) T_1 = 740 ms and b) T_1 = 280 ms. Signal vs. flip angle using calculated flip angle correction values for c) T_1 = 740 ms and d) T_1 = 280 ms.

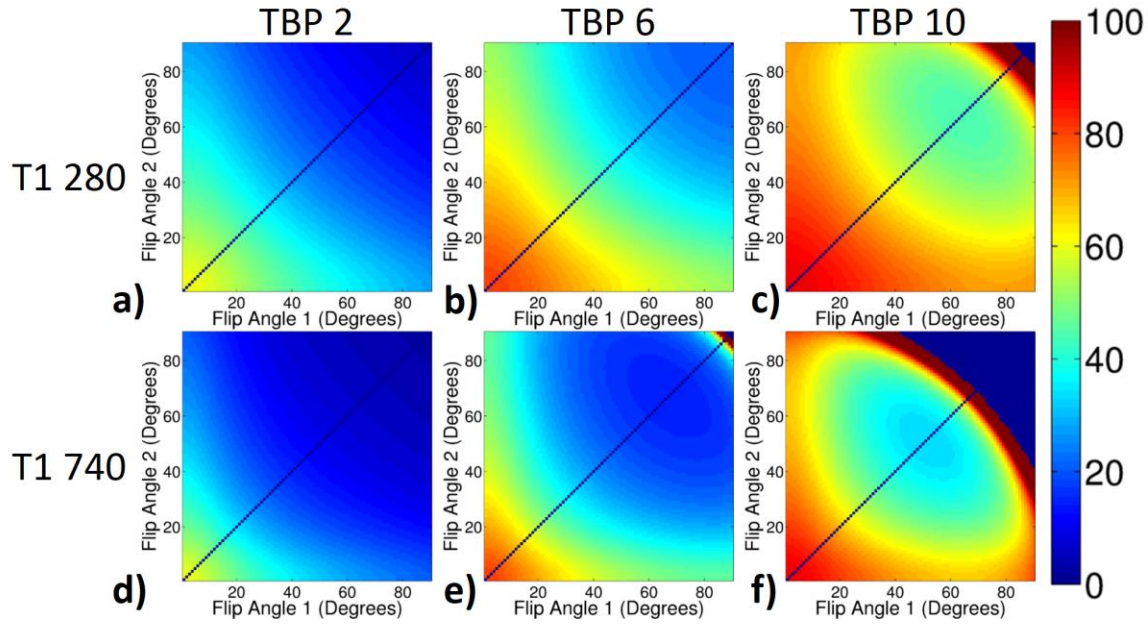

Figure 4.4 – Bloch simulation calculations of $T_1$for every combination of flip angles displayed as percent of true T_1. a-c) T_1 = 280 ms a) TBP 2, b) TBP 6, c) TBP 10. d-f) T_1 = 740 ms d) TBP 2, e) TBP 6, f) TBP 10.

measurements of T_1 at these combinations is unreliable. The large flip angle combination region of the higher TBP figures shows a calculated T_1 that is negative, which is because the calculated slope between $S/\sin(\alpha)$ and $S/\tan(\alpha)$ for these large flip angles is greater than 1. For arguments greater than 1, the log function is positive leading to a negative T_1 from Equation [4.3].

Figure 4.5 shows the T_1 estimates calculated with flip angle correction. Accurate measurements of T_1 can be obtained from multiple combinations. These results depend heavily on the TR/T_1 ratio and TBP. A decrease in T_1 or an increase in TR, will increase the number of combinations leading to accurate T_1 estimates; also, as TBP increases, the range of combinations resulting in an accurate T_1 also increases. This increase in flip angle combination choices also adds a little more "forgiveness" to slightly incorrect choice in angles.

The bands giving reasonable T_1 values are demonstrated in Figure 4.6 where only flip angle combinations resulting in a T_1 estimate that is between 95% and 105 % of the true value are shown. The region of accuracy increases with TBP. An added benefit of increasing the TBP is the ability to measure T_1 values of different tissue types within 5% accuracy by using the same flip angle choices in 2D. Low TBP has no or small overlap of accuracy regions depending on the T_1 values of the tissues of interest. For example, using desired (uncorrected) flip angles 10° and 60° and TBP 2, simulated T_1 estimates are 130% and 129% of true T_1 of 280 ms and 740 ms, respectively, but with TBP 10, T_1 estimates are 104% and 96% of true T_1 of 280 ms and 740 ms, respectively. The signal dependence on the TR/T_1 ratio means increasing TR will make this overlap region even larger.

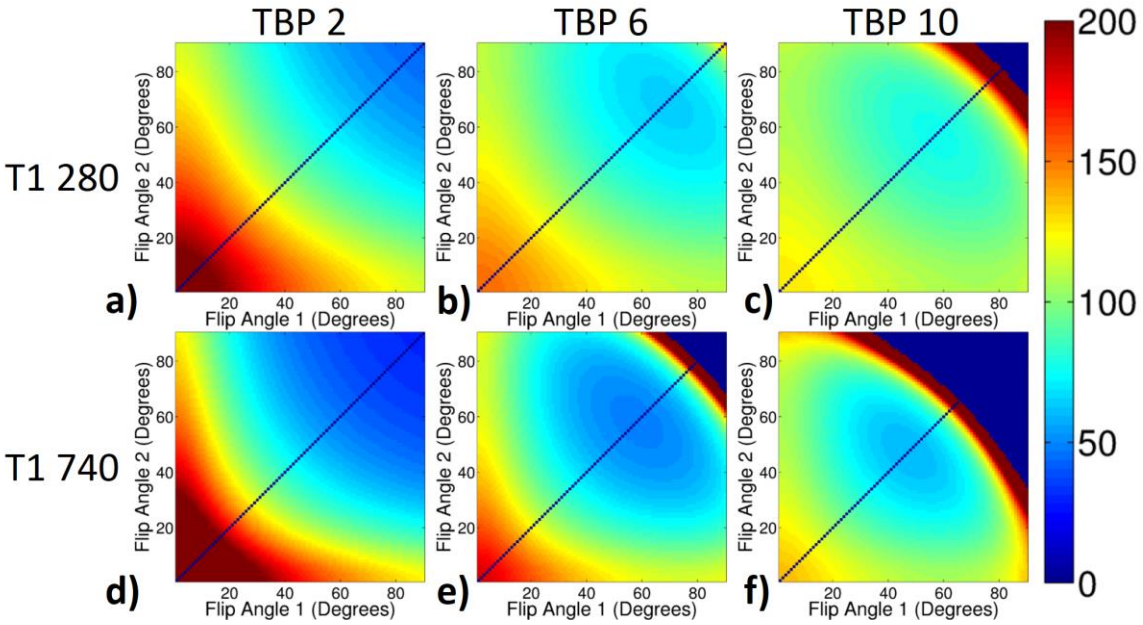

Figure 4.5 – Bloch simulation calculations of T_1 for every combination of flip angles using flip angle correction displayed as percent of true T_1. a-c) T_1 = 280 ms a) TBP 2, b) TBP 6, c) TBP 10. d-f) T_1 = 740 ms d) TBP 2, e) TBP 6, f) TBP 10. Flip angles shown are desired flip angle.

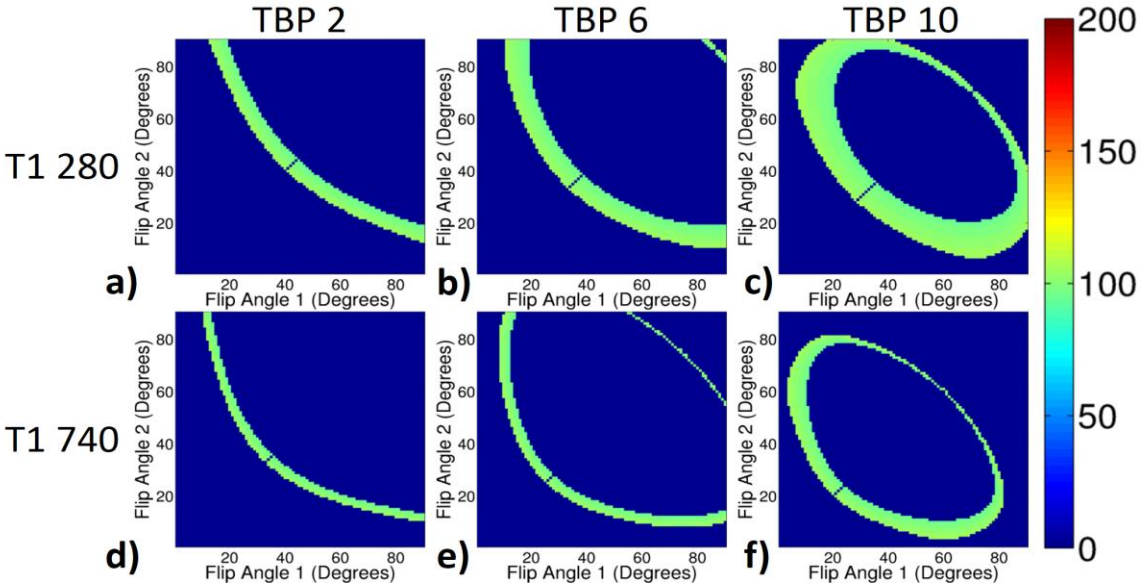

Figure 4.6 – Bloch simulation calculations of T_1 for every combination of flip angles using flip angle correction within 5% of true T_1. a-c) T_1 = 280 ms a) TBP 2, b) TBP 6, c) TBP 10. d-f) T_1 = 740 ms d) TBP 2, e) TBP 6, f) TBP 10. Flip angles shown are desired flip angle.

Experimental results using flip angle correction are shown in Figure 4.7. Calculation of T_1 using IR method gives values of 278 ± 8 ms and 741 ± 3 ms for the breast fat and gelatin respectively. Results for excised breast fat agree well with simulation. The gelatin phantom data was noisier and agrees with simulation for a smaller range of flip angle combinations in the lower flip angle region. Using the same desired flip angles as above, 10° and 60° and TBP 2, T_1 estimates are 111% and 115% of true T_1, but with TBP 10, T_1 estimates are 104% and 106% of true T_1 for breast fat and gelatin, respectively.

Results of the Monte Carlo simulation are shown in Figure 4.8. The ratio of standard deviation to true T_1 (σ_{T1}/T_1) is directly inversely proportional to the SNR. Therefore, results are displayed as maximum SNR times the fractional error in T_1 to demonstrate measurement precision bias for any SNR. Flip angle combinations near the line of identity have very high standard deviation. Higher TBP have a band of very high standard deviation across the larger flip angles making them unreliable for T_1 estimates, which is also seen in the SPGR figures. Monte Carlo simulations were also done for the SPGR steady state signal equation, Equation [4.1]. The results show a minimum standard deviation for flip angle combinations that are approximately 71% of the maximum. This agrees with the conclusion made by (16).

4.5 Discussion

This paper has considered the problem of using the variable flip angle method in conjunction with a 2D acquisition to make quantitative measurements of the longitudinal relaxation time, T_1. The nonrectangular excitation profile leads to signal contribution from the outer edges of the slice, which experience a flip angle less than

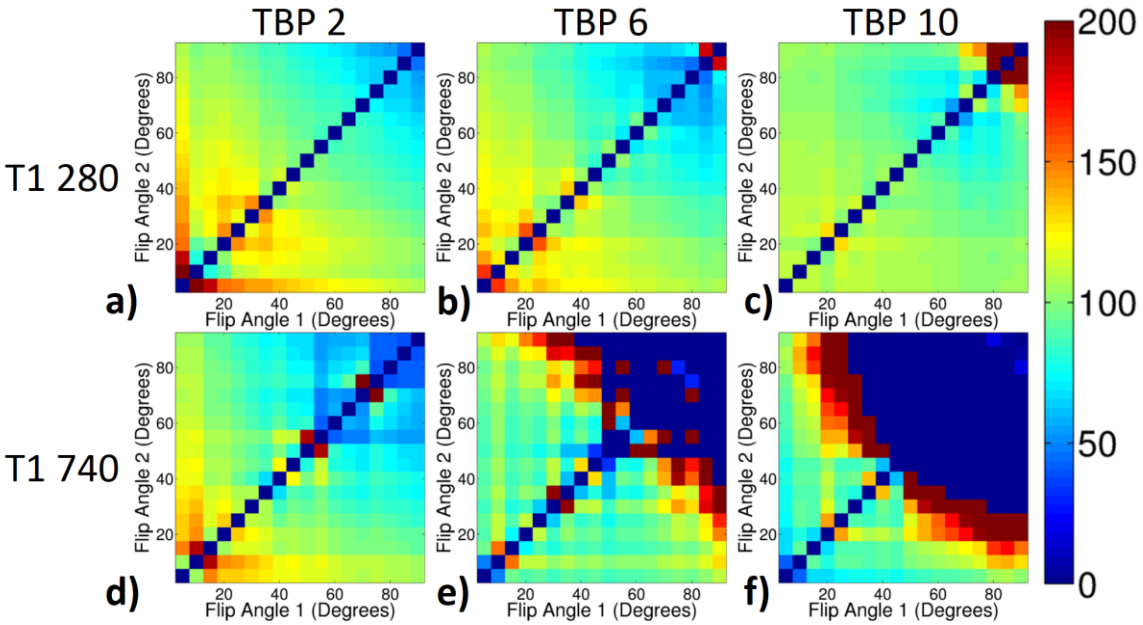

Figure 4.7 – Experimental calculations of T_1 for every combination of flip angles using flip angle correction displayed as percent of true T_1. a-c) T_1 = 280 ms a) TBP 2, b) TBP 6, c) TBP 10. d-f) T_1 = 740 ms d) TBP 2, e) TBP 6, f) TBP 10. Flip angles shown are desired flip angle.

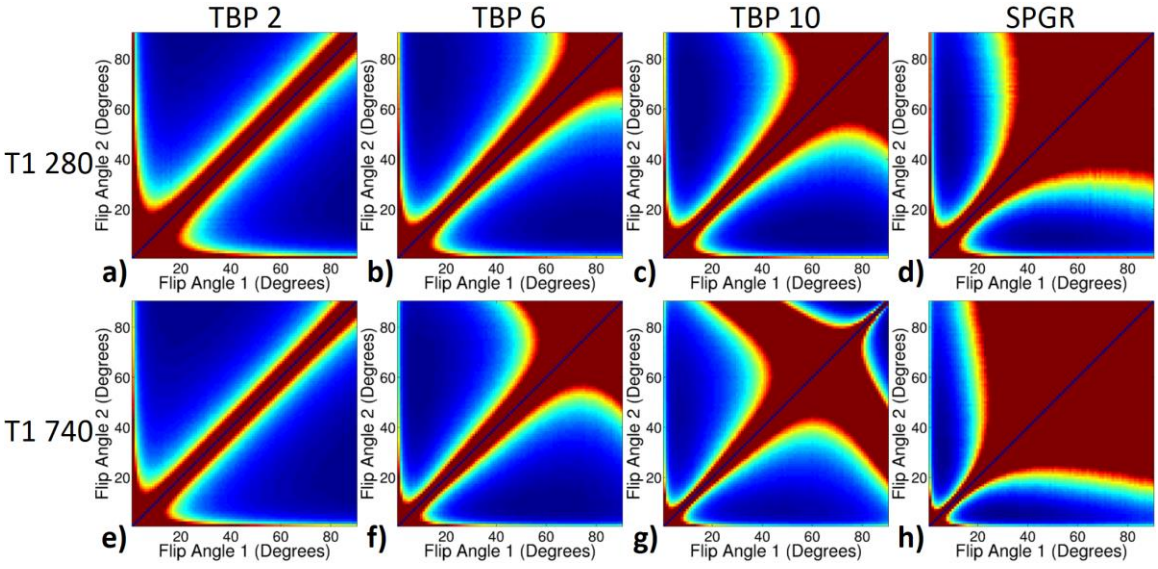

Figure 4.8 – Monte Carlo simulations of standard deviation of T_1 for every combination of flip angles using flip angle correction. Results are displayed as SNR multiplied by the fractional error of true T_1. a-d) T_1 = 280 ms a) TBP 2, b) TBP 6, c) TBP 10, d) SPGR. e-h) T_1 = 740 ms e) TBP 2, f) TBP 6, g) TBP 10, h) SPGR. Flip angles shown are desired flip angle.

desired. This signal contribution increases with flip angle and becomes significant when the desired angle is larger than the Ernst angle. This extra signal creates a total signal vs. flip angle relationship that is not accurately described by the SPGR steady state signal equation and, therefore introduces errors in measurements of T_1. The initial investigation of the VFA technique by Fram et al. (11) was done with a single slice. At that time, their largest source of error was the incomplete spoiling of the residual magnetization, resulting in significant error in T_1 due to the deviation in signal from the SPGR equation. They recognized a residual nonlinearity in their plots of signal/sin(α) vs. signal/tan(α) including the variation in signal across the slice as one of the possible causes. Plots of the simulated data from Figure 4.3 as signal/sin(α) vs. signal/tan(α) show the same nonlinearity, strongly indicating that their observed residual nonlinearity was, in fact, due to the nonuniform slice excitation profile.

A flip angle correction technique which assumes that the total signal in the slice is based on the average flip angle experienced in the slice was used to attempt to correct for the imperfect slice excitation profile. This correction technique, which is generally used to correct for variations in flip angle due to B1+ inhomogeneity, only resulted in accurate T_1 measurements within a narrow band of angle combinations.

A major observation from this study is the relative dependence of VFA measurement accuracy and precision on flip angle choices for 2D vs. 3D acquisition. For 3D measurements, where the B1 variation across a voxel is small, the T_1 measurement is accurate to the extent that the flip angle can be calibrated. In this case, the optimal (most precise) choice of flip angles are the two that give about 71% of the maximum signal value on either side of the Ernst angle peak (16). Because the optimal

flip angles depend on the TR/T_1 ratio, the two flip angles that result in precise measurements of T_1 for one tissue type, will result in less precision for tissues of different T_1 or even the same tissue if T_1 changes.

For 2D measurements, the accuracy and precision of T_1 measurements are both very dependent on the two flip angles used, as well as the TR/T_1 ratio and the TBP. Increasing TR and/or TBP leads to a wider band of flip angle combinations that result in accurate estimates of T_1. Thus, the best choice of flip angles in a 2D acquisition must be considered in terms of accuracy in addition to precision and are not necessarily near the 71% of maximum. For example, for TBP = 2, the total signal never reduces to 71% of the maximum by 90°, yet can still result in accurate (e.g., +/- 5%) measurements of T_1 within a narrow band of flip angle combinations. A general trend that is observed is that the optimum flip angles are both larger than those used in an equivalent 3D measurement. For example, in terms of both accuracy and precision, the optimum desired (uncorrected) flip angles for TBP = 2 and T_1 = 280 ms are 18° (~83%) and 90° (~82.5%) (in the range from 1° to 90°), for TBP = 10 they are 14° (~87%) and 70° (~63%), and for the ideal SPGR (rectangular slice profile) they are 9° and 49° (both ~71%). Similar to 3D VFA, the error is largely determined by the smaller of the two flip angles (16).

The correction method presented here assumes a linear relationship between the desired flip angle and the effective flip angle. More accurate T_1 calculations might be possible if a more exact, nonlinear relationship could be developed and used. Although the results were also limited to just two T_1 values, it is believed that these results are indicative of the types of errors that would be obtained for a range of T_1

values.

We note that these simulation results are specific to the Hamming windowed sinc RF pulse envelope and resulting profile shape considered in this paper, and are only an example of the errors that can occur with different RF pulse envelopes that have different profiles. But all finite duration pulses will have some nonuniformity in excitation profile and will therefore result in measurement errors. The results presented are qualitatively indicative of the errors that can be expected.

Finally, although this paper demonstrates that accurate values of T_1 can be obtained using the VFA method in 2D, these accurate values are only obtained in a narrow band of flip angle combinations. Large errors will occur if there are variations in the flip angle across the slice. That is, simply correcting for the variation in B1+ throughout the slice does not compensate for regions in the slice where the flip angle varies out of the "accurate" band of angles. Until a better correction method can be obtained, these results demonstrate that accurate measurements of T_1 are more likely obtained by a thin slab 3D VFA acquisition than from multiple-slice 2D acquisitions.

4.6 Conclusion

The slice excitation profile is a significant factor in the accuracy of T_1 measurements using the VFA method in a 2D acquisition. T_1 measurement errors occur due to the large flip angle variation within each voxel of the 2D slice. The flip angle correction method detailed here compensates for B1+ inhomogeneity as well as providing a first order compensation for the error due to the imperfect slice excitation profile. Even with this correction only a narrow band of angle combinations results in accurate T_1. As TBP increases, the band of accurate flip angle combinations widens.

When large variations in B1+ occur across the slice, the correction methods discussed in this paper will not work to restore accurate T_1 measurements.

4.7 References

1. Diakite M, Payne A, Todd N, Parker DL. Irreversible change in the T1 temperature dependence with thermal dose using the proton resonance frequency-T1 technique. Magn Reson Med 2013;69(4):1122-1130.

2. Spencer RG, Fishbein KW. Measurement of spin-lattice relaxation times and concentrations in systems with chemical exchange using the one-pulse sequence: breakdown of the Ernst model for partial saturation in nuclear magnetic resonance spectroscopy. J Magn Reson 2000;142(1):120-135.

3. Bellamy DD, Pereira RS, McKenzie CA, Prato FS, Drost DJ, Sykes J, Wisenberg G. Gd-DTPA bolus tracking in the myocardium using T1 fast acquisition relaxation mapping (T1 FARM). Magn Reson Med 2001;46(3):555-564.

4. Schabel MC, Parker DL. Uncertainty and bias in contrast concentration measurements using spoiled gradient echo pulse sequences. Phys Med Biol 2008;53(9):2345-2373.

5. Vrenken H, Geurts JJ, Knol DL, van Dijk LN, Dattola V, Jasperse B, van Schijndel RA, Polman CH, Castelijns JA, Barkhof F, Pouwels PJ. Whole-brain T1 mapping in multiple sclerosis: global changes of normal-appearing gray and white matter. Radiology 2006;240(3):811-820.

6. Rieke V, Butts Pauly K. MR thermometry. J Magn Reson Imaging 2008;27(2):376-390.

7. Treier R, Steingoetter A, Fried M, Schwizer W, Boesiger P. Optimized and combined T1 and B1 mapping technique for fast and accurate T1 quantification in contrast-enhanced abdominal MRI. Magn Reson Med 2007;57(3):568-576.

8. Brix G, Schad LR, Deimling M, Lorenz WJ. Fast and precise T1 imaging using a TOMROP sequence. Magn Reson Imaging 1990;8(4):351-356.

9. Hardy CJ, Edelstein WA, Vatis D, Harms R, Adams WJ. Calculated T1 images derived from a partial saturation-inversion recovery pulse sequence with adiabatic fast passage. Magn Reson Imaging 1985;3(2):107-116.

10. Young IR, Hall AS, Bydder GM. The design of a multiple inversion recovery sequence for T1 measurement. Magn Reson Med 1987;5(2):99-108.

11. Fram EK, Herfkens RJ, Johnson GA, Glover GH, Karis JP, Shimakawa A, Perkins TG, Pelc NJ. Rapid calculation of T1 using variable flip angle gradient refocused imaging. Magn Reson Imaging 1987;5(3):201-208.

12. Cheng HL, Wright GA. Rapid high-resolution T(1) mapping by variable flip angles: accurate and precise measurements in the presence of radiofrequency field inhomogeneity. Magn Reson Med 2006;55(3):566-574.

13. Deoni SC, Peters TM, Rutt BK. High-resolution T1 and T2 mapping of the brain in a clinically acceptable time with DESPOT1 and DESPOT2. Magn Reson Med 2005;53(1):237-241.

14. Deoni SC, Rutt BK, Jones DK. Investigating the effect of exchange and multicomponent T(1) relaxation on the short repetition time spoiled steady-state signal and the DESPOT1 T(1) quantification method. J Magn Reson Imaging 2007;25(3):570-578.

15. Deoni SC, Rutt BK, Peters TM. Rapid combined T1 and T2 mapping using gradient recalled acquisition in the steady state. Magn Reson Med 2003;49(3):515-526.

16. Schabel MC, Morrell GR. Uncertainty in T(1) mapping using the variable flip angle method with two flip angles. Phys Med Biol 2009;54(1):N1-8.

17. Venkatesan R, Lin W, Haacke EM. Accurate determination of spin-density and T1 in the presence of RF-field inhomogeneities and flip-angle miscalibration. Magn Reson Med 1998;40(4):592-602.

18. Parker GJ, Barker GJ, Tofts PS. Accurate multislice gradient echo T(1) measurement in the presence of non-ideal RF pulse shape and RF field nonuniformity. Magn Reson Med 2001;45(5):838-845.

19. Todd N, Diakite M, Payne A, Parker DL. Hybrid proton resonance frequency/T1 technique for simultaneous temperature monitoring in adipose and aqueous tissues. Magn Reson Med 2013;69(1):62-70.

CHAPTER 5

RESPIRATION ARTIFACT CORRECTION IN THREE-DIMENSIONAL PROTON RESONANCE FREQUENCY MR THERMOMETRY USING PHASE NAVIGATORS

This chapter is a reproduction of the paper titled, "Respiration Artifact Correction in Three-Dimensional Proton Resonance Frequency MR Thermometry Using Phase Navigators", authored by Bryant T. Svedin, Allison Payne and Dennis L. Parker, which is published in the journal Magnetic Resonance in Medicine, Vol.76, No.1, July 2016, pages 206-213.

5.1 Abstract

Purpose: To develop reliable three-dimensional (3D) segmented echo planar imaging (seg-EPI) proton resonance frequency (PRF) temperature monitoring in the presence of respiration-induced B0 variation. Methods: A free induction decay (FID) phase navigator was inserted into a 3D seg-EPI sequence before and after EPI readout to monitor B0 field variations. Using the field change estimates, the phase of each k-space line was adjusted to remove the additional phase from the respiratory induced off-resonance. This correction technique was evaluated while heating with MR-guided focused ultrasound (MRgFUS) in phantoms with simulated breathing and during nonheating conditions in healthy in vivo breasts. Results: With k-space phase

correction, the standard deviation of magnitude images and PRF temperature measurements in breast from five volunteers improved by an average factor of 1.5 and 2.1, respectively. Improved accuracy of temperature estimates was observed after correction while heating with MRgFUS in phantoms. Conclusion: Phase correction based on two FID navigators placed before and after the echo train provides promising results for implementing 3D monitoring of thermal therapy treatments in the presence of field variations due to respiration.

5.2 Introduction

The proton resonance frequency (PRF) shift method (1) has been widely adopted to measure temperature changes in tissue during thermal therapy treatments due to its linearity over the temperature range of interest, the constant of proportionality being largely independent of tissue type (except adipose tissue) (2), and its ability to produce temperature maps with the spatial and temporal resolution required to monitor treatments in real time. PRF temperature mapping interprets any phase change as a change in temperature and is therefore susceptible to errors from any phase changes that are not temperature induced, such as motion. Even when there is no motion within the imaged volume, such as when imaging a stationary breast or brain, phase changes induced by respiratory motion have been shown to produce artifacts (3-9). Respiratory-induced motion of the abdomen and lungs change the distribution of magnetic susceptibility, altering the B_0 field and corresponding resonant frequency distribution throughout the subject including the nonmoving imaged volume. Each frequency offset results in an added linear phase evolution during readout that changes between excitations, causing ghosting artifacts. This was

investigated in the breast by Peters et al. (4), who measured an average field fluctuation of 0.13 ppm during regular respiration throughout the breast. Similar but smaller field fluctuations have also been observed in the brain (7,10).

Several methods have been proposed to correct the respiration-induced B_0 variation in the breast (3,6,8). Although these correction schemes were successful, they all required a library of baseline images that adequately characterized the entire respiration period and were all limited to two-dimensional (2D) single slice imaging, limiting the monitored region. Although this 2D field of view results in a short temporal resolution that can adequately capture the respiratory cycle, it restricts the volume of tissue monitored during thermal therapies.

3D PRF sequences offer some important advantages over 2D methods, but have several challenges that must be overcome. 3D acquisitions can provide high spatial resolution sampling over the target volume and a larger field of view, which is advantageous for thermal therapy techniques, in general, to assess the effectiveness and safety of the treatment. However, three-dimensional (3D) acquisitions can require longer acquisition times, reducing temporal resolution and making the images more susceptible to artifacts from subject motion. Echo-planar imaging (EPI) sequences are often used to increase temporal resolution while maintaining the larger field of view. Because of the low phase encoding sampling bandwidth, EPI sequences can have increased sensitivity to phase errors due to B_0 variations. The amount of off-resonance varies continuously with respiration, and if the image acquisition is faster than the field variation, the phase error in each image could potentially be corrected using a multibaseline method. However, when the total acquisition time covers a significant

portion of one or multiple respiratory cycles, the phase variations cause ghosting. In addition, the slice orientation of the imaging volume during EPI acquisitions has a strong impact on respiration-induced artifacts (7).

The B_0 shift due to respiration can be measured using navigator acquisitions. Several navigator methods have been used for motion correction (11,12), to reduce signal fluctuation (13), and improve image quality (14,15). Some methods use free induction decay (FID) navigators (16), whereas others applied a gradient during navigator readout (11,15,17) or extracted the navigator information from the k-space data itself (ie, they are self-navigated) (10,18,19). These methods use navigator information to estimate the phase at the signal echoes and subsequently remove the unwanted phase.

In this study, we developed an improved method that corrects respiratory induced phase variations in a 3D seg-EPI sequence by collecting two internal FID phase correction navigators--one before the EPI readout and one after--to estimate the respiration-induced field change. This technique improves upon other methods by acquiring a 3D image volume with a relatively short temporal resolution without the need for a library of baseline images. The ability of the phase correction navigators to estimate respiration-induced field shifts in the breast in vivo was demonstrated in healthy volunteers. The accuracy of temperature measurements using the correction technique during MRgFUS is demonstrated using phantom studies.

5.3 Methods

5.3.1 Phase Navigator

A 3D seg-EPI sequence was modified to include flyback EPI readout and two internal phase correction navigators as shown in Figure 5.1a. The flyback readout ensures that the fat chemical shift is always in the same direction and eliminates the need for standard EPI phase correction. The navigators have no gradients during readout and provide an estimate of the average phase over the sensitive volume of each channel in the receiver array. Phase correction is performed by assuming a uniform shift in B_0 and resulting frequency offset over the sensitive area of each coil. Although it has been shown that the B_0 offset varies spatially (4), making this assumption slightly erroneous, using an array of coils as is done in this study does provide some spatial sensitivity to the off-resonance measurement.

An outline of this correction method is shown in Figure 5.1. The phase difference between the two FIDs consists of a constant phase difference due to the offset of the image and a variable phase due to the frequency variation with respiration. An example of the phase of the two FIDs is shown in Figure 5.1b. The navigator signal measured by the j^{th} coil after removing the Larmor frequency is described using the equation

$$S_j(t) = \int_{volume} c_j(\boldsymbol{x}) m(\boldsymbol{x}, t) e^{-i\gamma \int_0^t \Delta B(\boldsymbol{x},\tau) d\tau} d\boldsymbol{x} \qquad [5.1]$$

where c_j is the j^{th} coil sensitivity, $m(\boldsymbol{x}, t)$ is the magnetization distribution, and $\Delta B(\boldsymbol{x}, t)$ is the field shift. The phase difference between the two navigators was calculated by multiplying the second navigator by the complex conjugate of the first navigator using Equation [5.2], where it is assumed that the field shift is constant over

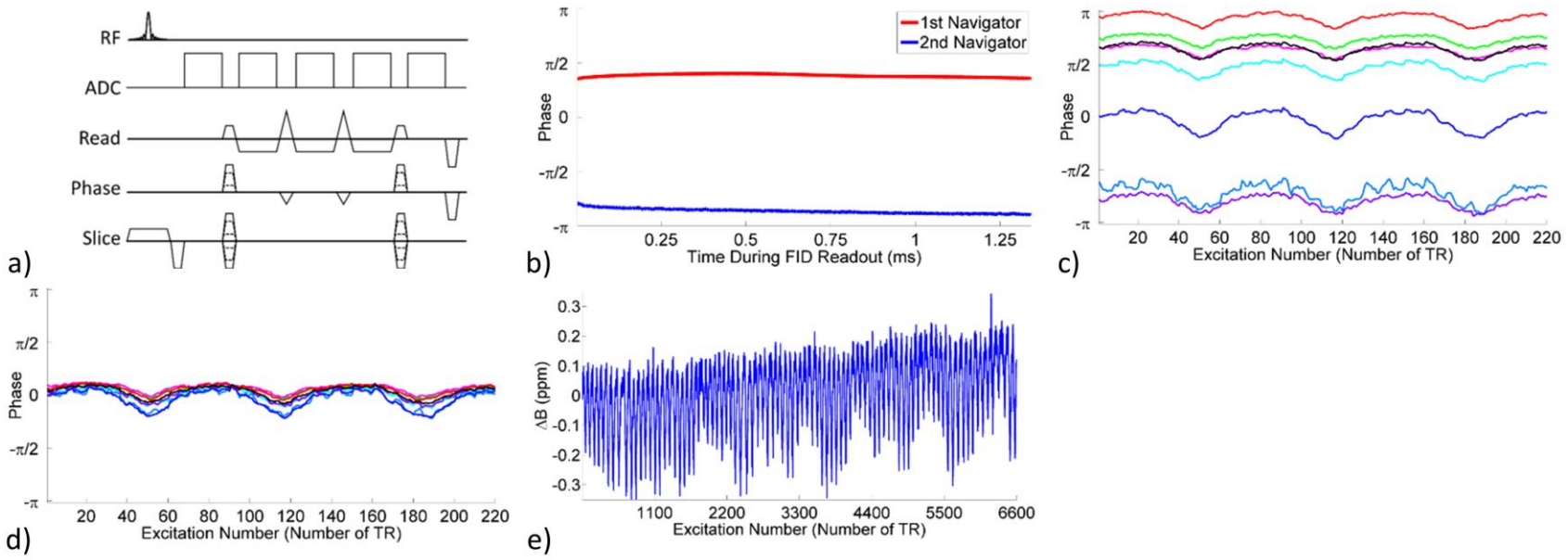

Figure 5.1. a) Modified segmented EPI sequence with flyback readout. FID phase navigator readouts are acquired before and after EPI readout. b) Example of phase during navigator readout for a single TR. c) Example of average phase difference estimate for 8 coils during one image acquisition. d) Example of phase variation about constant phase difference for 8 coils during one image acquisition. e) Example of field shift (in ppm) for one coil over 30 image acquisitions.

space and time during each repetition time:

$$\Delta\varphi_j = \angle\left(S_j^2 S_j^{1^*}\right) = \angle(e^{-i\gamma\Delta B(t_2-t_1)}) \quad [5.2]$$

Measurement error is reduced by taking the average phase difference of corresponding samples in each FID. Figure 5.1c shows an example of the phase difference during one image acquisition for each of the eight receiver coils. In addition to the phase variation with respiration, there is a constant phase difference between the channels due to the small spatial variation in B_0 (imperfect shim) between sensitive volumes. The constant phase difference between each coil is removed by a baseline correction. The average phase difference of the first image is used as a baseline, subtracting from all subsequent image acquisitions for each receiver coil. Note that this method also measures and corrects for a weighted average B_0 field drift for each coil (weighted somewhat by the coil sensitivities).

After removing the constant phase difference $\Delta\,\varphi_{j,const}$, the remaining phase variation is primarily due to temporal B_0 variation, as shown in Figure 5.1d. The field shift is calculated using the equation

$$\Delta B_j = \frac{\Delta\varphi_j - \Delta\,\varphi_{j,const}}{\gamma\Delta t} \quad [5.3]$$

where $\Delta\varphi$ is the phase difference, γ is the gyromagnetic ratio, and Δt is the time difference between navigator readouts. The field shift is shown in parts per million (ppm) in Figure 5.1e.

After excitation, phase accumulates linearly in time by $\varphi(t) = \Delta B * \gamma * t$. The phase of the k-space lines acquired for each excitation is adjusted to remove the extra phase accumulated due to respiration at their individual read time in the echo train, incorporating echo shifting. The field offset ΔB is calculated and used for correcting

each coil separately. After adjusting the signal phase, the corrected signal is described using the equation

$$S_j(k_x, k_y) = \int_{volume} c_j(\boldsymbol{x}) m(\boldsymbol{x}, t) e^{-i\gamma \int_0^t [\Delta B(\boldsymbol{x},\tau) - \Delta B_j] d\tau} e^{-i2\pi(k_x x + k_y y)} d\boldsymbol{x} \quad [5.4]$$

where ΔB_j is measured every excitation.

5.3.2 Experiments

To demonstrate the ability of the phase navigators to correct respiration-induced artifacts, two types of experiments were performed. The first experiment evaluated the correction in the breast during nonheating conditions, and the second experiment evaluated the correction technique during MRgFUS heating in both a gelatin and salt pork phantom. In this situation, a male volunteer was positioned above the phantom setup to create the respiration artifact while heating with MRgFUS. All experiments were performed in a Siemens TIM Trio 3T MRI scanner (Siemens Medical Solutions, Erlangen, Germany) using a breast-specific MRgFUS system with an integrated eight-channel RF coil and an MRI-compatible phased array transducer (256 elements, 1 MHz frequency, 13 cm radius of curvature; Imasonic, Besançon, France and Image Guided Therapy, Pessac, France) (20-22). All human studies were approved by the local Institutional Review Board (IRB) and performed with informed consent.

5.3.3 In Vivo Breast Nonheating Experiments

Five healthy female volunteers (age range, 29–50 y) were positioned head-first in the breast-specific MRgFUS device in the prone position. After localization,

multiple 3D seg-EPI GRE image volumes were acquired in the coronal orientation with no ultrasound applied while the volunteer was free breathing (voxel spacing = 1 x 1 x 3 mm; field of view = 224 x 154 x 24 mm; matrix = 224 x 154 x 10, flip angle = 20°, repetition time [TR]/echo time [TE] = 47/15 ms; EPI Factor = 7, 8 slices with 25% oversampling; readout bandwidth = 744 Hz/pixel; phase encoding bandwidth = 56 Hz/pixel; spectral fat saturation pulse applied before every TR; 30 repetitions; 10.3 s per image). Volunteer 1 moved several times during the first 19 image acquisitions, and volunteer 2 moved during the seventh image acquisition, causing image misregistration; therefore, only the last 11 and 23 images were used for these two volunteers, respectively. PRF temperature estimates were calculated using the first of the remaining images as the reference phase. Three-point Dixon data were acquired using the same imaging parameters with TE = 16/17.2/18.4 ms and no fat saturation pulses. These data were used to calculate separate water and fat images. After shifting the fat images to compensate for the large chemical shift artifact present in seg-EPI data, these images were used for tissue segmentation. Only the PRF temperature estimates within water and glandular tissue were used to analyze the effectiveness of the correction method.

5.3.4 MRgFUS Phantom Experiments

The correction technique was evaluated during heating conditions using both a gelatin phantom (23) and an excised pork sample that contained significant amounts of both fat and aqueous tissues. In order to simulate respiration effects, a male volunteer lay prone above the breast-specific MRgFUS device breathing freely during the ultrasound sonications. A separation gap of approximately 5 mm was intentionally

left between the phantom and the chest of the volunteer, eliminating any possible heating of the volunteer and reducing the possibility of bulk phantom motion during the heating period while allowing respiration-induced variation of B_0. The 3D imaging volume was prescribed in a coronal orientation with the same imaging parameters that were used in the in vivo breast nonheating experiment. For the gelatin phantom, we used the same 3D seg-EPI sequence with the same MR parameters as for the volunteers except for the following: field of view = 224 x 154 x 24 mm; matrix = 224 x 154 x 10; TR/TE = 32/15 ms; no fat saturation; 7 s per image. Four sets of data were collected for both the gelatin and excised pork phantoms. For comparison, two image sets were acquired without the volunteer placed above the phantom. The first image set served as a control without FUS heating or breathing artifact. The second set provided a baseline of the MRgFUS heating (25 acoustic W, 60 s) without the breathing artifact. The third and fourth image sets repeated imaging sets one and two with the volunteer above simulating respiration effects. The pork phantom was unintentionally displaced ~1-2 mm while placing the volunteer above, causing a slight position shift between the breathing and non-breathing situation. The PRF temperatures were determined using the average phase of five baseline images obtained with no ultrasound heating as the reference phase.

5.4 Results

In the five female volunteers, it was found that the field shift amplitude was patient specific. While the field shift values shown in Figure 5.1d (volunteer 5), as well as volunteer 3, oscillated with an amplitude of approximately 0.2 ppm, volunteers 1, 2, and 4 had amplitudes of 0.1 ppm, 0.1 ppm, and 0.15 ppm, respectively, likely

indicating a variation of inhalation volume.

Results for the five female volunteers are shown in Figure 5.2. All images are of the center acquired slice for each volunteer. The top two rows show the uncorrected (top) and corrected (bottom) magnitude images. The middle two rows show the standard deviation of the magnitude as a percent of the average magnitude value, for uncorrected (top) and corrected (bottom). The bottom two rows show the PRF standard deviation in °C for uncorrected (top) and corrected (bottom) for water and glandular tissue. The incorporation of navigator phase correction reduced the ghosting artifact in the magnitude images for all volunteers, as shown by the reduction of the magnitude standard deviation. The standard deviation of magnitude within the breast was improved by an average factor ranging from 1.34 to 1.84 for the five volunteers. The PRF temperature precision was also improved. The standard deviation of PRF temperature estimates within glandular tissue was improved by an average factor ranging from 1.67 to 2.45 for the five volunteers. The values for each volunteer are shown in Table 5.1.

The PRF temperature precision images for the phantom studies without MRgFUS heating comparing the cases with and without a volunteer above are shown in Figure 5.3. PRF temperature estimates versus measurement number for an example single voxel near the center of each phantom for gelatin and pork are shown in Figure 5.3b and 5.3c, respectively. The mean PRF standard deviation inside the gelatin and pork in each case is shown in Table 5.2.

Figure 5.4a shows the phantom results during MRgFUS heating. The PRF temperature map for the peak temperature voxel measurement, with and without

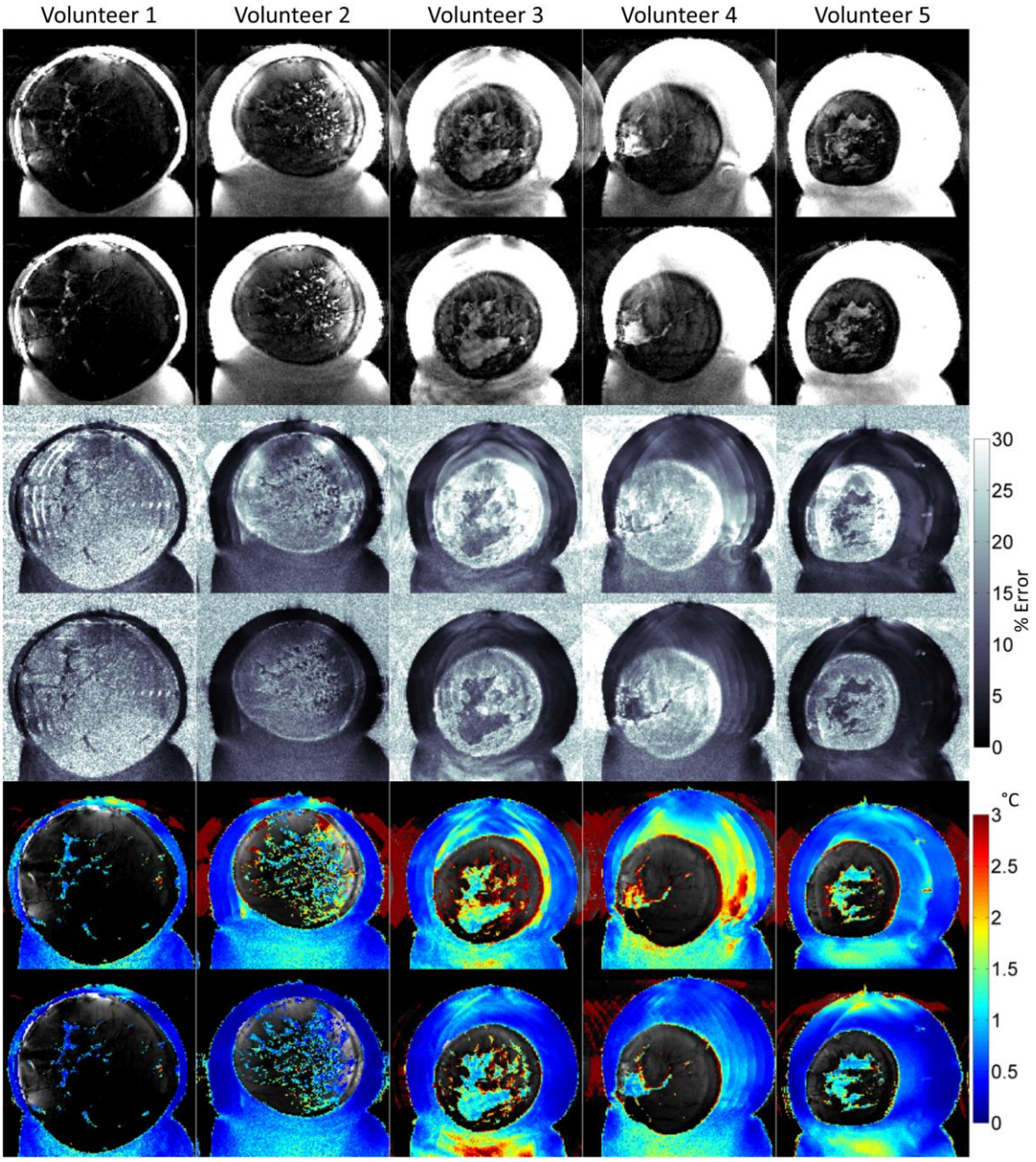

Figure 5.2. In vivo breast images for the five healthy volunteers. Top two row: Magnitude images uncorrected (top row) and corrected (bottom row). Middle two rows: Standard deviation of magnitude uncorrected (top row) and corrected (bottom row). The color scale indicates the percent of the mean signal value. Bottom two rows: Standard deviation of PRF temperature estimates in water and glandular tissue (°C) uncorrected (top row) and corrected (bottom row).

Table 5.1
Comparison of in vivo breast results

Volunteer	Mean Magnitude SD Improvement Factor	Maximum Magnitude SD Improvement Factor	Mean PRF SD Improvement Factor	Maximum PRF SD Improvement Factor
1	1.36 ± 0.52	12.5	1.67 ± 1.14	27.4
2	1.84 ± 0.97	13.7	2.45 ± 2.67	64.2
3	1.40 ± 0.52	5.4	2.14 ± 1.86	25.0
4	1.34 ± 0.37	5.0	2.16 ± 1.63	23.3
5	1.70 ± 0.58	6.7	1.92 ± 1.59	25.2

Abbreviations: SD, standard deviation

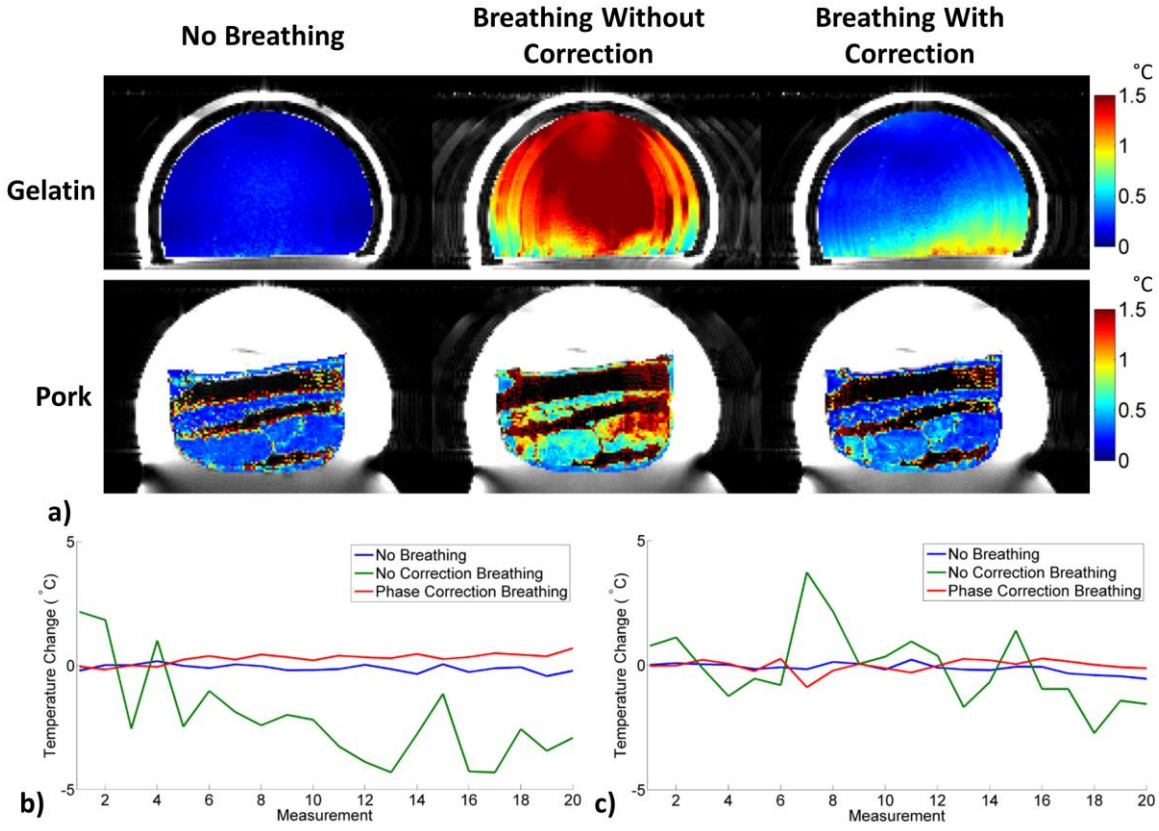

Figure 5.3. Phantoms under nonheating conditions. (a) PRF temperature precision images for gelatin and pork comparing the no breathing, breathing without correction, and breathing with correction cases without FUS heating. (b) PRF temperature change of a single voxel in gelatin phantom for all three cases. (c) PRF temperature change of a single voxel in pork phantom for all three cases.

Table 5.2
Phantom results

Case	Gelatin PRF Mean SD ±SD °C	Pork PRF Mean SD ±SD °C
No Breathing	0.17 ± 0.09	0.25 ± 0.10
Breathing without correction	1.36 ± 0.28	1.01 ± 0.66
Breathing with correction	0.39 ± 0.23	0.45 ± 0.32

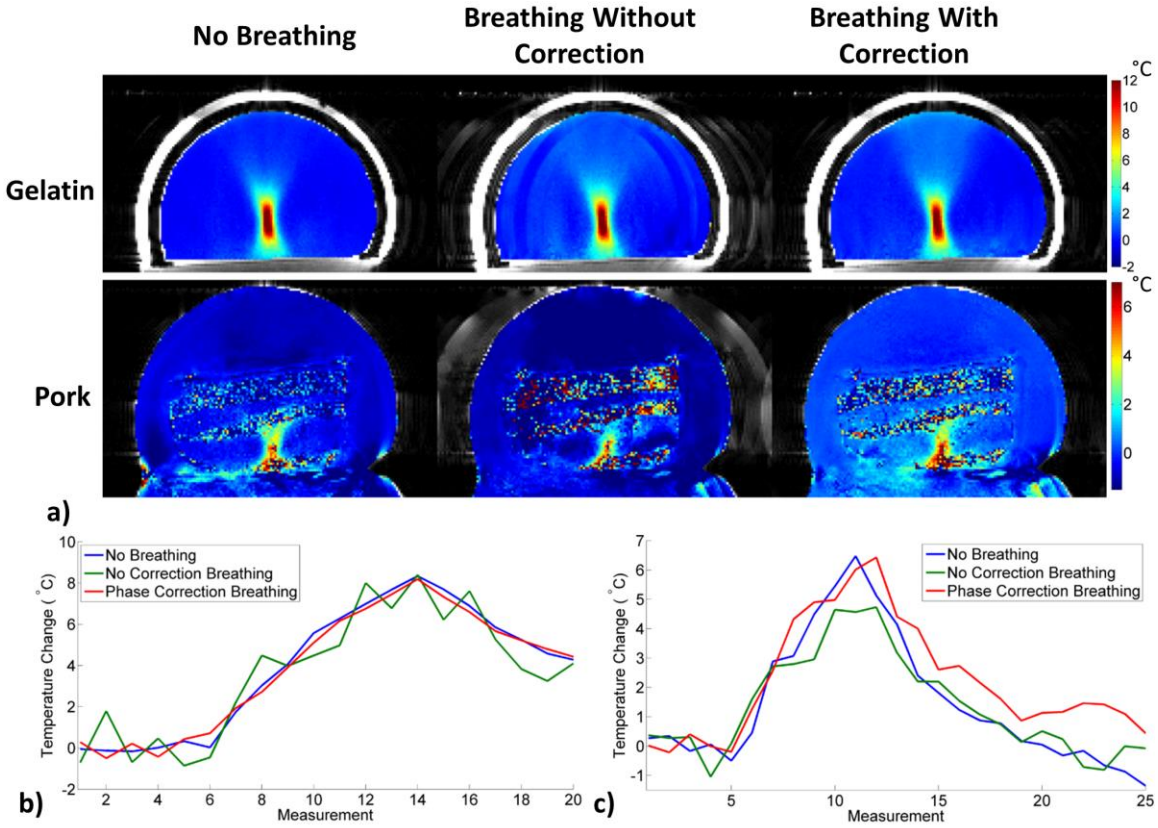

Figure 5.4. MRgFUS phantom experiments. (a) PRF temperature change images at the time of the peak temperature for gelatin and pork comparing the no breathing, breathing without correction, and breathing with correction cases with MRgFUS heating. (b) PRF temperature change of a single voxel in gelatin phantom for all three cases. (c) PRF temperature change of a single voxel in pork phantom for all three cases.

simulated respiration for both the gelatin phantom and excised pork are shown. The off-resonance due to respiration introduced greater error to the PRF measurements of the sonicated area (Figure 5.4b and 5.4c).

5.5 Discussion

Our results show that image magnitude, phase, and PRF measurement artifacts caused by respiration induced B_0 variations during 3D seg-EPI image acquisition can be reduced using two internal FID phase navigators that are acquired at the start and end of each echo train. In the breast of the five volunteers, there were improvements to the standard deviation of image magnitude by an average factor of 1.52, as well as the standard deviation of the temperature estimate by an average factor of 2.1. The inclusion of two internal FID phase navigators had a minimal impact on scan time by adding approximately 1 and 2 ms to TE and TR, respectively. The impact on scan time could be minimized further by acquiring fewer samples in the FID.

The field shift oscillation amplitudes of the breast volunteers before respiratory correction are in the same range and agree with findings by Peters et al. and Bolan et al. (4,24). In our phantom studies, the PRF precision after correction was comparable to the control cases without the volunteer above; therefore, there were no respiratory artifacts. When heating with MRgFUS, the breathing with correction temperature estimates were nearly identical to the nonbreathing case within the sonicated area in the gelatin phantom. The pork phantom also showed significant improvement to temperature estimates within the sonicated area. It is assumed the efficiency of this correction method decreases as the spatial variation of the off-resonance increases. Each receiver channel measures its own field shift for its region of sensitivity. This

study focused on coronal acquisitions within the breast, which did not have motion within the imaging volume. This method may not be as effective with a transverse or sagittal slab in the breast, as respiratory motion (a different artifact) may be within the field of view, as well as possible decreased uniformity of the field shift over the sensitive region of each coil.

Although several published techniques have used a navigator, many of them focused on motion correction (11,12) or improving functional MRI signal (17,18,25,26) and were either self-navigated or used a single navigator per TR. In our method, the phase changes due to echo shifting during seg-EPI readouts (to reduce abrupt phase transitions in k-space) necessitated the use of two internal navigators to calculate the phase difference, instead of simply calculating the difference between navigators in subsequent TRs.

Although 2D image acquisitions offer greater time resolution, which is very important in thermal therapy treatments, they often lack the spatial coverage needed to measure temperature in all areas that could be affected during treatment. The method presented here offers 3D images corrected for respiration artifacts, which could increase patient safety by allowing more volume coverage during treatment. The temporal resolution of the in vivo breast images and pork phantom studies was 10.3 s and the gelatin phantom was 7 s. These could be reduced using parallel acquisition methods (27-29), temporally constrained reconstruction (30,31), model predictive filtering (32,33), or decreased resolution (34). Phase navigators could be used with any of these methods as long as the phase correction was applied before the reconstruction algorithm and would theoretically not interfere with their effectiveness. A time

reduction factor of 2 or 3 could potentially be sufficient for near real-time monitoring. This method could also theoretically be applied to 2D acquisitions, supplementing or removing the need for a multi-baseline library.

5.6 Conclusion

Our proposed method provides promising results for implementing 3D monitoring of thermal therapy treatments while allowing free breathing. PRF temperature precision was improved using phase correction navigators in both phantom studies and in vivo breast. Ghosting artifacts in the magnitude and phase images were mostly removed. This technique could apply to other stationary targets with nearby motion in addition to breast.

5.7 References

1. Ishihara Y, Calderon A, Watanabe H, Okamoto K, Suzuki Y, Kuroda K, Suzuki Y. A precise and fast temperature mapping using water proton chemical shift. Magn Reson Med 1995;34(6):814-823.

2. Peters RD, Hinks RS, Henkelman RM. Ex vivo tissue-type independence in proton-resonance frequency shift MR thermometry. Magn Reson Med 1998;40(3):454-459.

3. Hey S, Maclair G, de Senneville BD, Lepetit-Coiffe M, Berber Y, Kohler MO, Quesson B, Moonen CT, Ries M. Online correction of respiratory-induced field disturbances for continuous MR-thermometry in the breast. Magn Reson Med 2009;61(6):1494-1499.

4. Peters NH, Bartels LW, Sprinkhuizen SM, Vincken KL, Bakker CJ. Do respiration and cardiac motion induce magnetic field fluctuations in the breast and are there implications for MR thermometry? J Magn Reson Imaging 2009;29(3):731-735.

5. Raj D, Paley DP, Anderson AW, Kennan RP, Gore JC. A model for susceptibility artefacts from respiration in functional echo-planar magnetic resonance imaging. Phys Med Biol 2000;45(12):3809-3820.

6. Shmatukha AV, Bakker CJ. Correction of proton resonance frequency shift temperature maps for magnetic field disturbances caused by breathing. Phys Med Biol 2006;51(18):4689-4705.

7. Van de Moortele PF, Pfeuffer J, Glover GH, Ugurbil K, Hu X. Respiration-induced B0 fluctuations and their spatial distribution in the human brain at 7 Tesla. Magn Reson Med 2002;47(5):888-895.

8. Vigen KK, Daniel BL, Pauly JM, Butts K. Triggered, navigated, multi-baseline method for proton resonance frequency temperature mapping with respiratory motion. Magn Reson Med 2003;50(5):1003-1010.

9. Wyatt CR, Soher BJ, MacFall JR. Correction of breathing-induced errors in magnetic resonance thermometry of hyperthermia using multiecho field fitting techniques. Med Phys 2010;37(12):6300-6309.

10. Wowk B, McIntyre MC, Saunders JK. k-Space detection and correction of physiological artifacts in fMRI. Magn Reson Med 1997;38(6):1029-1034.

11. Ehman RL, Felmlee JP. Adaptive technique for high-definition MR imaging of moving structures. Radiology 1989;173(1):255-263.

12. Korin HW, Felmlee JP, Ehman RL, Riederer SJ. Adaptive technique for three-dimensional MR imaging of moving structures. Radiology 1990;177(1):217-221.

13. Hu X, Kim SG. Reduction of signal fluctuation in functional MRI using navigator echoes. Magn Reson Med 1994;31(5):495-503.

14. Kim WS, Mun CW, Kim DJ, Cho ZH. Extraction of cardiac and respiratory motion cycles by use of projection data and its applications to NMR imaging. Magn Reson Med 1990;13(1):25-37.

15. Versluis MJ, Sutton BP, de Bruin PW, Bornert P, Webb AG, van Osch MJ. Retrospective image correction in the presence of nonlinear temporal magnetic field changes using multichannel navigator echoes. Magn Reson Med 2012;68(6):1836-1845.

16. Boulant N, Bottlaender M, Uhrig L, Giacomini E, Luong M, Amadon A, Massire A, Larrat B, Vignaud A. FID navigator-based MR thermometry method to monitor small temperature changes in the brain of ventilated animals. NMR Biomed 2015;28(1):101-107.

17. Hu X, Le TH, Parrish T, Erhard P. Retrospective estimation and correction of physiological fluctuation in functional MRI. Magn Reson Med 1995;34(2):201-212.

18. Durand E, van de Moortele PF, Pachot-Clouard M, Le Bihan D. Artifact due to B(0) fluctuations in fMRI: correction using the k-space central line. Magn Reson Med 2001;46(1):198-201.

19. Le TH, Hu X. Retrospective estimation and correction of physiological artifacts in fMRI by direct extraction of physiological activity from MR data. Magn Reson Med 1996;35(3):290-298.

20. Payne A, Merrill R, Minalga E, Vyas U, de Bever J, Todd N, Hadley R, Dumont E, Neumayer L, Christensen D, Roemer R, Parker D. Design and characterization of a laterally mounted phased-array transducer breast-specific MRgHIFU device with integrated 11-channel receiver array. Med Phys 2012;39(3):1552-1560.

21. Payne A, Todd N, Minalga E, Wang Y, Diakite M, Hadley R, Merrill R, Factor R, Neumayer L, Parker DL. In vivo evaluation of a breast-specific magnetic resonance guided focused ultrasound system in a goat udder model. Med Phys 2013;40(7):073302.

22. Minalga E, Payne A, Merrill R, Todd N, Vijayakumar S, Kholmovski E, Parker DL, Hadley JR. An 11-channel radio frequency phased array coil for magnetic resonance guided high-intensity focused ultrasound of the breast. Magn Reson Med 2013;69(1):295-302.

23. Farrer A, de Bever J, Coats B, Christenson D, Payne A. Fabrication and Evaluation of Tissue-Mimicking Phantoms for Use with MR-ARFI and MRgFUS. Proceedings of the 14th International Symposium of Therapeutic Ultrasound, Las Vegas, Nevada, USA, 2014. p. 232.

24. Bolan PJ, Henry PG, Baker EH, Meisamy S, Garwood M. Measurement and correction of respiration-induced B0 variations in breast 1H MRS at 4 Tesla. Magn Reson Med 2004;52(6):1239-1245.

25. Pfeuffer J, Van de Moortele PF, Ugurbil K, Hu X, Glover GH. Correction of physiologically induced global off-resonance effects in dynamic echo-planar and spiral functional imaging. Magn Reson Med 2002;47(2):344-353.

26. Ramsey NF, van den Brink JS, van Muiswinkel AM, Folkers PJ, Moonen CT, Jansma JM, Kahn RS. Phase navigator correction in 3D fMRI improves detection of brain activation: quantitative assessment with a graded motor activation procedure. Neuroimage 1998;8(3):240-248.

27. Griswold MA, Jakob PM, Heidemann RM, Nittka M, Jellus V, Wang J, Kiefer B, Haase A. Generalized autocalibrating partially parallel acquisitions (GRAPPA). Magn Reson Med 2002;47(6):1202-1210.

28. Pruessmann KP, Weiger M, Scheidegger MB, Boesiger P. SENSE: sensitivity encoding for fast MRI. Magn Reson Med 1999;42(5):952-962.

29. Odeen H, Todd N, Diakite M, Minalga E, Payne A, Parker DL. Sampling strategies for subsampled segmented EPI PRF thermometry in MR guided high intensity focused ultrasound. Med Phys 2014;41(9):092301.

30. Todd N, Adluru G, Payne A, DiBella EV, Parker D. Temporally constrained reconstruction applied to MRI temperature data. Magn Reson Med 2009;62(2):406-419.

31. Todd N, Prakash J, Odeen H, de Bever J, Payne A, Yalavarthy P, Parker DL. Toward real-time availability of 3D temperature maps created with temporally constrained reconstruction. Magn Reson Med 2014;71(4):1394-1404.

32. de Bever J, Todd N, Payne A, Christensen DA, Roemer RB. Adaptive model-predictive controller for magnetic resonance guided focused ultrasound therapy. Int J Hyperthermia 2014;30(7):456-470.

33. Todd N, Payne A, Parker DL. Model predictive filtering for improved temporal resolution in MRI temperature imaging. Magn Reson Med 2010;63(5):1269-1279.

34. Todd N, Vyas U, de Bever J, Payne A, Parker DL. The effects of spatial sampling choices on MR temperature measurements. Magn Reson Med 2011;65(2):515-521.

CHAPTER 6

FOCAL POINT DETERMINATION IN MAGNETIC RESONANCE-GUIDED FOCUSED ULTRASOUND USING TRACKING COILS

This chapter is a reproduction of the paper titled, "Focal Point Determination in Magnetic Resonance-guided Focused Ultrasound Using Tracking Coils", authored by Bryant T. Svedin, Michael J. Beck, J. Rock Hadley, Robb Merrill, Joshua T. de Bever, Bradley D. Bolster Jr., Allison Payne and Dennis L. Parker, which is published in the journal Magnetic Resonance in Medicine, DOI: 10.1002/mrm.26294.

6.1 Abstract

Purpose: To develop a method for rapid prediction of the geometric focus location in MR coordinates of a focused ultrasound (US) transducer with arbitrary position and orientation without sonicating. Methods: Three small tracker coil circuits were designed, constructed, attached to the transducer housing of a breast-specific MR-guided focused US (MRgFUS) system with 5 degrees of freedom, and connected to receiver channel inputs of an MRI scanner. A one-dimensional sequence applied in three orthogonal directions determined the position of each tracker, which was the corrected for gradient nonlinearity. In one transducer position orientation where the tracker positions were also known. Subsequent US focus locations were determined from the isometric transformation of the trackers. The accuracy of this method was

verified by comparing the tracking coil predictions to thermal center of mass calculated using MR thermometry data acquired at 16 different transducer positions for MRgFUS sonications in a homogeneous gelatin phantom. Results: The tracker coil predicted focus was an average distance of 2.1 ± 1.1 mm from the thermal center of mass. The one-dimensional locator sequence and prediction calculations took less than 1 s to perform. Conclusion: This technique accurately predicts the geometric focus for a transducer with arbitrary position and orientation without sonicating.

6.2 Introduction

MR-guided focused ultrasound (MRgFUS) has a wide range of promising applications including the treatment of cancer (1-3), localized drug delivery (4-6), and neuromodulation (7,8). For many of these applications, the treatment time can be long and may require sonicating at several positions with the transducer in multiple physical location. Thus, rapidly finding the physical location of the ultrasound (US) focus is critical to successful interventional treatments. When the orientation of the focused US (FUS) system is monitored with position sensors, the transducer location can be computed directly. Relative to the transducer, the focal spot of table top vertically shooting transducers have been located by calibrating the transducer focus with gelatin phantoms or finding the water spout in a water bath relative to the MRI scanner isocenter and then calculating offset positions into the patient in MRI coordinates (9,10).

For FUS systems without position sensors, two methods of locating the transducer focus are typically used. In one method, the focus location in MRI coordinates is predicted geometrically from scout images showing the transducer

location and orientation. Hand-drawn measurements are made to find the focus location based on the known focal length from the transducer face. This location is highly subjective, depending on 1) scout image resolution, 2) the accuracy of the scout image orientation with respect to the transducer, and 3) the accuracy of a perpendicular line drawn from the center of the transducer face.

In a second method, low-power, short-duration heating or acoustic radiation force impulse (ARFI) imaging (11-13) can also be used to determine the focus location. de Bever et al. (14) demonstrated the ability of a 3D MR-ARFI sequence to determine the position of the focus to within approximately 0.5 mm in a gelatin phantom using a vertically propagating transducer. To be accurate and sensitive, this method required motion encoding and slice encoding gradients to be along the beam propagation path.

Several factors can contribute to the difficulty in focal spot localization when using low-power heating or ARFI. The accuracy of the transducer focus location depends on the acquired image's resolution (15). It has been shown that tissue heterogeneity causes US aberrations which can cause decreased maximum pressure, deformed focal shape, and shifted focal location (16,17). These aberrations increase the difficulty of locating the geometric focus through US sonication. Focus localization with both ARFI and low power heating requires having a reasonable estimate of the focus location from the scout images to effectively position the image volume during sonication. Difficulty of all described methods is increased when the transducer has arbitrary position and orientation.

Dumoulin et al. (18) described a simple method for locating a small receive coil in 3D MR coordinates. This technique has been used extensively in intravascular

catheter tracking (19). In a variant of this technique, Ooi et al. (20) used three small signal generating beads with individual radiofrequency (RF) coils placed on a pair of glasses to follow the motion of the head. During image acquisition, tracking data from the beads were used to prospectively update the position and orientation of the imaging volume to follow the motion of the head. The coils on the glasses were wirelessly coupled to the multi-channel head coil, which limited the viable range of motion to correctly distinguish the small receiver coils. Tracker coils have also been incorporated in FUS systems (21-23). In a system designed for prostate ablation (21,23), the tracker coils were placed in the system housing such that the plane formed by the three coils contained the US focus. A special pulse sequence was used to track the locations of the coils within the imaging volume and to control the image plane to contain the tracker coils in real-time to ensure the focal spot is always within the image.

In this study, we developed a technique to locate the geometric focus of a focused US transducer without position sensors, from the locations of three small RF tracking coils mounted rigidly to the transducer housing. Hardware and software design considerations and predicted focal position accuracy relative to US heating measurements are presented.

6.3 Methods

6.3.1 Hardware

All experiments were performed in a Siemens TIM Trio 3T MRI scanner using a breast-specific MRgFUS system (Figure 6.1) with an integrated eight-channel RF coil and an MRI-compatible phased array transducer (256 elements; frequency = 940

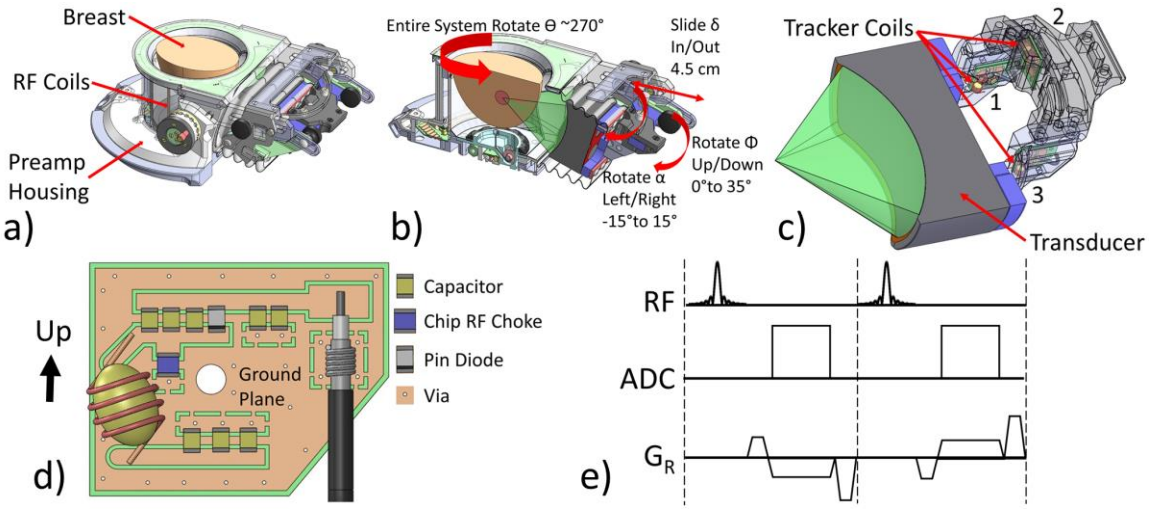

Figure 6.1. a) MRgFUS breast system b) Cross section showing various degrees of freedom. c) Tracker coil arrangement. The transducer is cut in half horizontally to clearly show tracker coils. d) Conceptual circuit design. Coil axis is rotated ~15° from vertical to give maximum signal possible for every transducer position. e) Locator Sequence for one readout direction GR. This is applied along Gx, Gy and Gz to locate the tracker coil.

kHz; radius of curvature = 10 cm; focal length = 10 cm [Imasonic, Besançon, France; Image Guided Therapy, Pessac, France]). This breast-specific MRgFUS system is the second generation of the system previously described in (24-26) and is designed to position the patient prone with either the left or right breast in the treatment cylinder at the MRI scanner isocenter. The transducer is mounted laterally to the breast and the system gives the transducer 5 mechanical degrees of freedom (Figure 6.1b). The entire system can rotate freely about its central axis (Θ = 0° to 270°) with the patient table in place. Allowed transducer motions include: linear (δ =0 to 4.5 cm) along the slot guide toward and away from the central axis of the cylinder; tilt (Φ = 0° to 35°) from horizontal in the plane perpendicular to the MR table; and rotation (α = -15° to 15°) in the horizontal plane of the transducer. These degrees of freedom have gauge markings on the device to display the transducer orientation and aid in positioning the

focus at the desired MR coordinates. When combined with electronic steering, the system provides a large treatable volume (0.9 L) within the breast (25).

The three tracker coils were made by tightly wrapping insulated 27 AWG wire four times around a benzonatate (100 mg) spherical capsule that was 6.75 mm in diameter. The wires were bonded to the capsule with epoxy and soldered to a custom printed circuit board measuring 21 x 29 x 1 mm (Figure 6.1d). The unit was rigidly attached to the circuit board with epoxy with the coil axis approximately 15° from vertical to maintain coil signal sensitivity for any Φ rotation of the transducer. The circuit board was printed with a large ground plane on both sides with connection vias to reduce the stray inductance of the circuit. The tuning capacitance for the 1H resonant frequency was achieved by placing capacitors in parallel and in series (Figure 6.1d). Surface mount capacitors were used instead of variable capacitors to ensure capacitance stability over time. A diode and chip RF choke were inserted into the circuit to provide active detuning of the resonant circuit during RF transmission. The coils were connected to Siemens preamps with varying lengths of RG316 coax cable. Preamp decoupling values for the three tracker coils were -22.1, -24.2 and -23.4 dB. The circuit boards were rigidly attached to the posterior transducer support structure of the breast MRgFUS system forming a triangle with unique side lengths (Figure 6.1c).

6.3.2 Software

A simple one-dimensional readout sequence was used to obtain each tracker coil's approximate position within the bore (Figure 6.1e) (18). The sequence nonselectively excited the entire volume then read in one dimension (pixel spacing =

0.24 mm; field of view = 500 mm; echo time (TE)/repetition time (TR) = 4.6/9.4 ms; readout bandwidth = 250 Hz/pixel; flip angle = 15°). After applying a Hann filter, the one-dimensional data was zero-fill interpolated to 0.12 mm pixel spacing. The sequence used six excitations to perform a readout in all three orthogonal directions with both a positive and negative gradient lobe. The data was converted to image space by the scanner image calculation environment and transferred automatically (through the US control software) to a custom MATLAB (Mathworks, Natick, MA) graphical user interface (GUI) on a second computer, which performed all of the following computations. A center of mass (COM) was computed for each readout polarity using Equation [6.1]

$$COM = \frac{\sum_{i=1}^{n} v_i(\vec{r}_i) \cdot \vec{r}_i}{\sum_{i=1}^{n} v_i(\vec{r}_i)} \qquad [6.1]$$

where r_i is the position of each voxel and v_i is the associated signal value.

Only voxels whose signal magnitude exceeded 15% of the maximum were included in the COM calculations. The final tracker coil position was computed from the mean of the two COM locations for each dimension (18).

The coil positions were then corrected for gradient nonlinearity, also referred to as gradient warp, using the method described by Janke et al. (27). The spherical harmonic coefficients necessary for the correction were provided by Siemens Medical Solutions, Erlangen, Germany. After obtaining the position of each coil, the six degrees of freedom transformation (28) that aligned the calibrated coil locations to the current locations was calculated using MATLAB's *procrustes* function. This transform was then applied to the calibrated focus location to estimate the current focal location. The MATLAB GUI displayed the current focal location, current coil positions and the

raw signal plots from each coil. The computation time within the GUI was approximately 150 ms. This prediction method requires calibration of the tracker coil positions with respect to the focus location. (The calibration is described below in the "Accuracy Verification" section.)

6.3.3 Tracker Coil Signal

An experiment was performed to assess the performance of the tracker coil signal as a function of distance from isocenter. The worst-case scenario for signal performance was chosen where the MRgFUS system was placed in the scanner with the transducer's beam propagating in the head-foot (HF) direction, as this alignment of the tracker coils with the B0 field has the highest sensitivity to Φ rotations (Figure 1b). The center tracker coil (coil #2, Figure 6.1c) on the transducer housing was placed at isocenter, and the MR patient table was moved in 1 cm increments out to 20 cm away from isocenter while collecting tracker location data at each table position. This was repeated for four Φ rotations (0°, 10°, 20°, and 30°). The magnitude of the gradient warp correction distance of the tracker coils was also calculated for these data. The focus was predicted at each HF position, both with and without using gradient warp correction, using the same calibrated coil positions and focus obtained from a separate experiment as described in the "Accuracy Verification" section.

6.3.4 Accuracy Verification

A breast shaped gelatin phantom (29) was placed in the system and coupled to the transducer with deionized and degassed water that was doped with 1 g/L of manganese chloride (MnCL2) to decrease T_2 and suppress the water signal. The center

of the MRgFUS system tank was positioned at isocenter and the system patient table was placed above the phantom and six one liter bags of saline were placed on the table above the transducer to emulate signal from a patient. The transducer was placed in a total of 16 positions, 12 of which were unique and four of which were repeated. With the center of the MRgFUS system positioned at isocenter, the tracker coils were located approximately 16-20 cm from isocenter. This distance will vary slightly depending on which breast is treated and system rotation θ. The gelatin phantom was heated with the US transducer at the geometric focus (13 acoustic W, 31.5 s) twice for each transducer position where the 3D imaging slabs were oriented with the imaging planes parallel and perpendicular to the US propagation path (Figure 6.2). Proton resonance frequency (PRF) shift temperature measurements (30) were obtained during sonication using a three dimensional segmented echo planar imaging (seg-EPI) sequence with flyback readout (voxel dimensions = 1 x 1 x 2 mm; field of view = 224 x 154 x 16 mm; TE/TR = 19/41 ms; EPI Factor = 13; 12 slices with 25% oversampling; readout bandwidth = 1062 Hz/pixel; 13 Image repetitions; 6.3 s per image). After applying a Hann filter along the readout and phase encoding directions, images were zero-fill interpolated to 0.5 mm isotropic voxel spacing. Three baseline images were acquired before US sonication, and the average phase during the baseline images was used as the reference phase for calculating the PRF shift temperature change.

The measured focus location in both slab orientations was determined as the COM of the 3D temperature map using only the voxels that experienced at least 50% of the maximum temperature. The measured focus location for each transducer

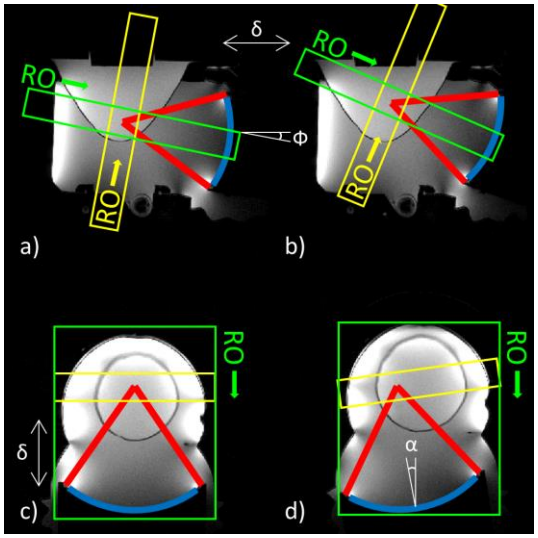

Figure 6.2. Transducer positions and imaging slabs. Green – Parallel slab. Yellow – Perpendicular slab. RO – Readout direction. a) Initial position at Φ=10°, δ=2 cm, α=0°. b) Φ=20°, δ=2 cm, α=0°. c) Φ=20°, δ=3 cm, α=0°. d) Φ=20°, δ=3 cm, α=10°. Red lines show approximate ultrasound beam propagation. Curved blue line outlines the transducer face. All experiment locations used one of these four positions with the system rotation Θ at 0°, 40° or 90°. See Figure 6.1b for definitions of Θ, δ, α, and Φ.

position was defined as the average of the locations determined from the parallel and perpendicular imaging slabs. The temperature COM at the first transducer position (Figure 6.2a with Θ=0°, δ=2cm, Φ=10°, α=0°) was used to calibrate the location of the focus with respect to the three tracker coils. Because the calibration between the tracker coils and the focus was not yet known, the 3D imaging slabs were aligned manually for the first location by estimating the focal position from measurements drawn on localizer images to ensure the focus was captured in the images. After the calibration from the first location was determined, predictions from the tracker coils were used to position the center of the slab at the predicted focus location for the remaining transducer positions. The slab orientation (rotation) was aligned parallel or perpendicular to the US propagation path with knowledge of the rotation, θ, of the

system and the rotations (Φ, and α) of the transducer. The distance between the measured and tracker coil predicted focus locations was determined for each transducer position.

The variability of the measured temperature COM position was measured by repeating the heating at the first transducer position six times (three parallel slabs and three perpendicular slabs) while allowing sufficient time for the gelatin to cool between repetitions. The tracking sequence was repeated 10 times at the first transducer position to assess the variability of tracker coil position estimates. The focal position was predicted from each of these 10 repetitions.

6.4 Results

Figure 6.3a shows the typical signal from a tracker coil for all six readouts. The dashed line shows the cutoff set at 15% of the maximum value. Signal from the saline bags, which is well below the 15% cutoff, can be seen in the Y direction. The measured coil position is defined to be halfway between the peaks from positive and negative readouts. The typical relative signal-to-noise ratio (SNR) of these coils with the tracking sequence was approximately 1000. Figure 6.3b shows the tracker signal as a function of HF distance from isocenter and Φ rotation. The signal change with Φ rotation depends on the component of the coil's area that is perpendicular to the MRI scanner's main magnetic field. The kink in the plot is possibly due to the profile of the B1 transmit field and the related bandwidth of the excitation pulse, though this has not been explored. Figure 6.3c shows the gradient warp correction distance as a function of HF distance from isocenter for a tracker coil on the magnet's x=0 (left-right) axis. Figures 6.3d-e show how the predicted focus moved with and without gradient warp

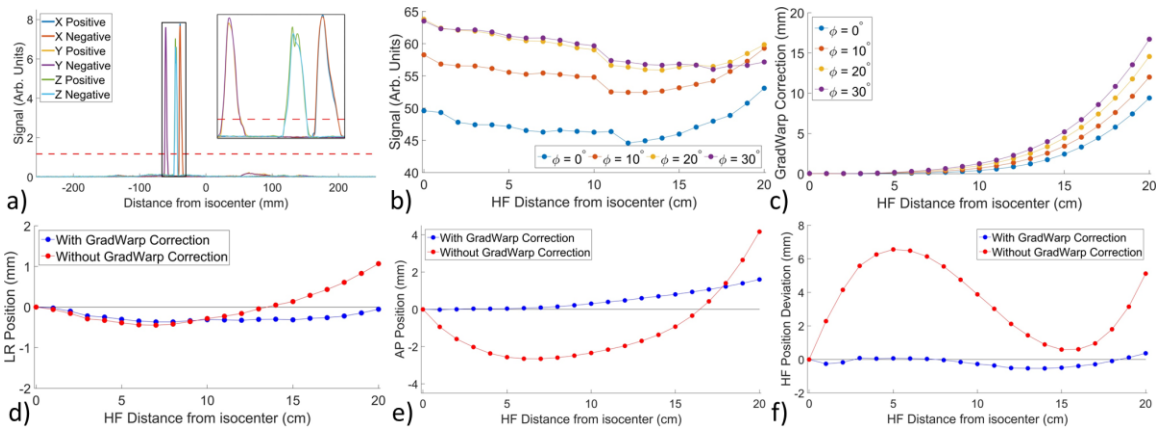

Figure 6.3. a) Example tracker signal from a single coil for all 6 readout directions with inset showing zoomed in profiles. b) Tracker signal vs. head-foot distance from isocenter for four Φ rotations for tracker coil #2. c) Gradient warp correction distance as a function of head-foot distance from isocenter for four Φ rotations for tracker coil #2. d-e) Predicted focus movement relative to the first predicted location with and without gradient warp correction for the LR axis (d) and AP axis (e). f) Deviation from expected difference relative to the first predicted focus location with and without gradient warp correction for the HF axis.

correction compared to the first predicted location for the left-right and anterior-posterior axes for Φ=30°. The predicted focus should show no motion along these axes, as the only change between these points was the table moving in the HF direction. Figure 6.3f shows the deviation from expected difference in the predicted focus position relative to the first predicted location along the HF axis for Φ=30°.

Temperature measurements as a function of time for the six repeatability sonications were nearly identical within the parallel (3.1% variation) and perpendicular (2.0% variation) cases. The parallel slab orientation measured a slightly higher temperature than the perpendicular slab, most likely due to partial volume effects (15). For the parallel slab repeatability tests, the temperature center of mass moved an average distance of 0.15 mm between repetitions, and for the perpendicular slabs it was 0.14 mm. The average distance of the temperature center of mass between

the parallel and perpendicular imaging slabs was 2.1±0.1 mm in the repeatability tests, and for all 16 locations it was 1.6±0.5 mm.

The tracker coil predicted focus was an average distance of 2.1±1.1 mm from the locations determined from the PRF temperature data. Without gradient warp correction, the predicted focus was an average distance of 6.5±3.9 mm from the PRF temperature focus. The error in predicted focus location displayed some bias. The average error in the y axis prediction was approximately 1.4 mm above (patient posterior) the actual focus. The average error in the x-z plane was approximately 1.1 mm toward the transducer. For the 10-run tracker coil repeatability tests, the measured center of mass positions moved an average distance of 9 micrometers, and the position of the predicted focus varied by an average distance of 19 micrometers between runs.

Figure 6.4 shows the PRF temperature change at the US focus and predicted focus location overlaid on the zoomed in magnitude images for all three orthogonal planes going through the temperature center of mass for all 16 transducer positions of the parallel imaging case.

6.5 Discussion

The results in this paper demonstrate that, using tracking coils without sonication, the geometric focus of the US transducer in this specific noncommercial MRgFUS system inside a Siemens TIM Trio 3T MRI scanner can be accurately predicted to within approximately 2.1 mm. The calibration between the tracker coils and focus locations only needs to be performed once for the system. The tracking sequence and prediction calculations are rapid, requiring less than 1 s to measure and report the predicted focus in MR coordinates. Such rapid localization might also be

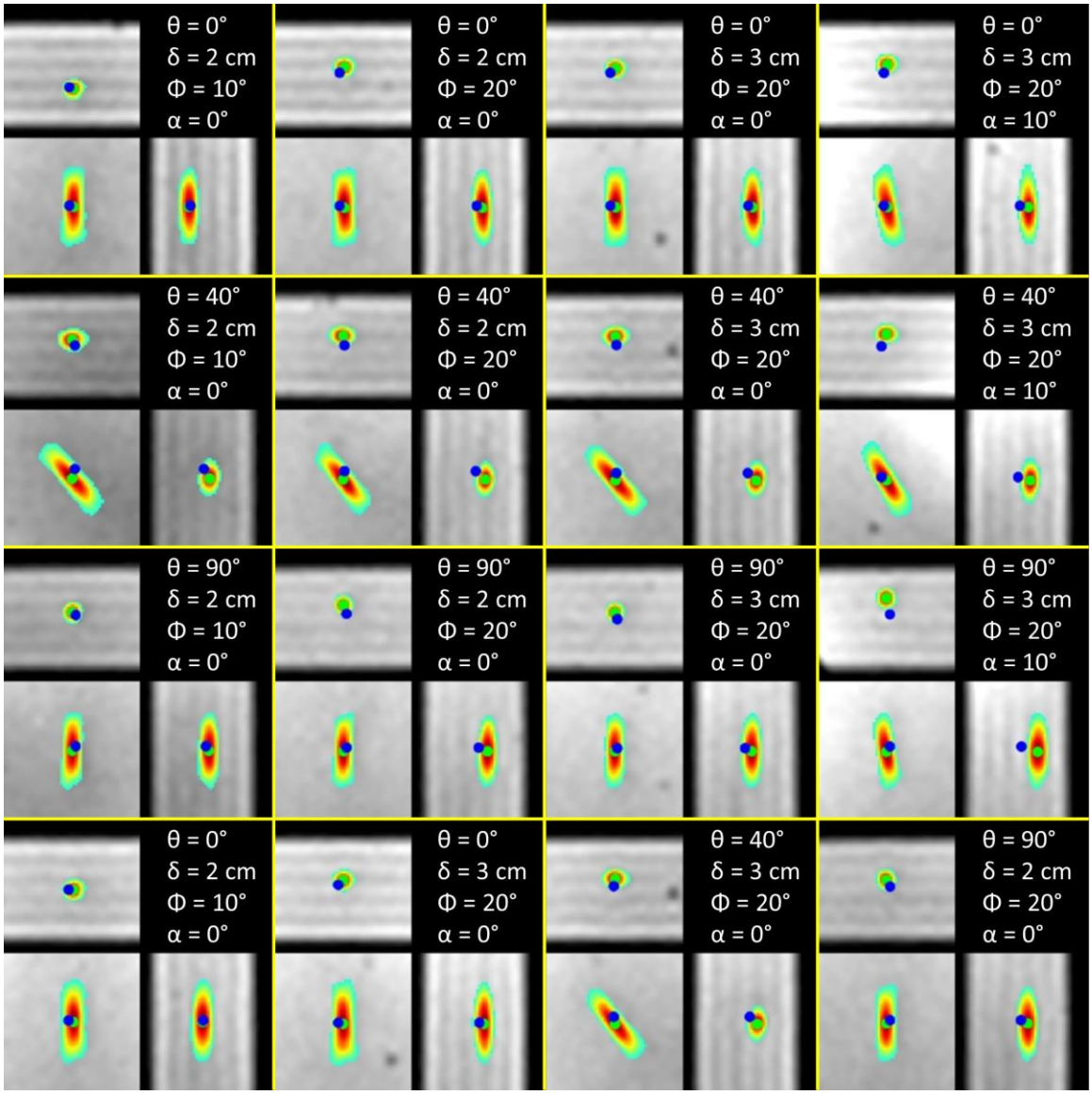

Figure 6.4. PRF temperature at the focus overlaid on magnitude images for the three orthogonal planes through the temperature center of mass for all 16 transducer positions of the parallel slab imaging case. The calculated temperature center of mass location is shown by a green marker and the predicted focus location from the tracker coils is shown by a blue marker.

applicable to a hand-held or manually positioned FUS transducer. Although this rapid position determination is very useful to FUS therapy, the need for low-power test sonications may still be necessary to ensure proper acoustic coupling of the patient as well as other safety and efficacy concerns. However, the tracker coils will minimize the time necessary for focal point determination. Gradient warp correction proved to be necessary to accurately locate the coils. This is due to their relatively large distance from isocenter (~16-20 cm) for most transducer positions.

Indeed, imperfect gradient warp correction is most likely the largest source of error between the predicted and actual focus location. Gradient warp correction uses a limited number of correction coefficients, and requires accurate measurements of the spherical harmonic coefficients. Figures 6.3e-f show the effects of imperfect gradient warp correction on the predicted focus. Although significantly improved after gradient warp correction, more correction coefficients could possibly further improve the accuracy of the tracker coil predicted focus. Tracker coils implemented on US systems with shorter focal lengths may have less gradient warp error, as they would likely be closer to isocenter during treatment. The tracker coils' effective range is limited to the size of the magnet's spherical volume of uniform field around isocenter and the usable range of the gradients, which will vary between scanner models.

The *procrustes* algorithm used in MATLAB calculates a shape preserving Euclidean transformation. By making the triangle shape formed by the three tracker coils rigid and unique (ie, not isosceles or equilateral), this ensures that the correct transducer translation and, more specifically, rotation is calculated. The exact placement of the trackers on the transducer housing is not necessarily important as

long as the triangle sides are unique and they move rigidly with the transducer. Although MATLAB offers a convenient prototyping environment, future development plans include performing all calculations within the US control software, removing the need to export to MATLAB.

Tuning and matching of the coils provided high SNR, allowing the coils to be used anywhere within the magnet's uniform volume. The high SNR also makes the position determination highly repeatable. It should be noted, however, that proper decoupling of the tracker coils during image acquisition is necessary to prevent artifacts in normal imaging sequences. When active/passive or preamp decoupling fails, the tracker coils can produce artifacts in imaging sequences even when the coil is not within the excited volume or imaging field of view. Quality assurance scans with phantoms, which are already in the treatment protocol before each patient is treated, will ensure the tracker/imaging coils are in proper working order.

The repeatability of heating with FUS in the gelatin phantom was demonstrated. The predicted focus location does not take into account any US propagation effects such as refraction, beam aberration, or attenuation. For each transducer position, the US beam propagated through different distances in the phantom. These different propagation lengths would attenuate the focus slightly, helping explain the discrepancy between the heated and predicted focal location since the predicted location is dependent on geometry only. This shift is likely much smaller than the error from imperfect gradient warp correction due to the homogenous nature of the phantom. Finally, it is possible that beam aberration distortions may be greater in breasts with highly heterogeneous distributions of fat and glandular tissue (29).

In conclusion, this study demonstrates that the positions of three tracker coils rigidly attached to the transducer housing can be used to quickly and accurately predict the location of the US transducer geometric focus without the need to sonicate. Rapid prediction of the focus based on this method will shorten total treatment time by allowing faster focal spot determination. This will improve patient safety and potentially reduced treatment times by removing the need to sonicate in order to locate the focus.

6.6 Acknowledgments

We thank Alexis Farrer for preparing the gelatin phantom.

6.7 References

1. Furusawa H, Namba K, Thomsen S, Akiyama F, Bendet A, Tanaka C, Yasuda Y, Nakahara H. Magnetic resonance-guided focused ultrasound surgery of breast cancer: reliability and effectiveness. J Am Coll Surg 2006;203(1):54-63.

2. Kim YS, Bae DS, Kim BG, Lee JW, Kim TJ. A faster nonsurgical solution very large fibroid tumors yielded to a new ablation strategy. Am J Obstet Gynecol 2011;205(3):292 e291-295.

3. Sommer G, Bouley D, Gill H, Daniel B, Pauly KB, Diederich C. Focal ablation of prostate cancer: four roles for magnetic resonance imaging guidance. Can J Urol 2013;20(2):6672-6681.

4. Frenkel V, Etherington A, Greene M, Quijano J, Xie J, Hunter F, Dromi S, Li KC. Delivery of liposomal doxorubicin (Doxil) in a breast cancer tumor model: investigation of potential enhancement by pulsed-high intensity focused ultrasound exposure. Acad Radiol 2006;13(4):469-479.

5. Kneidl B, Peller M, Winter G, Lindner LH, Hossann M. Thermosensitive liposomal drug delivery systems: state of the art review. Int J Nanomedicine 2014;9:4387-4398.

6. Rapoport N, Nam KH, Gupta R, Gao Z, Mohan P, Payne A, Todd N, Liu X, Kim T, Shea J, Scaife C, Parker DL, Jeong EK, Kennedy AM. Ultrasound-

mediated tumor imaging and nanotherapy using drug loaded, block copolymer stabilized perfluorocarbon nanoemulsions. J Control Release 2011;153(1):4-15.

7. Elias WJ, Huss D, Voss T, Loomba J, Khaled M, Zadicario E, Frysinger RC, Sperling SA, Wylie S, Monteith SJ, Druzgal J, Shah BB, Harrison M, Wintermark M. A pilot study of focused ultrasound thalamotomy for essential tremor. N Engl J Med 2013;369(7):640-648.

8. Suffredini G, Levy LM. MR-guided, focused ultrasound: applications to essential tremor and other neurologic conditions. AJNR Am J Neuroradiol 2014;35(5):829-831.

9. Ellens NP, Kobelevskiy I, Chau A, Waspe AC, Staruch RM, Chopra R, Hynynen K. The targeting accuracy of a preclinical MRI-guided focused ultrasound system. Med Phys 2015;42(1):430-439.

10. Hynynen K, Freund WR, Cline HE, Chung AH, Watkins RD, Vetro JP, Jolesz FA. A clinical, noninvasive, MR imaging-monitored ultrasound surgery method. Radiographics 1996;16(1):185-195.

11. Holbrook AB, Ghanouni P, Santos JM, Medan Y, Butts Pauly K. In vivo MR acoustic radiation force imaging in the porcine liver. Med Phys 2011;38(9):5081-5089.

12. Kaye EA, Chen J, Pauly KB. Rapid MR-ARFI method for focal spot localization during focused ultrasound therapy. Magn Reson Med 2011;65(3):738-743.

13. McDannold N, Maier SE. Magnetic resonance acoustic radiation force imaging. Med Phys 2008;35(8):3748-3758.

14. de Bever JT, Odeen H, Todd N, Farrer AI, Parker DL. Evaluation of a three-dimensional MR acoustic radiation force imaging pulse sequence using a novel unbalanced bipolar motion encoding gradient. Magn Reson Med 2015:n/a-n/a.

15. Todd N, Vyas U, de Bever J, Payne A, Parker DL. The effects of spatial sampling choices on MR temperature measurements. Magn Reson Med 2011;65(2):515-521.

16. Hinkelman LM, Liu DL, Waag RC, Zhu Q, Steinberg BD. Measurement and correction of ultrasonic pulse distortion produced by the human breast. J Acoust Soc Am 1995;97(3):1958-1969.

17. Mougenot C, Tillander M, Koskela J, Kohler MO, Moonen C, Ries M. High intensity focused ultrasound with large aperture transducers: a MRI based focal

point correction for tissue heterogeneity. Med Phys 2012;39(4):1936-1945.

18. Dumoulin CL, Souza SP, Darrow RD. Real-time position monitoring of invasive devices using magnetic resonance. Magn Reson Med 1993;29(3):411-415.

19. Wacker FK, Elgort D, Hillenbrand CM, Duerk JL, Lewin JS. The catheter-driven MRI scanner: a new approach to intravascular catheter tracking and imaging-parameter adjustment for interventional MRI. AJR Am J Roentgenol 2004;183(2):391-395.

20. Ooi MB, Aksoy M, Maclaren J, Watkins RD, Bammer R. Prospective motion correction using inductively coupled wireless RF coils. Magn Reson Med 2013;70(3):639-647.

21. Watkins R, Piel J, Rowling K, Dumoulin C. A Handheld Device for MR-Guided Focused Ultrasound Ablation of the Prostate. In Proceedings of the 13th Annual Meeting of ISMRM, Honolulu, Hawaii, USA, 2002. p. 2223.

22. Salgaonkar VA, Prakash P, Plata J, Holbrook A, Rieke V, Kurhanewicz J, Hsu IC, Diederich CJ. Targeted hyperthermia in prostate with an MR-guided endorectal ultrasound phased array: patient specific modeling and preliminary experiments. Proc SPIE 2013;8584: doi:10.1117/1112.2004609.

23. Piel JE, Giaquinto RO, Watkins RD, Gross P, Guhde R, Darrow RD, Bishop P, Ari N, Ari X, Topka TM, Dumoulin CL. A Trans-Rectal Focused Ultrasound Probe for MR-Guided Ablation of the Prostate. In Proceedings of the 13th Annual Meeting of ISMRM, Miami Beach, Florida, USA 2005. p. 152.

24. Minalga E, Payne A, Merrill R, Todd N, Vijayakumar S, Kholmovski E, Parker DL, Hadley JR. An 11-channel radio frequency phased array coil for magnetic resonance guided high-intensity focused ultrasound of the breast. Magn Reson Med 2013;69(1):295-302.

25. Payne A, Merrill R, Minalga E, Vyas U, de Bever J, Todd N, Hadley R, Dumont E, Neumayer L, Christensen D, Roemer R, Parker D. Design and characterization of a laterally mounted phased-array transducer breast-specific MRgHIFU device with integrated 11-channel receiver array. Med Phys 2012;39(3):1552-1560.

26. Payne A, Todd N, Minalga E, Wang Y, Diakite M, Hadley R, Merrill R, Factor R, Neumayer L, Parker DL. In vivo evaluation of a breast-specific magnetic resonance guided focused ultrasound system in a goat udder model. Med Phys 2013;40(7):073302.

27. Janke A, Zhao H, Cowin GJ, Galloway GJ, Doddrell DM. Use of spherical

harmonic deconvolution methods to compensate for nonlinear gradient effects on MRI images. Magn Reson Med 2004;52(1):115-122.

28. Lavit C, Escoufier Y, Sabatier R, Traissac P. The ACT (STATIS method). Computational Statistics & Data Analysis 1994;18(1):97-119.

29. Farrer AI, Odeen H, de Bever J, Coats B, Parker DL, Payne A, Christensen DA. Characterization and evaluation of tissue-mimicking gelatin phantoms for use with MRgFUS. J Ther Ultrasound 2015;3:9.

30. Ishihara Y, Calderon A, Watanabe H, Okamoto K, Suzuki Y, Kuroda K, Suzuki Y. A precise and fast temperature mapping using water proton chemical shift. Magn Reson Med 1995;34(6):814-823.

CHAPTER 7

MULTI-ECHO PSEUDO-GOLDEN ANGLE STACK OF STARS THERMOMETRY WITH HIGH SPATIAL AND TEMPORAL RESOLUTION USING K-SPACE WEIGHTED IMAGE CONTRAST

This chapter is based on a paper titled, "Multi-Echo Pseudo-Golden Angle Stack of Stars Thermometry with High Spatial and Temporal Resolution Using k-Space Weighted Image Contrast", authored by Bryant T. Svedin, Allison Payne, Bradley D. Bolster Jr. and Dennis L. Parker, which was submitted to the journal Magnetic Resonance in Medicine for review in January 2017 and resubmitted after review in March 2017.

7.1 Introduction

Magnetic resonance (MR) imaging provides excellent soft tissue contrast and when used to guide focused ultrasound (FUS), provides the ability to localize, plan, monitor and verify treatments (1). FUS has been used to noninvasively treat uterine fibroids as well as breast, prostate, liver, and brain cancer (2-5). As FUS can locally heat tissue very quickly, at rates greater than 1 °C/s, the monitoring of treatments (6,7) requires a high spatial and temporal resolution. Also, because the energy is delivered from a large transducer aperture to a small focus, a large field of view is required to

monitor any possible energy deposition away from the focus. The FUS beam will likely travel through several different tissue types during treatment where a portion of the beam will be reflected and transmitted at each tissue interface depending on the impedance difference between the tissues. Each tissue type will also absorb a different amount of the ultrasound energy. For example, 90% of the ultrasound energy through the skull is reflected or absorbed (8).

Monitoring of interventional treatments can be done using 2D or 3D MRI sequences where the method chosen is often governed by the trade-off between the needed temporal and spatial resolution and required field of view. Currently, clinical monitoring of MR guided FUS (MRgFUS) treatments is limited to a single (or relatively few) 2D slices (2,3,9-13) providing a limited field of view. For example, 2D monitoring of the ultrasound focus during transcranial MRgFUS treatments is severely limited and can miss heating outside of the slices monitored, such as near the skull surface, in grating lobes or in any points of unintended energy deposition due to beam aberration (14).

MR temperature imaging does have some limitations, which are more apparent when using 2D imaging such as partial volume effects, which cause temperature underestimation (15). These effects can be reduced using smaller voxels and band-limited (sinc) interpolation (15), but these options are not readily available in 2D MRI which has slices that are thicker and interpolation cannot be used in the through slice direction. Further, it can also be difficult to properly position a single 2D slice to capture the entire focus and to limit slice crosstalk, multiple 2D slices often have a gap between each slice where any temperature changes will not be measured. Respiration

and motion artifacts will also introduce errors to the temperature monitoring.

3D MR thermometry can overcome many of the field of view, partial volume, and coverage gap limitations, which are inherent in 2D imaging but unfortunately, standard 3D sequences typically require too much time to acquire k-space to be clinically viable. Temporal resolution can be increased by methods involving undersampling such as temporally constrained reconstruction (16), model predictive filtering (17), Kalman filtering (18), parallel imaging (19) or using a sequence designed for increased speed such as segmented echo-planar imaging (seg-EPI) (20,21).

While a 3D seg-EPI offers several advantages, it has limitations. The chemical shift artifact, field inhomogeneity, and field variation due to motion artifacts are increased due to the low bandwidth in the phase encoding direction. The chemical shift typically requires imaging with fat saturation, while the respiration artifact can be corrected to a limited extent depending on the orientation of the 3D slab (22). Increasing the EPI factor, or number of lines collected per TR, will increase the temporal resolution while further escalating the chemical shift and respiration artifacts and decreasing the signal to noise ratio (SNR). Seg-EPI sequences also typically have image distortions along the phase encode direction.

Non-Cartesian 3D sequences, such as stack of stars and stack of spirals (23), have several advantages that have been explored for use in thermometry. Projection sampling performs well with high levels of undersampling. The center of k-space is sampled every TR providing robustness to motion, as well as the ability to correct respiration artifacts through self navigation (24). Projection sampling can take advantage of the oversampled central region of k-space to artificially increase the

temporal resolution while maintaining the high spatial resolution by using k-space weighted image contrast (KWIC) (25,26). Using a golden angle (GA) increment improves the ability for angular undersampling, as a GA increment guarantees an optimal projection angle distribution for an arbitrary number of projection angles, and the irrational nature of the GA also lends itself to compressed sensing (27). It has been shown that the GA is also an optimal radial projection order when using KWIC (28), as it allows for arbitrary temporal resolution and temporal update rate. Combining radial sampling with Cartesian slice encoding in stack of stars (SOS) sequences allows for 3D imaging with these advantages (29). The temporal resolution can be further increased by taking advantage of partial Fourier sampling in the slice direction (30).

While the implementation of non-Cartesian sampling trajectories have historically had some difficulties, these issues have been largely overcome. Off-resonance artifacts produce blurring instead of unidirecitonal shift, but a more uniform field and increased readout bandwidth can help decrease the blur (29). Errors in the gradient timing can produce significant artifacts, but several correction methods have been successfully implemented (29,31-33). Finally, efficient algorithms and computer hardware can significantly reduce the computation time required to grid the non-Cartesian measurements onto a Cartesian grid (34,35).

Many regions of the body have significant amounts of adipose tissue near where interventional treatments are performed (e.g., breast, uterus), which can affect image quality. The strength of the chemical shift artifact and SNR are both related to the readout bandwidth. As the readout bandwidth is decreased, the SNR and chemical shift artifact will both increase. A simple method to maintain SNR while decreasing

the chemical shift artifact is to increase the readout bandwidth and acquire multiple echoes (36,37). The individual echoes will have lower SNR; however, data from each echo can be combined to increase the overall SNR of both the magnitude and phase information (38-40). Acquiring multiple echoes has the added benefit of allowing calculation of T2* and the initial signal magnitude, M(0), as well as separate water/fat images. T2 has been shown to have a linear relationship with temperature in adipose tissue and has been used as a measure of temperature to monitor near field heating (40,41). The signal magnitude also varies with the equilibrium magnetization and T1, both of which change with temperature (6,42).

In this work, we present and evaluate a new 3D multiecho SOS sequence for use in MRI thermometry with pseudo golden angle (PGA) sampling and KWIC temporal weighting to simultaneously provide multiple quantitative measurements (proton resonance frequency (PRF) shift temperature, M(0), and T2*). Unlike the GA increment, which never repeats, the PGA has the advantage that the projection angle repeats after a fixed number of increments, allowing a trajectory matching baseline subtraction for improved temperature measurement accuracy. We demonstrate that 3D multiecho SOS with PGA simultaneously provides high spatial and temporal resolution measurements, measures and corrects respiration artifacts through self-navigation, and provides water/fat separation. The KWIC reconstruction algorithm and quantitative measurements are described in detail. Four possible methods of phase determination and baseline subtraction for calculating PRF temperature change from multi-echo PGA SOS image volumes are presented. The precision of each quantitative measurement from the sequence and KWIC reconstruction method were tested in

breasts during a nonheating situation. The sequence and KWIC reconstruction were also applied during MRgFUS heating in aqueous and adipose ex vivo pork tissue.

7.2 Methods

7.2.1 Sequence and Data Acquisition

A 3D multi-echo stack of stars spoiled gradient echo sequence was modified such that the angle increment between projections was the PGA, $\theta = (1 - 233/377) * 360° \approx 137.56°$. The PGA is based on the ratio of two Fibonacci numbers and will cause the k-space trajectory to repeat exactly after 377 projections. For each excitation, all echoes were acquired at the same projection angle, and were acquired with a bipolar gradient readout. This was repeated for all kz phase encodings were acquired at the same projection angle before incrementing by the PGA. Sampling the center of k-space with each TR (Figure 7.1a) allowed for self-navigated respiration correction as described in Section 7.2.3.

7.2.2 Image Reconstruction

The KWIC algorithm with a sliding KWIC reconstruction window was implemented to generate images with an effectively high temporal resolution (25,26) with the PGA sampling pattern. The PGA projection increment guarantees a nearly uniform distribution of projection angles for any arbitrary number of projections. By using a sliding window an arbitrary number of time points with arbitrary temporal resolution can be reconstructed. The optimal KWIC reconstruction window used with GA is described by Winkelmann (28), where the radial aliasing difference between uniformly distributed radial projections and GA sampling is minimized when the

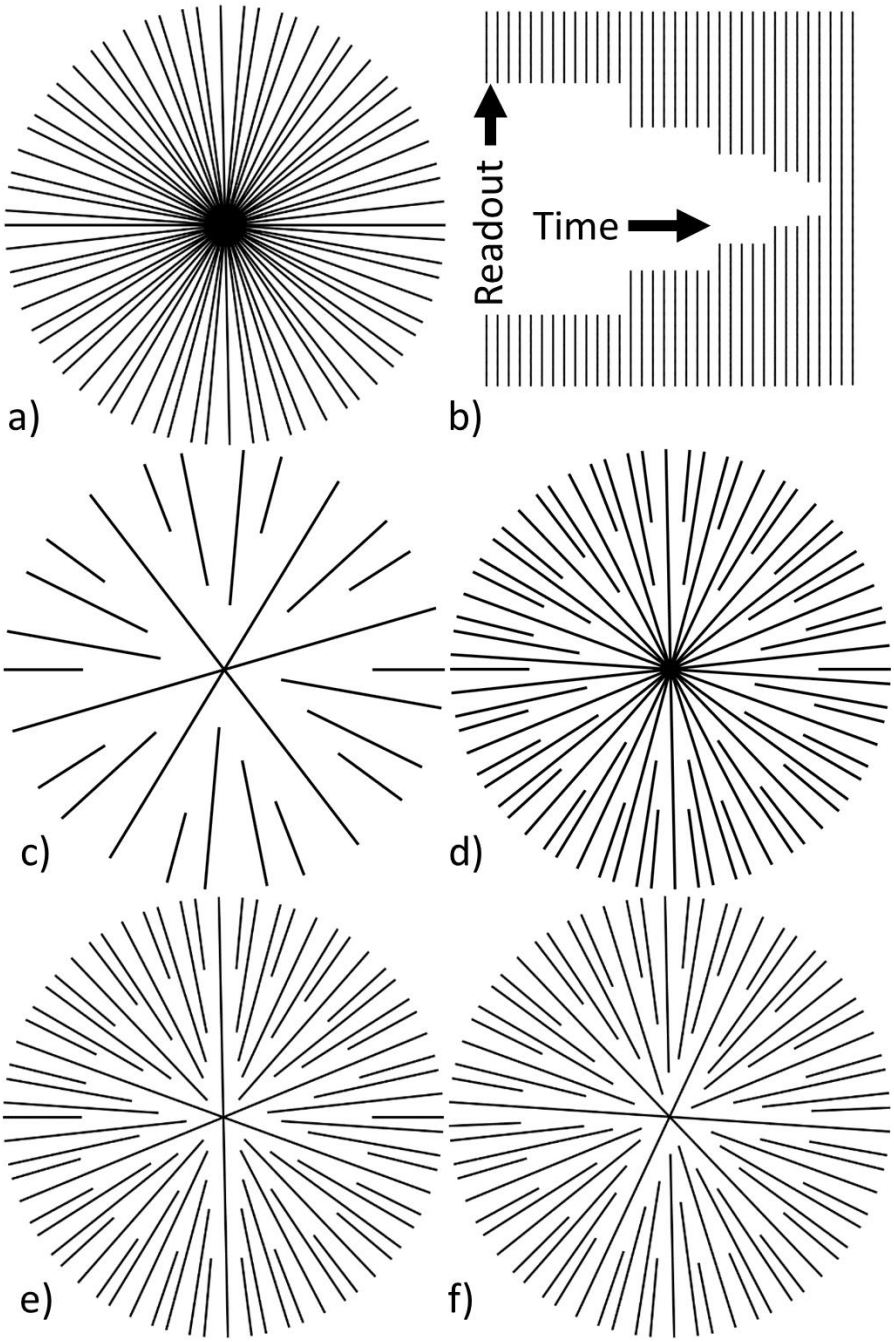

Figure 7.1. a) Example of fully sampled pseudo-golden angle (PGA) k-space with 34 projections. b) Asymmetric KWIC window with 3 center and 34 outermost projections. c) Example of k-space sampling using KWIC with 3 center and 13 outermost projections. d) Example of k-space sampling using KWIC with 8 center and 34 outermost projections. e) Example of k-space sampling using KWIC with 3 center and 34 outermost projections at the first reconstructed time point. f) Example of k-space sampling using KWIC with 3 center and 34 outermost projections at the second reconstructed time point.

number of acquired projections is equal to a Fibonacci number. The effective temporal resolution of images reconstructed using the KWIC algorithm is the time covered by the center of k-space. KWIC reconstructed images maintain the high spatial resolution data from the outer portions of k-space. The overall signal contrast and relatively low resolution of the FUS heating are contained in the central region of k-space and are updated much more frequently than the high frequency region which changes more slowly.

The properties of the sampling pattern and the KWIC reconstruction window used in this work depended on the number of projection included through the center and outermost rings as demonstrated in Figure 7.1 where several examples are shown. The window was asymmetric in time, placing the center of k-space at the end of the temporal window (example Figure 7.1b), thereby ensuring that the majority of the image information comes from the most recently acquired data. The number of KWIC rings and the radius of each ring depends on the total number of lines included and the number of lines through the center as described below. The angular spacing within each ring depends on the total number of projections included in the window. Including fewer projections will not only increase the overall temporal resolution, but will increase the angular spacing of projections within each ring (example Figure 7.1c). Thus, there is a tradeoff between the temporal resolution and undersampling artifacts. Increasing the number of projections through the center simply increases the radius of the innermost ring (example Figure 7.1d). The required total number of projections and number of projections through the center to accurately reconstruct the image will change with the necessary image FOV, and spatial and temporal resolution to

accurately represent the temperature change.

The KWIC window used to reconstruct nearly all KWIC images in this work had 13 projections in the center and each successive ring used the next higher Fibonacci number of projections up to 377 in the outermost ring. The outer radius of each ring (as a fraction of the total radius) was determined by the ratio of the number of projections in the ring and the number in the outermost ring: (13, 21, 34, 55, 89, 144, 233, 377)/377 = (0.035, 0.056, 0.09, 0.146, 0.236, 0.382, 0.618, 1). The sliding window was advanced 13 projections between each reconstructed time point. After the KWIC filter and density compensation were applied, the data were regridded using nufft (34) (available at http://web.eecs.umich.edu/~fessler/irt/irt). Besides density compensation, each projection was equally weighted. When using a GA or PGA projection increment with KWIC, the relative distribution of k-space points remains unchanged in subsequent time frames, but the entire distribution rotates about the center as shown in Figure 7.1e and f. This causes any artifacts from regridding to change spatially between reconstructed time points. For reference, a temporal series of time images reconstructed with various sizes of the sliding KWIC window is shown in Supporting Video S2. By incrementing with a PGA that repeats every 377 projections, and advancing the sliding window by 13 projections, the k-space distribution rotation will repeat after 29 reconstructed time frames. This allows a trajectory-matched baseline library, based on the 29 rotations of the k-space distribution, to be used in temperature difference calculations. The KWIC window was applied after respiration correction and to each echo separately. All images were reconstructed offline using MATLAB (Mathworks, Natick, Massachusetts, USA).

7.2.3 Respiration Correction

The respiration correction method used is the same as described in (22), except the phase variation is measured using self-navigation from the center of k-space instead of separate navigator readouts. The slice Fourier transform was applied before respiration correction was performed, thus each slice was corrected separately. The phase of the center of k-space as a function of TE was unwrapped using Equation [7.1]

$$\begin{aligned} \varphi_1 &= \angle p_1 \\ \varphi_n &= \angle(p_n p_{n-1}^*) + \varphi_{n-1} \end{aligned} \qquad [7.1]$$

where p_n is the complex value at the center of k-space, φ_n is the phase of the nth echo and $\angle$ is the angle operator. This unwrapping method works as long as the phase increment between echoes is less than 2π. Respiration phase offsets were measured by linearly fitting the slope of the phase at the center of k-space from the multiple echoes as a function of TE using linear regression. Each measurement coil will measure a different inherent nonzero phase slope due to spatial variation in B0 between sensitive volumes. This inherent phase slope was removed by averaging the measured slope over multiple respiratory cycles to obtain a baseline (nonvarying) slope and subtracting the baseline from each measurement for each coil independently. The first 377 projections were arbitrarily chosen for the baseline as it would cover multiple respiratory cycles. This method also measures and corrects for weighted average B0 field drift for each coil (weighted by the coil sensitivities). After removing the baseline phase, the remaining measured phase slope variation is primarily due to respiration motion. This measurement through the center of k-space assumes a spatially uniform off resonance from respiration. While this is not entirely true, as it has been shown that the B0 offset varies spatially (43), using an array of coils does provide some spatial

sensitivity to the off-resonance measurement. The phase of each echo was adjusted to remove the variation in phase due to respiration at their individual read time in the echo train as described in (22).

7.2.4 Coil Combination

Multicoil data were combined using a slightly modified version of Roemer's equation (44). The magnitude information was combined using the standard Roemer's equation (Eq. 24 in (44)), which is reproduced here in slightly different notation as Equation [7.2], where the complex image value is used instead of the complex sensitivity for each coil

$$M = \left(\sum_{j,k=1}^{Nc} p_j R_{j,k}^{-1} p_k^* \right)^{\frac{1}{2}} \qquad [7.2]$$

where M is the combined magnitude image data, p_j and p_k are the complex image data using KWIC from coils j and k, and $R_{j,k}^{-1}$ is the inverse noise covariance. This coil combination results in an optimal combination of magnitude information, though it contains no phase information. The phase information can also be optimally combined using a slightly modified version of Equation [7.2] by replacing the complex image value, p_k, with a complex phase reference. A fully sampled set of images, ${}^{f}p$, was reconstructed without a KWIC window using the first 377 projections, to minimize undersampling artifacts, to be used as a reference phase for the phase information coil combination. The complex data from the first echo for each coil was used as the reference phase for each echo and for each reconstructed time point, as this will preserve the phase evolution with TE. The phase information was combined using the

modified Roemer's equation shown in Equation [7.3],

$$\psi = \angle\left(\sum_{j,f=1}^{Nc} p_j R_{j,k}^{-1}\ {}^{f}p_{k,ref}^{*}\right) \qquad [7.3]$$

where ${}^{f}p_{k,ref}$ is the fully sampled complex reference data from coil k. By combining the phase information from each coil using a reference phase, the resulting data are a phase difference from the reference phase. The magnitude and phase information were recombined through Equation [7.4]

$$P = Me^{i\psi} \qquad [7.4]$$

The fully sampled multiple coil images were also combined to be used later for water/fat separation.

7.2.5 Thermometry Calculations

PRF temperature difference calculations were made using four different methods for comparison. The first method, referred to as single echo first baseline (SE-FB), simply calculated the PRF temperature difference using each echo's phase independently and the first KWIC reconstructed time image as the reference phase for subtraction. The second method, referred to as single echo trajectory-matched baseline (SE-TB) also calculated the difference for each echo independently, but used a trajectory-matched baseline library, where the reference phase is from the image where the k-space distribution was in the same rotation as the current image. The third method, combined echo first baseline (CE-FB), calculated the temperature change using the combined echo phase, described in the next paragraph, and used the first reconstructed time image as the reference phase, and the fourth method, combined echo trajectory-matched baseline (CE-TB), used the combined echo phase and a

trajectory-matched baseline library determined by the rotation of the k-space distribution. The PRF temperature change, ΔT, from the reference time is defined as

$$\Delta T = \frac{\psi(T) - \psi(T_0)}{\gamma \alpha B_0 TE} \quad [7.5]$$

where $\psi(T)$ is the phase of the current image, $\psi(T_0)$ is the phase of the reference image at a known temperature, γ is the gyromagnetic ratio, α is the PRF change coefficient of -0.01 ppm/°C and B_0 is the magnetic field strength (6).

The phase data from each echo was combined to improve temperature precision using a weighted linear least squares fit of the phase as a function of echo time as shown in Equation [7.6],

$$X^2 = \sum_j \frac{\left(\psi(x, TE_j) - (a + bTE_j)\right)^2}{\sigma^2\left(\psi(x, TE_j)\right)} \qquad a = \psi_0(x) \qquad b = \beta(x) \quad [7.6]$$

where $\psi_0(x)$ is the initial phase of pixel x at TE=0ms, $\beta(x)$ is the slope of the phase change, $\psi(x, TE_j)$ is the measured phase of the xth pixel at the jth TE, and $\sigma^2\left(\psi(x, TE_j)\right)$ is the variance of the phase at each pixel x for the jth TE. The variance of the phase is proportional to one over the magnitude squared,

$$\sigma^2\left(\psi(x, TE_j)\right) \propto \frac{1}{M(x, TE_j)^2} \quad [7.7]$$

making the combined phase simply weighted by the magnitude squared.

$$X^2 = \sum_j M(x, TE_j)^2 \left(\psi(x, TE_j) - (a + bTE_j)\right)^2 \quad [7.8]$$

The solutions for a and b in Equation [7.8] are derived in Appendix A. The phase information was unwrapped along the echo dimension using Equation [7.1] before calculating the fit. Once a and b were obtained, the optimal phase combination was

calculated for the same TE as the last acquired echo using Equation [7.19].

M(0) and T2* were also calculated from the multiple echoes. Assuming mono-exponential decay, the signal magnitude in the presence of noise has the form

$$M(x,TE_j) = \left(M(x,0)^2 e^{-2\frac{TE_j}{T_2^*}} + C(x) \right)^{\frac{1}{2}} \qquad [7.9]$$

where $M(x,TE_j)$ is the signal magnitude from the xth pixel at the jth TE and $C(x)$ represents the effective noise variance at the xth pixel. The offset value of $C(x)$ can be estimated using the magnitude values and is derived in Appendix B. The value of $C(x)$ was estimated from the solution given in Equation [7.29], and then subtracted from the square of Equation [7.9], which was then linearized to give

$$\ln\left(M(x,TE_j)^2 - C(x) \right) = \ln(M(x,0)^2) - 2\frac{TE_j}{T_2^*} \qquad [7.10]$$

A weighted linear least squares fit of the natural log of the magnitude is shown in Equation [7.11]

$$X^2 = \sum_j \frac{\left(\ln\left(M(x,TE_j)^2 - C(x) \right) - (a + bTE_j) \right)^2}{\sigma^2\left(M(x,TE_j) \right)} \qquad [7.11]$$

$$a = \ln(M(x,0)^2) \qquad b = \frac{-2}{T_2^*}$$

The variance of the magnitude is also proportional to one over the magnitude squared,

$$\sigma^2\left(M(x,TE_j) \right) \propto \frac{1}{M(x,TE_j)^2} \qquad [7.12]$$

making Equation [7.11] also weighted by the magnitude squared.

$$X^2 = \sum_j \left(M(x,TE_j)^2 - C(x) \right) \left(\ln\left(M(x,TE_j)^2 - C(x) \right) - (a + bTE_j) \right)^2 \qquad [7.13]$$

Equation [7.13] has the same form as Equation [7.8] and has the same solutions for a and b which are derived in Appendix A by replacing ψ_j with $\ln\left(M_j^2 - C\right)$ and y_j^2 with $\left(M\left(x, TE_j\right)^2 - C(x)\right)$. M(0) and T2* are obtained from a and b by

$$\widehat{M}(x,0) = e^{\frac{a}{2}} \qquad \hat{T}_2^* = -\frac{2}{b} \tag{7.14}$$

Variations in M(0) and T2* were measured as a percent change using two methods. First, as a difference from the first time frame and second, as a difference from the trajectory-matched baseline k-space distribution time frames.

7.2.6 Experiments

To demonstrate the ability of the multiecho PGA SOS sequence to measure temperature changes, two types of experiments were performed. The first evaluated the precision of temperature measurements in in vivo breast during nonheating conditions, and the second experiment evaluated the sequence during MRgFUS heating in a pork phantom. All experiments were performed in a Siemens Prisma 3T MRI scanner (Siemens Healthcare, Erlangen, Germany) using a breast-specific MRgFUS system with an integrated eight-channel RF coil and an MRI-compatible phase array transducer (256 elements, 1MHz frequency, 10 cm radius of curvature; Imasonic, Besançon, France and Image Guided Therapy, Pessac, France) (45-47). All human studies were approved by the local Institutional Review Board and were performed with informed consent.

7.2.7 In Vivo Breast Nonheating Experiments

Five healthy female volunteers (age range: 20-51 years) were recruited for non-heating experiments. Each volunteer was positioned in the breast-specific MRgFUS device. After localization, multiecho PGA SOS images were acquired in both the coronal and sagittal orientations while the volunteer was free breathing. In each orientation, images were acquired with 3 different sets of imaging parameters (different TR, number of echoes, number of slices) to assess the effectiveness of each. The first image set had the following parameters (voxel size = 1.3 mm isotropic; field of view = 208 x 208 x 20.8 mm; matrix = 160 x 160 x 16; 1000 radial projections; flip angle = 10°; TR = 20 ms; TE = $2.46 + 1.29 * n, n = 0\ to$ 10 ms; readout bandwidth = 1080 Hz/pixel; 5/8 partial Fourier in slice direction). The second set of images were acquired using the same imaging parameters except with only the first 6 echoes and TR = 11 ms. The third set of images had the same TR/TE as the second set, but acquired twice as many slices with the same isotropic resolution (field of view = 208 x 208 x 41.6 mm; matrix = 160 x 160 x 32). The first 20 radial projections from each image set were discarded to ensure the sequence was at steady state before reconstruction. Each image set created 47 reconstructed time points. The effective temporal resolution of each image set was 2.60, 1.43 and 2.86 seconds, respectively. A single set of images was reconstructed without a KWIC window using the first 377 projections to minimize undersampling artifacts for use in creating a fat/water mask. Separate water/fat images were generated from the first three echoes of the images reconstructed without the KWIC window using the three-point Dixon method (48).

Temperature difference calculations were made using the four methods as

described above in the Thermometry Calculations section. Using a mask from the separated water/fat images the standard deviation through time of temperature in each aqueous tissue voxel was calculated for each of the four methods described above for each volunteer. The average of these aqueous tissue voxel standard deviations was calculated for each method for each volunteer. The PRF precision values using the last TE of each of the four methods were compared for statistical difference using a one-way ANOVA with a p value threshold of 0.05. To determine the relative precision of each phase determination/baseline subtraction method, the voxel-wise difference between the precisions from the last TE of the SE-TB, CE-FB, CE-TB methods and the SE-FB method were compared. The average difference value was determined for each difference comparison to quantify the improvement over the SE-FB method and the same ANOVA statistical test as above was used. The effect of respiration correction was quantified by subtracting the PRF precision values calculated without correction from those with correction for each aqueous voxel using the CE-TB method. The spatial average of the standard deviation from the combined echoes was also calculated as a function of the number of echoes included in the weighted linear least squares fit. M(0) and T2* were calculated using the weighted linear least squares method described above and including only the in phase echoes to minimize errors from signal changes that are not described by the exponential decay model in Equation [7.9], such as the signal from a mixture of water and fat which would move in and out of phase. The percent change in M(0) and T2* were measured as described above. The standard deviation through time of M(0) and T2* differences were calculated for both of the difference calculations.

7.2.8 MRgFUS Phantom Experiments

The sequence was evaluated during FUS heating conditions using a pork belly sample that contained significant amounts of both fat and aqueous tissues. The phantom was positioned in the same breast-specific MRgFUS system that was used to image the volunteers. The 3D imaging volume was prescribed in a coronal orientation with the same imaging parameters as the second set of in vivo images (TR = 11, 6 echoes) and 1905 radial projections (for all sampled kz) were acquired. This resulted in 117 reconstructed time frames. The phantom was sonicated with 25 acoustic W for 40 s. The pork phantom was sonicated in two locations, one in aqueous and the other in adipose tissue. PRF temperature measurements were calculated using the four methods and M(0) and T2* differences were also calculated as described in the Thermometry Calculations section. For comparison, image sets were acquired during identical sonications using a seg-EPI sequence with the following parameters (voxel size = 1.3 mm isotropic; field of view = 208 x 145.6 x 20.8 mm; matrix = 160 x 112 x 16; flip angle = 20°; TR = 44 ms; TE = 14 ms; EPI Factor = 7; readout bandwidth = 1020 Hz/pixel; 6/8 partial Fourier in slice direction). PRF temperature measurements for the seg-EPI sequence were calculated using the first time frame as the reference.

7.3 Results

The central slice of the separate water/fat images generated from the SOS sequence are shown in Figure 7.2 for each of the volunteers in both the coronal and sagittal orientations and for the pork phantom in a coronal orientation. As expected, the amount and distribution of aqueous tissue varied between volunteers. An example of the PRF temperature precision in aqueous tissue for each of the four calculation

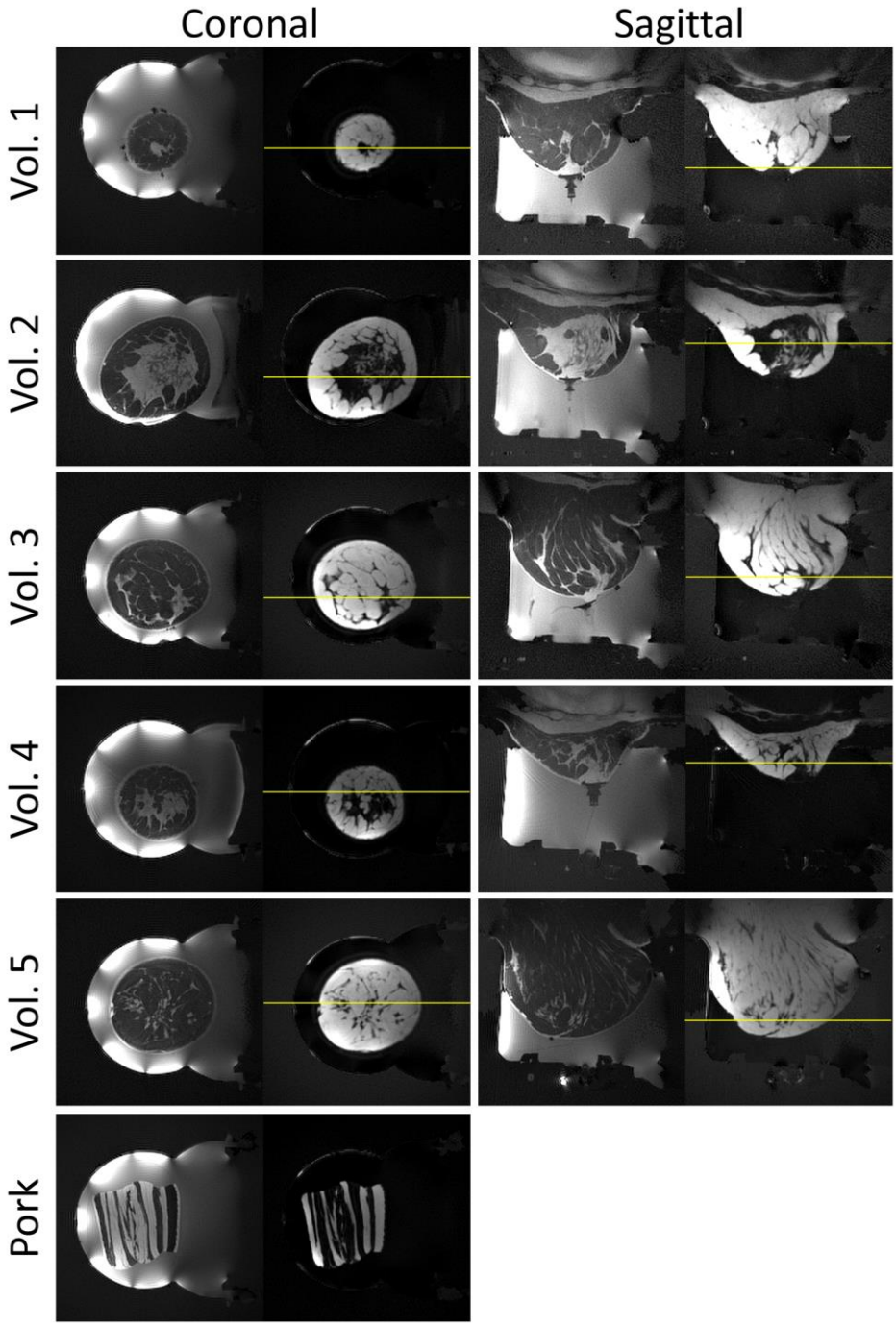

Figure 7.2. Separated water (left) and fat (right) images for in vivo breast coronal (left column) and sagittal (right column) for five volunteers and pork phantom (bottom left). Yellow line in fat images display the location of the center slice in the other orientation.

methods is shown for volunteer 2 in Figure 7.3. Figure 7.4 shows the PRF standard deviation maps for each volunteer in both orientations using the CE-TB method. Figure 7.5 shows the PRF standard deviation maps with and without respiration correction for volunteer 4 using the CE-TB method. The average improvement for each of the volunteers are comparable to the improvement observed in (22). The average improvement across the volunteers for image set 1 was 24.4±6% and 62.3±14% for the coronal and sagittal orientations respectively.

Figure 7.6 displays displays the spatially averaged PRF standard deviation for volunteer 3 as a function of TE for image set 1 in both coronal and sagittal orientation for each of the four methods. The combined echo phase data only include the echoes

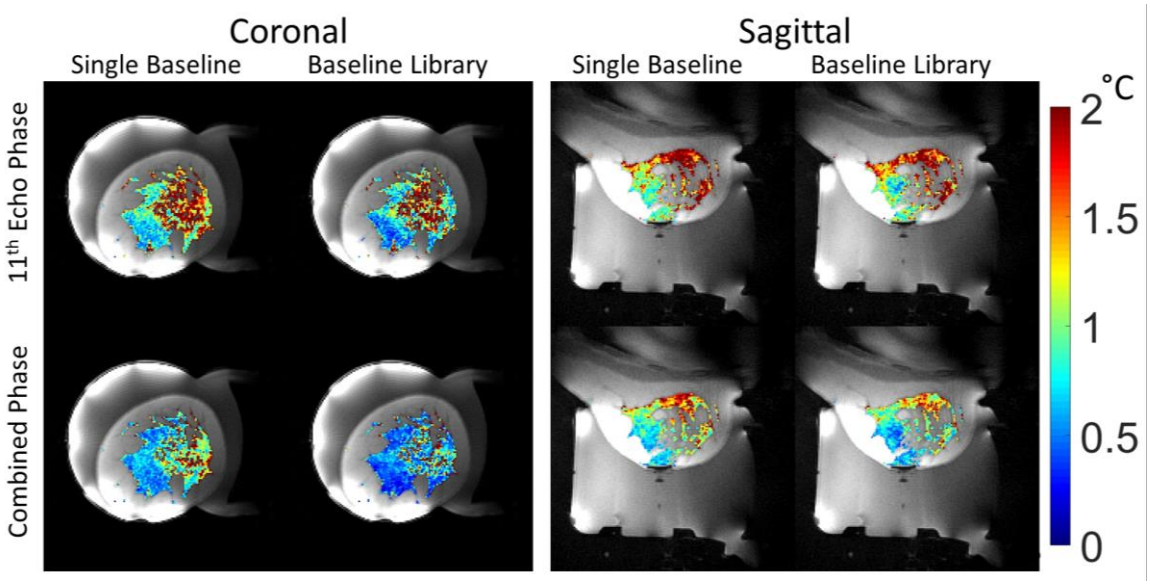

Figure 7.3. Standard deviation through time maps of PRF temperature in aqueous tissue for the four calculation methods for volunteer 2. Left column: 1st image used as phase reference. Right column: Trajectory-matched baseline images. Top Row: PRF temperature calculated from the last echo. Bottom row: PRF temperature calculated from the combined phase.

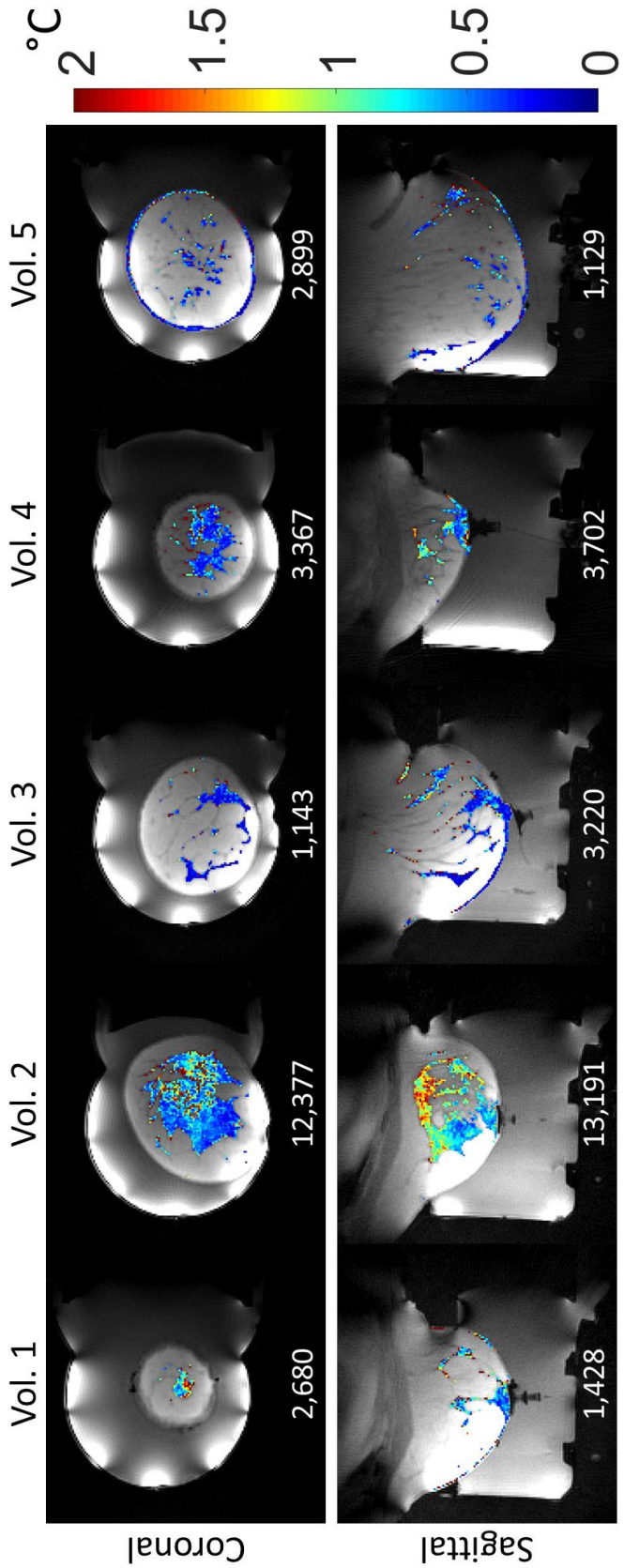

Figure 7.4. Standard deviation through time maps of PRF temperature in aqueous tissue for each volunteer using the CE-TB method and image set 1. The total number of aqueous voxels for each image orientation and volunteer is displayed at the bottom of each image.

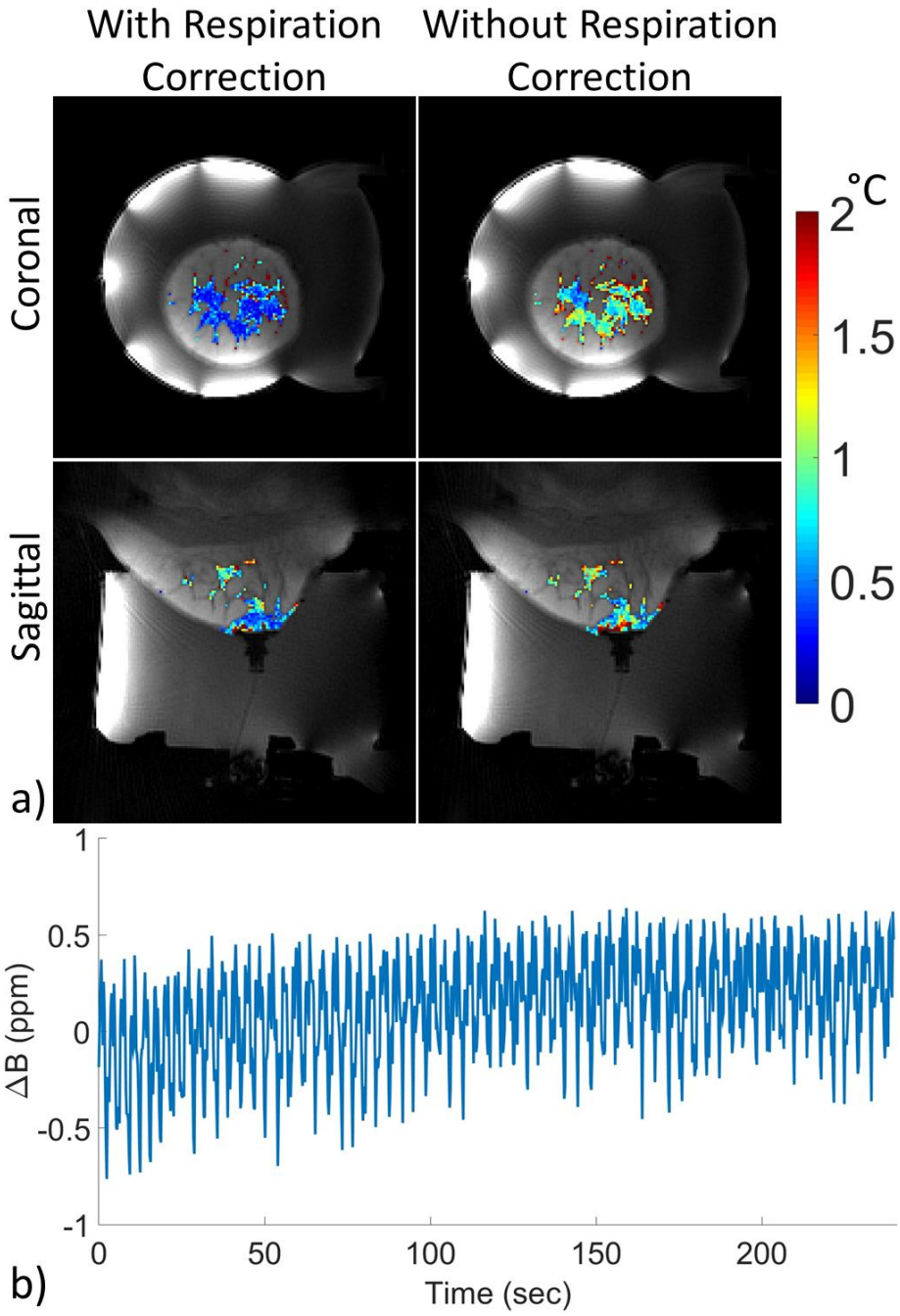

Figure 7.5. a) Standard deviation through time maps of PRF temperature in aqueous tissue with (left) and without (right) respiration correction for volunteer 4 using the CE-TB method and image set 1. b) Example of measured field shift in the central slice of the image set 1 coronal acquisition for volunteer 4.

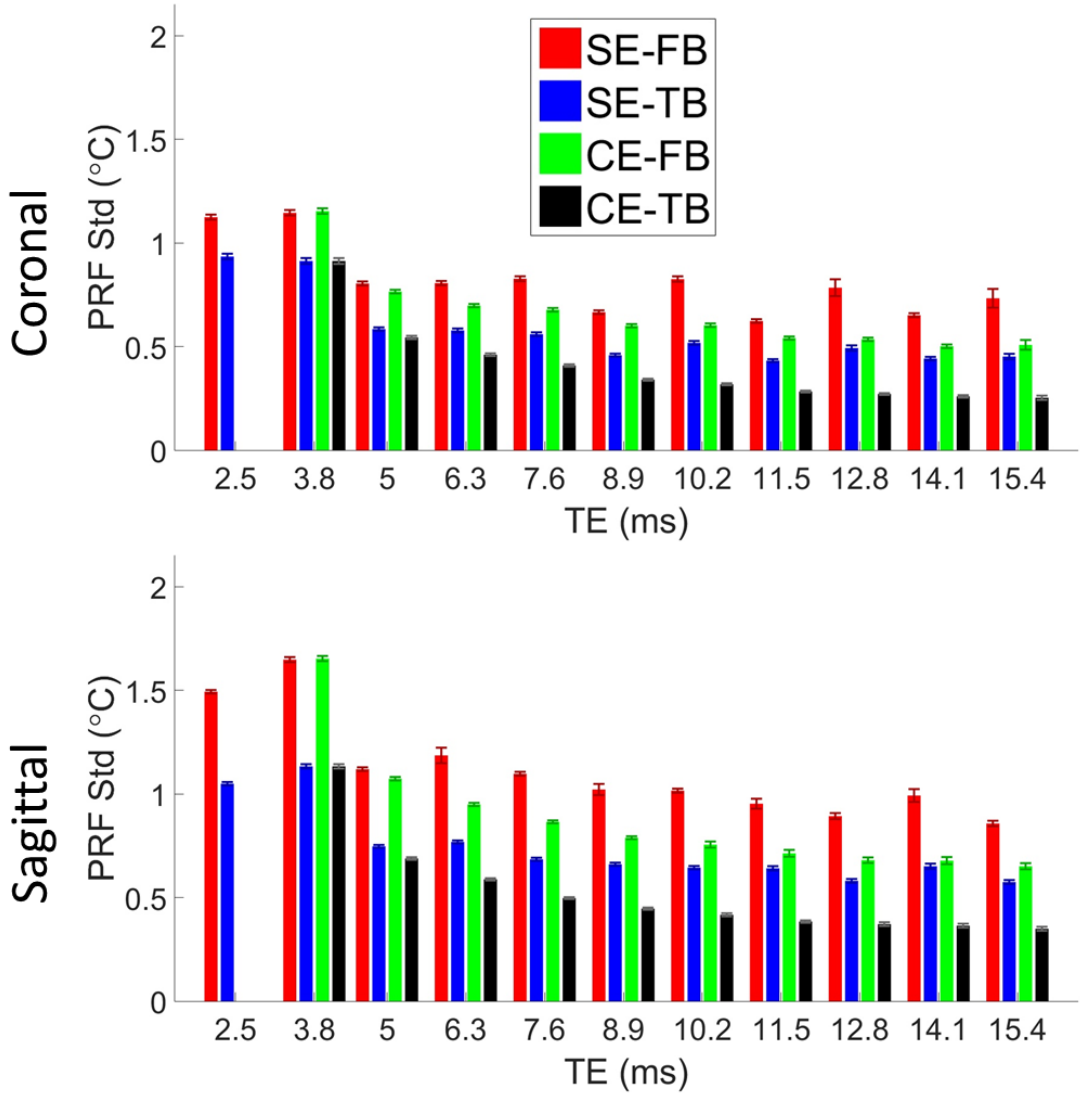

Figure 7.6. Spatially averaged PRF standard deviation as a function of TE in aqueous tissue in the breast for volunteer 3 and image set 1. Errors bars are the standard error of the average PRF standard deviation for each echo image volume. PRF temperature calculated using the: Red) SE-FB method; Blue) SE-TB method; Green) CE-FB method; Black) CE-TB method. The combined phases (CE methods) only used the echoes up to and including the displayed TE.

up to and including the displayed TE. Figure 7.7a shows the spatially averaged PRF standard deviation values for each volunteer for each of the four methods at the last TE from image set 1 in both coronal and sagittal orientation. For nearly every case, there was a statistically significant difference between each of the methods. The CE-TB method had the highest precision in both coronal and sagittal orientations for all three image sets and volunteers in all but one case (Image Set 3, Coronal, Volunteer 2). It should be noted that the error bars in Figure 7.7a are not a true standard error, as the variation present is not solely due to noise and has spatial location dependence (e.g., distance from coils and respiration). Figure 7.7b shows the average improvement

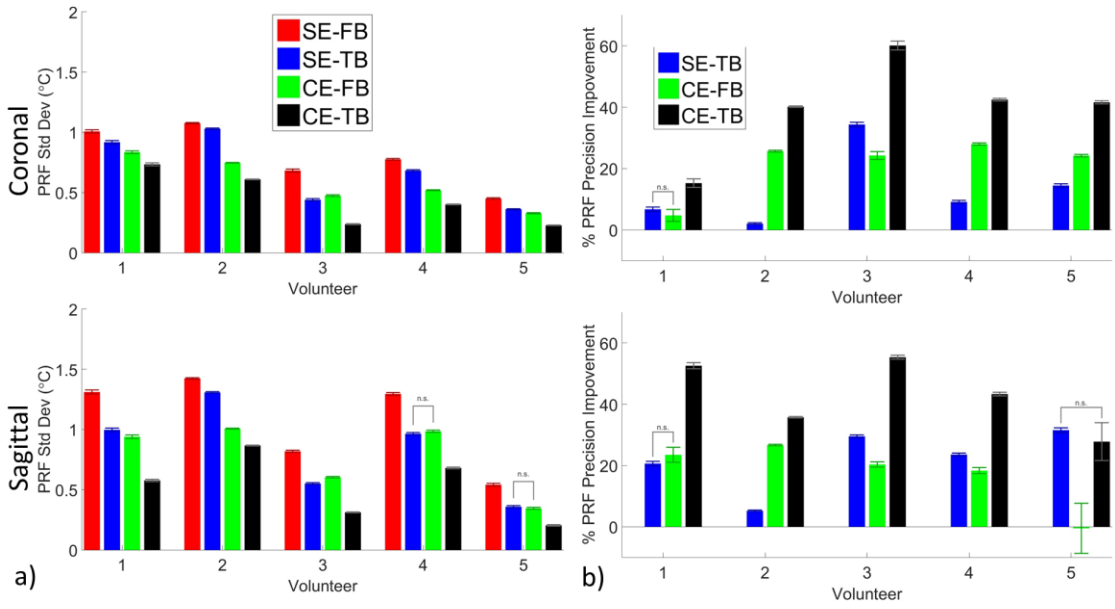

Figure 7.7. a) Spatially averaged PRF standard deviation values from image set 1 for the last TE in aqueous tissue in the breast for each volunteer in the coronal and sagittal orientations for each of the four calculation methods. Errors bars are the standard error of the spatial values. PRF temperature calculated using: Red) SE-FB method; Blue) SE-TB method; Green) CE-FB method; Black) CE-TB method. Bars between methods indicate no statistically significant difference between the methods. b) Average improvement in PRF precision compared to the SE-FB method. Bars between improvement values indicate no statistically significant difference between the methods.

in the precision compared to the SE-FB. For nearly every case, there was a statistically significant difference between each of the improvements.

Examples of the exponential decay fit are shown in Figure 7.8. Figure 7.8b shows an example of T_2^* measurements whether or not the offset C is accounted for, and Figure 7.8c gives an example of the offset C within the breast. Figure 7.9a shows the percent change from baseline of M(0) and T2* for volunteer 2. In all cases the precision of the M(0) and T2* estimates were better when only including the in-phase echoes instead of all echoes and an example is shown in Figure 7.9b. Time average values for M(0), T_2^* and offset C from the KWIC reconstructed images were nearly identical (within ~5%) to those obtained from fully sampled (without KWIC) images (not shown).

The FUS heating in pork results are shown in Figure 7.10. When heating within aqueous tissue, the CE-TB PRF measurements from the KWIC stack of stars

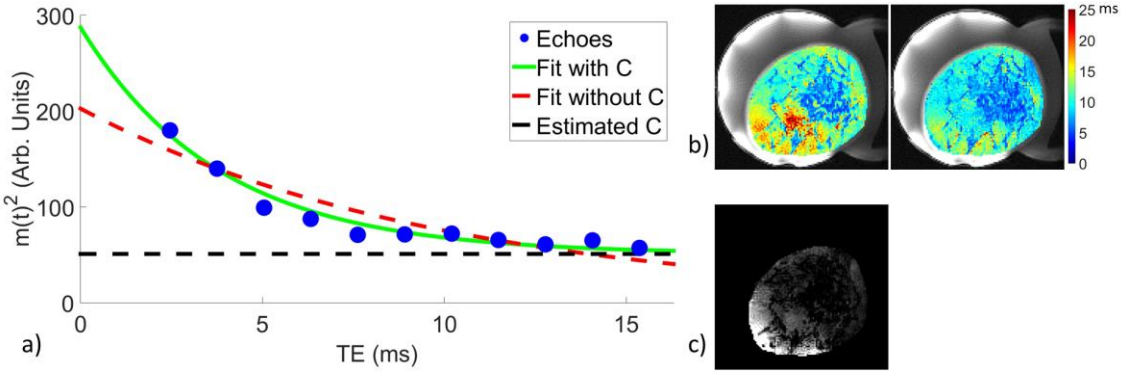

Figure 7.8. a) Example of SOS multiecho exponential decay with weighted linear least squares fit to data removing offset C (green) and without removing offset C (red dash). b) Example of T_2^* measurements within the breast without removing C (left) and with removing C (right). The T_2^* values within aqueous and adipose tissue are more uniform after removing the offset C. c) Example of the measured offset value C within the breast.

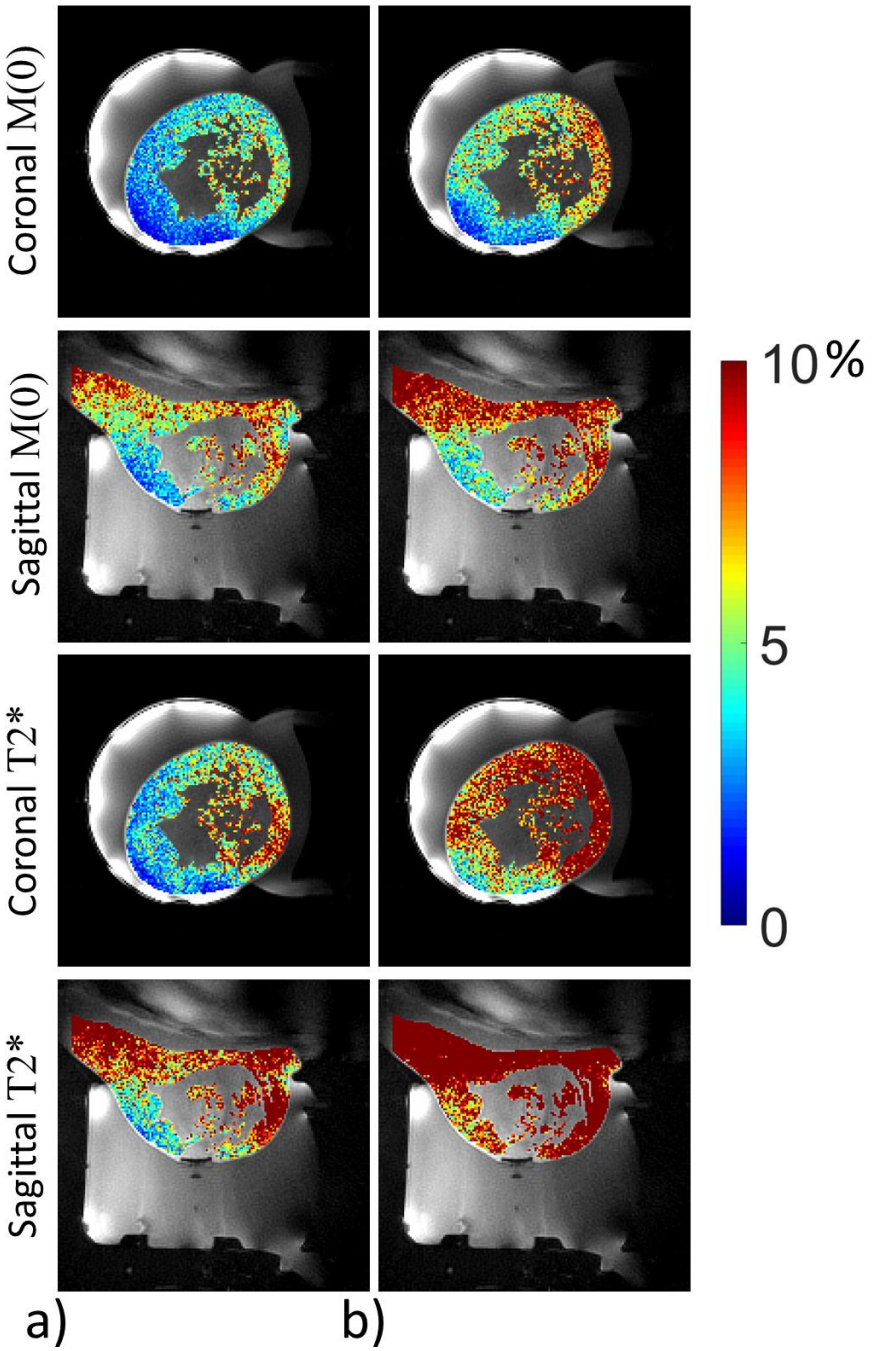

Figure 7.9. Standard deviation through time maps for volunteer 2 of M(0) and T2* as a percent difference from the baseline value determined using the trajectory matched baseline library a) using only the in phase echoes and b) using all echoes in the fit.

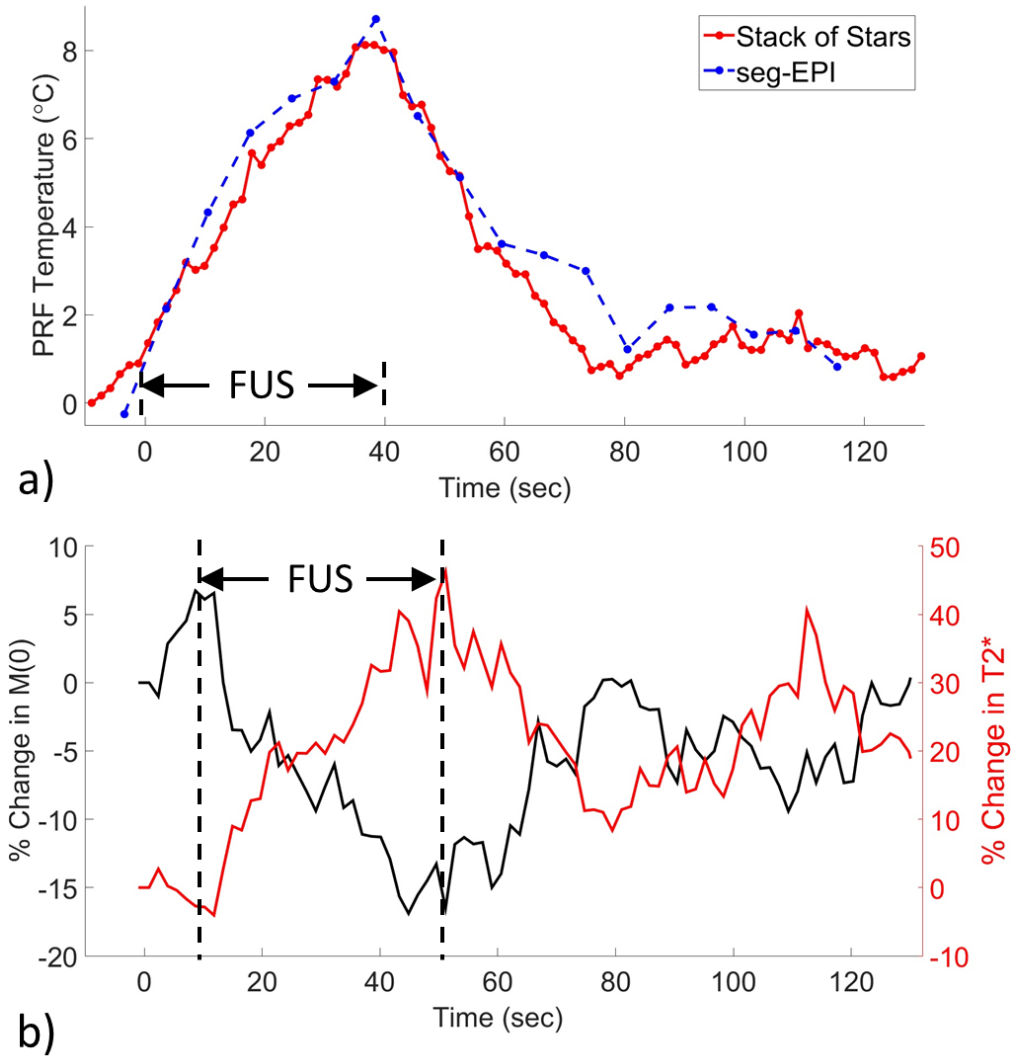

Figure 7.10. Phantom FUS heating. a) PRF temperature change during FUS heating in aqueous tissue within a pork phantom. Solid red line – CE-TB Stack of stars sequence. Dashed blue line – seg-EPI sequence. b) Percent change in M(0) (black) and percent change in T_2^* (red) during FUS heating in adipose tissue within a pork phantom. Vertical bars indicate the duration of the FUS.

sequence were comparable with those obtained from the seg-EPI sequence (Figure 7.10a). Time lapse videos of the PRF temperature change using the stack of stars and seg-EPI sequences are provided in Supporting Video S1. Both T2* and M(0) showed temperature dependence in pork adipose tissue when heating with FUS (Figure 7.10b).

7.4 Discussion

The multiecho stack of stars acquisition and reconstruction method described in this paper provides simultaneous measurements of PRF temperature change, M(0), T2* and water/fat separation with a large field of view (208 x 208 x 20.8 mm) with high spatial (1.3 mm isotropic) and temporal (1.43 s) resolution. The PRF precision (temperature standard deviation) ranged between ~0.3-1.0 °C between the volunteers and the coronal and sagittal orientations, and the measured PRF temperature change during MRgFUS was comparable to a 3D seg-EPI sequence.

The multiple echo acquisition provided several advantages. Self-navigated respiration correction allowed for free breathing and improved PRF precision as seen in Figure 7.6. There was no need for fat saturation because the high readout bandwidth and radial acquisition minimized the chemical shift artifact. The phase information from each echo was combined to significantly improve the PRF temperature measurement precision as quantified in Figure 7.7. For voxels with significant mixing of water and fat, phase combination would likely produce errors due to the frequency difference between water and fat. Combining the phases of only the in-phase echoes would remove the error due to the fat mixture, but would use fewer echoes in the combination. The magnitude information from the in-phase echoes was combined to calculate M(0) and T2* which could potentially be used as a measure of temperature

change in adipose tissue as seen in Figure 7.10b. The stack of stars sequence provided comparable heating profiles to a 3D seg-EPI sequence as shown in Figure 7.10a. Another advantage of the stack of stars sequence is that it does not have the same image distortion that is present in a seg-EPI sequence.

The KWIC window improves the temporal resolution while maintaining the high spatial resolution. It also causes the undersampling artifacts to vary between reconstructed time points due to the k-space distribution rotation between reconstructed time points, and was the primary source of error in the SE-FB and CE-FB PRF measurements. Using the PGA increment causes the undersampling artifacts to repeat and allows for the use of a trajectory-matched baseline library, which gave significant improvement when using the SE-Tb and CE-TB measurements. The PRF temperature measurements calculated from the combined echo phase and using the baseline library had statistically significant improvement in precision compared to those calculated from a single echo phase with a single baseline. Each k-space disk enclosed by a KWIC ring represents objects or object details within a specific size range. The KWIC algorithm updates central k-space (the central disk), which represents larger object detail, with a higher temporal resolution. Fine object details are updated at the same rate with the sliding window, but will have a lower temporal resolution as this information is enclosed by the outer rings of the KWIC window. The temporal resolution of the focus will depend on the KWIC window attributes (number of inner/outer lines, update rate) and the size of the focus.

The total number of lines included in the KWIC window can also be adjusted. The KWIC window used in this work had a temporal window covering 75 s for image

set 1 and 41 s for image set 2. The full effect of different KWIC window parameters and focus sizes remains to be investigated, and the authors have plans to investigate with simulation and experimental studies. Lowering the total number of lines will improve the temporal resolution of each ring while sacrificing SNR to increased undersampling artifacts, Figure 7.1c. These artifacts could possibly be reduced through a compressed sensing or regularized reconstruction (49). While all the images in this study were updated at a constant rate of 13 projections, the PGA allows for arbitrary temporal position of the reconstruction. The trajectory-matched baseline library can still be used with an arbitrary temporal position by an appropriate shift of the KWIC window to select a baseline image reconstructed with the same k-space distribution rotation.

The precision of the PRF, M(0) and T2* measurements depended on several factors which include location within the breast (distance from chest wall and from imaging coils), the number of lines included in the KWIC window, and the image orientation. Voxels closer to the chest wall experienced greater respiration artifact. The respiration correction assumes a spatially uniform off resonance, which is a more accurate assumption in the coronal orientation, though tissue sufficiently far away from the chest in the sagittal images had comparable PRF precision to the coronal images, as seen in Figure 7.4.

Changes in M(0) and T2* with temperature need calibration and verification before reliable temperature measurements can be made through either parameter. The precisions of M(0) and T2* were higher in adipose tissue compared to aqueous, likely due to the higher signal intensity from the shorter T1 of adipose tissue. It has been

shown that T2 in adipose tissue will increase with temperature (40,41). T2* is also affected by any intravoxel dephasing. A large temperature gradient across a voxel will decrease T2*, creating an opposite dependence with temperature. Decreasing the voxel size will attenuate this problem but will also lower SNR. The only effect that the KWIC window had on M(0) and T2* measurements was to decrease SNR due to the retrospective undersampling.

The effective noise variance C was spatially variant, as shown in Figure 7.8c, which indicates that the noise is not Gaussian distributed white noise after regridding the SOS sequence (50) , though the true source of the spatial variation remains to be determined. T2* measurements were more uniform within the breast when taking into account C as shown in Figure 7.8b. The standard deviation through time of T2* was also improved when accounting for C (not shown). The offset value C used when fitting the exponential decay is only an approximation of the true effects of noise in non-Cartesian magnitude MR images. A more accurate model of the noise may improve the M(0) and T2* precision further.

7.5 Conclusion

This work provides promising results for implementing a 3D method of monitoring thermal therapies using a multiecho PGA stack of stars sequence. This novel sequence provides PRF temperature, M(0) and T2* (which may become useful indicators of temperature change), water/fat separation, allows for free breathing and has high spatial and temporal resolution. The sliding KWIC window with PGA acquisition increases its versatility by allowing reconstruction of images at arbitrary time points. PRF temperature precision was significantly improved by combining

phases from multiple echoes and by using a trajectory-matched baseline library. The temperature measurement accuracy during FUS heating was comparable to a 3D seg-EPI sequence.

7.6 Appendix A

To simplify the readability of the solution, we will express the magnitude of a single pixel x at the jth echo as y_j and the phase of pixel x at the jth echo as ψ_j. The weighted linear least squares function in Equation [7.8] is minimized by taking the derivate of X^2 with respect to *a* and *b* and setting both equations equal to zero.

$$\frac{dX^2}{da} = -2\sum_{j=1}^{n} {y_j}^2(\psi_j - a - bTE_j) = 0$$
$$\frac{dX^2}{db} = -2\sum_{j=1}^{n} {y_j}^2 TE_j(\psi_j - a - bTE_j) = 0 \qquad [7.15]$$

When put into matrix form this becomes

$$\begin{bmatrix} \sum {y_j}^2 & \sum TE_j {y_j}^2 \\ \sum TE_j {y_j}^2 & \sum TE_j^2 {y_j}^2 \end{bmatrix} \begin{bmatrix} a \\ b \end{bmatrix} = \begin{bmatrix} \sum {y_j}^2 \psi_j \\ \sum TE_j {y_j}^2 \psi_j \end{bmatrix} \qquad [7.16]$$

To slightly simplify these equations, we can define the following variables

$$r = \sum (TE_j^2 {y_j}^2) \quad s = \sum ({y_j}^2 \psi_j) \quad t = \sum (TE_j {y_j}^2)$$
$$u = \sum (TE_j {y_j}^2 \psi_j) \quad v = \sum {y_j}^2 \qquad [7.17]$$

The first matrix is inverted and multiplied to both sides to obtain the following solutions to *a* and *b*

$$a = \frac{r * s - t * u}{v * r - t^2} \qquad [7.18]$$

$$b = \frac{v * u - t * s}{v * r - t^2}$$

The combined phase at any TE is then simply given by

$$\hat{\psi}(x, TE) = a + bTE \quad [7.19]$$

7.7 Appendix B

The magnitude of the measured MRI signal in the presence of noise has the form:

$$m(t) = (M(0)^2 e^{-2t/T2^*} + C)^{1/2} = (Ae^{-Bt} + C)^{1/2} \quad [7.20]$$

where C represents the effective noise variance, which may be spatially variant in radial sequences, $A = M(0)^2$ and $B = 2/\mathrm{T2}^*$. This can be expressed with the following form,

$$m^2 = y = Ae^{-Bt} + C. \quad [7.21]$$

The offset C can be estimated without using an iterative process (51). Start by subtracting C from both sides and taking the derivative with respect to t.

$$y - C = Ae^{-Bt} \quad [7.22]$$

$$y' = -BAe^{-Bt} \quad [7.23]$$

$$y' = B(C - y) \quad [7.24]$$

Defining the error function to be

$$e = y' - B(C - y) \quad [7.25]$$

The total squared error to minimize is

$$X^2 = \int_{t_0}^{t} (y' - B(C - y))^2 \, du \quad [7.26]$$

This error function is optimized further by weighting the squared error by the inverse of y to give more weight to samples closer to the offset C.

$$X^2 = \int_{t_0}^{t} \frac{1}{y}(y' - B(C - y))^2 \, du \qquad [7.27]$$

The total error function in Equation [7.27] is minimized to estimate the value of the constant C by taking the derivate of X^2 with respect to B and C, setting both equations equal to zero and solving for C which has the following solution.

$$C = \frac{\ln\frac{y(t)}{y(t_0)}\int_{t_0}^{t} y\,du - (t - t_0)(y(t) - y(t_0))}{\ln\frac{y(t)}{y(t_0)}(t - t_0) - (y(t) - y(t_0))\int_{t_0}^{t}\frac{1}{y}\,du} \qquad [7.28]$$

In discreet form with uniform spacing between samples, the solution for C has the following form

$$C = \frac{\ln\frac{y_n}{y_1}\sum_{j=1}^{n} y_j - n(y_n - y_1)}{\ln\frac{y_n}{y_1} * n - (y_n - y_1)\sum_{j=1}^{n}\frac{1}{y_j}} \qquad [7.29]$$

where n is the total number of samples.

7.8 References

1. Stafford RJ, Hazle JD. Magnetic resonance temperature imaging for focused ultrasound surgery: a review. Top Magn Reson Imaging 2006;17(3):153-163.

2. Jolesz FA. MRI-guided focused ultrasound surgery. Annu Rev Med 2009;60:417-430.

3. Medel R, Monteith SJ, Elias WJ, Eames M, Snell J, Sheehan JP, Wintermark M, Jolesz FA, Kassell NF. Magnetic resonance-guided focused ultrasound surgery: Part 2: A review of current and future applications. Neurosurgery 2012;71(4):755-763.

4. Kennedy JE, Ter Haar GR, Cranston D. High intensity focused ultrasound: surgery of the future? Br J Radiol 2003;76(909):590-599.

5. Tempany CM, McDannold NJ, Hynynen K, Jolesz FA. Focused ultrasound surgery in oncology: overview and principles. Radiology 2011;259(1):39-56.

6. Rieke V, Butts Pauly K. MR thermometry. J Magn Reson Imaging 2008;27(2):376-390.

7. Salomir R, Delemazure AS, Palussiere J, Rouviere O, Cotton F, Chapelon JY. Image-based control of the magnetic resonance imaging-guided focused ultrasound thermotherapy. Top Magn Reson Imaging 2006;17(3):139-151.

8. Pinton G, Aubry JF, Bossy E, Muller M, Pernot M, Tanter M. Attenuation, scattering, and absorption of ultrasound in the skull bone. Med Phys 2012;39(1):299-307.

9. Gallay MN, Moser D, Rossi F, Pourtehrani P, Magara AE, Kowalski M, Arnold A, Jeanmonod D. Incisionless transcranial MR-guided focused ultrasound in essential tremor: cerebellothalamic tractotomy. J Ther Ultrasound 2016;4:5.

10. Magara A, Buhler R, Moser D, Kowalski M, Pourtehrani P, Jeanmonod D. First experience with MR-guided focused ultrasound in the treatment of Parkinson's disease. J Ther Ultrasound 2014;2:11.

11. McDannold N, Clement GT, Black P, Jolesz F, Hynynen K. Transcranial magnetic resonance imaging- guided focused ultrasound surgery of brain tumors: initial findings in 3 patients. Neurosurgery 2010;66(2):323-332; discussion 332.

12. Schlesinger D, Benedict S, Diederich C, Gedroyc W, Klibanov A, Larner J. MR-guided focused ultrasound surgery, present and future. Med Phys 2013;40(8):080901.

13. Weintraub D, Elias WJ. The emerging role of transcranial magnetic resonance imaging-guided focused ultrasound in functional neurosurgery. Mov Disord 2016.

14. Hinkelman LM, Liu DL, Waag RC, Zhu Q, Steinberg BD. Measurement and correction of ultrasonic pulse distortion produced by the human breast. J Acoust Soc Am 1995;97(3):1958-1969.

15. Todd N, Vyas U, de Bever J, Payne A, Parker DL. The effects of spatial sampling choices on MR temperature measurements. Magn Reson Med 2011;65(2):515-521.

16. Todd N, Adluru G, Payne A, DiBella EV, Parker D. Temporally constrained reconstruction applied to MRI temperature data. Magn Reson Med 2009;62(2):406-419.

17. Todd N, Payne A, Parker DL. Model predictive filtering for improved temporal

resolution in MRI temperature imaging. Magn Reson Med 2010;63(5):1269-1279.

18. Roujol S, de Senneville BD, Hey S, Moonen C, Ries M. Robust adaptive extended Kalman filtering for real time MR-thermometry guided HIFU interventions. IEEE Trans Med Imaging 2012;31(3):533-542.

19. Griswold MA, Jakob PM, Heidemann RM, Nittka M, Jellus V, Wang J, Kiefer B, Haase A. Generalized autocalibrating partially parallel acquisitions (GRAPPA). Magn Reson Med 2002;47(6):1202-1210.

20. Diakite M, Odeen H, Todd N, Payne A, Parker DL. Toward real-time temperature monitoring in fat and aqueous tissue during magnetic resonance-guided high-intensity focused ultrasound using a three-dimensional proton resonance frequency T1 method. Magn Reson Med 2014;72(1):178-187.

21. Odeen H, Todd N, Diakite M, Minalga E, Payne A, Parker DL. Sampling strategies for subsampled segmented EPI PRF thermometry in MR guided high intensity focused ultrasound. Med Phys 2014;41(9):092301.

22. Svedin BT, Payne A, Parker DL. Respiration artifact correction in three-dimensional proton resonance frequency MR thermometry using phase navigators. Magn Reson Med 2015.

23. Fielden S, Zhao L, Miller W, Feng X, Wintermark M, Pauly KB, Meyer C. Spiral-based 3D MR thermometry. J Ther Ultrasound 2015;3(1):P18.

24. Durand E, van de Moortele PF, Pachot-Clouard M, Le Bihan D. Artifact due to B(0) fluctuations in fMRI: correction using the k-space central line. Magn Reson Med 2001;46(1):198-201.

25. Song HK, Dougherty L. k-space weighted image contrast (KWIC) for contrast manipulation in projection reconstruction MRI. Magn Reson Med 2000;44(6):825-832.

26. Song HK, Dougherty L. Dynamic MRI with projection reconstruction and KWIC processing for simultaneous high spatial and temporal resolution. Magn Reson Med 2004;52(4):815-824.

27. Uecker M, Lai P, Murphy MJ, Virtue P, Elad M, Pauly JM, Vasanawala SS, Lustig M. ESPIRiT--an eigenvalue approach to autocalibrating parallel MRI: where SENSE meets GRAPPA. Magn Reson Med 2014;71(3):990-1001.

28. Winkelmann S, Schaeffter T, Koehler T, Eggers H, Doessel O. An optimal radial profile order based on the Golden Ratio for time-resolved MRI. IEEE Trans Med Imaging 2007;26(1):68-76.

29. Block KT, Chandarana H, Milla S, Bruno M, Mulholland T, Fatterpekar G, Hagiwara M, Grimm R, Geppert C, Kiefer B, Sodickson DK. Towards Routine Clinical Use of Radial Stack-of-Stars 3D Gradient-Echo Sequences for Reducing Motion Sensitivity. J Korean Soc Magn Reson Med 2014;18(2):87-106.

30. McGibney G, Smith MR, Nichols ST, Crawley A. Quantitative evaluation of several partial fourier reconstruction algorithms used in mri. Magn Reson Med 1993;30(1):51-59.

31. Peters DC, Derbyshire JA, McVeigh ER. Centering the projection reconstruction trajectory: reducing gradient delay errors. Magn Reson Med 2003;50(1):1-6.

32. Brodsky EK, Samsonov AA, Block WF. Characterizing and correcting gradient errors in non-cartesian imaging: Are gradient errors linear time-invariant (LTI)? Magn Reson Med 2009;62(6):1466-1476.

33. Lee KJ, Paley MN, Griffiths PD, Wild JM. Method of generalized projections algorithm for image-based reduction of artifacts in radial imaging. Magn Reson Med 2005;54(1):246-250.

34. Fessler JA, Sutton BP. Nonuniform fast Fourier transforms using min-max interpolation. IEEE Trans Sig Process 2003;51(2):560-574.

35. Knoll F, Scharzl A, Diwoky C, Sodickson D. gpuNUFFT - An Open-Source GPU Library for 3D Gridding with Direct Matlab Interface. In Proceedings of the 22nd Annual Meeting of ISMRM, Milan, Italy, 2014. p. 4297.

36. Benkert T, Feng L, Sodickson DK, Chandarana H, Block KT. Free-breathing volumetric fat/water separation by combining radial sampling, compressed sensing, and parallel imaging. Magn Reson Med 2016.

37. Jeong HJ, Eddleman CS, Shah S, Seiberlich N, Griswold MA, Batjer HH, Carr JC, Carroll TJ. Accelerating time-resolved MRA with multiecho acquisition. Magn Reson Med 2010;63(6):1520-1528.

38. Marx M, Butts Pauly K. Improved MRI thermometry with multiple-echo spirals. Magn Reson Med 2016;76(3):747-756.

39. Rieke V, Pauly KB. Echo Combination to Reduce PRF Thermometry Errors From Fat. J Magn Reson Imag 2008;27(3):673-677.

40. Ozhinsky E, Kohi MP, Ghanouni P, Rieke V. T2-based temperature monitoring in abdominal fat during MR-guided focused ultrasound treatment of patients with uterine fibroids. J Ther Ultrasound 2015;3:15.

41. Baron P, Ries M, Deckers R, de Greef M, Tanttu J, Kohler M, Viergever MA, Moonen CT, Bartels LW. In vivo T2 -based MR thermometry in adipose tissue layers for high-intensity focused ultrasound near-field monitoring. Magn Reson Med 2014;72(4):1057-1064.

42. Parker DL. Applications of NMR Imaging in Hyperthermia: An Evaluation of the Potential for Localized Tissue Heating and Noninvasive Temperature Monitoring. IEEE Trans Biomed Eng 1984;BME-31(1):161-167.

43. Peters NH, Bartels LW, Sprinkhuizen SM, Vincken KL, Bakker CJ. Do respiration and cardiac motion induce magnetic field fluctuations in the breast and are there implications for MR thermometry? J Magn Reson Imaging 2009;29(3):731-735.

44. Roemer PB, Edelstein WA, Hayes CE, Souza SP, Mueller OM. The NMR phased array. Magn Reson Med 1990;16(2):192-225.

45. Payne A, Merrill R, Minalga E, Vyas U, de Bever J, Todd N, Hadley R, Dumont E, Neumayer L, Christensen D, Roemer R, Parker D. Design and characterization of a laterally mounted phased-array transducer breast-specific MRgHIFU device with integrated 11-channel receiver array. Med Phys 2012;39(3):1552-1560.

46. Payne A, Todd N, Minalga E, Wang Y, Diakite M, Hadley R, Merrill R, Factor R, Neumayer L, Parker DL. In vivo evaluation of a breast-specific magnetic resonance guided focused ultrasound system in a goat udder model. Med Phys 2013;40(7):073302.

47. Minalga E, Payne A, Merrill R, Todd N, Vijayakumar S, Kholmovski E, Parker DL, Hadley JR. An 11-channel radio frequency phased array coil for magnetic resonance guided high-intensity focused ultrasound of the breast. Magn Reson Med 2013;69(1):295-302.

48. Glover GH, Schneider E. Three-point Dixon technique for true water/fat decomposition with B0 inhomogeneity correction. Magn Reson Med 1991;18(2):371-383.

49. Feng L, Axel L, Chandarana H, Block KT, Sodickson DK, Otazo R. XD-GRASP: Golden-angle radial MRI with reconstruction of extra motion-state dimensions using compressed sensing. Magn Reson Med 2016;75(2):775-788.

50. Mosquera C, Irarrazabal P, Nishimura DG. Noise behavior in gridding reconstruction. 1995 9-12 May 1995. p 2281-2284 vol.2284.

51. Bristow-Johnson, Robert. Non-linear curve fitting: y = Ae^(-t/tau) + C. https://www.dsprelated.com/showthread/comp.dsp/58555-1.php. Published May 24, 2006. Accessed December 4, 2016.

CHAPTER 8

CONCLUSIONS

The work presented in this dissertation has focused on improving temperature imaging in MRI by developing improved temperature measurement sequences, evaluating the accuracy of 2D T1 measurements, which can be used to measure temperatue in fat, and developing a method to quickly locate the ultrasound focus for rapid targeting. The ability of MRI to noninvasively monitor temperature changes in near real time provides vital feedback for thermal therapy treatments such as FUS. These treatments are made safer by this ability to monitor the induced temperature change to ensure that only the desired tissue is treated, while healthy tissue is left unharmed. The energy deposition of thermal therapies can cover a large volume. It is therefore important to monitor not just the region with the highest deposition of energy, but the entire volume of possible energy deposition to ensure safety. Increasing the imaging volume will typically increase the required scan time by a proportional amount. Increasing the imaging volume can also introduce (or enhance) artifacts, such as respiration motion, that are not a problem with a smaller field of view.

The work presented in chapter four examined the effect of the excitation slice profile on T_1 measurements using the VFA method. Changes in T1 have been used as a measure of temperature in adipose tissue. During RF excitation, a truncated sinc

pulse is typically used. The truncation artifact causes the slice profile to not have the desired rectangular shape with uniform excitation throughout the slice. The spins across the slice will experience a flip angle that ranges from zero to the desired angle and then back to zero. When the desired angle is above the Ernst angle, spins near the edge of the slice profile will have a higher signal than those at the center when at steady state. This extra signal contribution will lead to errors when computing the T1 of the voxel using the VFA method with a 2D acquisition.

The VFA method uses the steady state signal equation and signals that were acquired at two different flip angles to calculation T1. The extra signal from the edges of the slice profile cause the signal in the voxel to vary from that predicted by the steady state signal equation. It was shown that while accurate T1 estimates were possible using the VFA method with 2D acquisition, only a limited number of flip angle combinations produced those accurate results. Any two flip angle combinations outside of the narrow band led to significant errors in the T1 estimate. These results demonstrate that accurate T1 measurements with 2D acquisition are impractical at best, and generally inaccurate. Accurate T1 measurements can be obtained using the VFA method using the central slices of a 3D acquisition, where the slice profile is essentially constant across the central slices.

The work presented in chapter five focused on the artifact introduced by respiration motion outside the imaging field of view. Respiration motion is problematic in breast imaging, even though the breast itself can be immobilized. The constant motion of the distribution of susceptible material will cause off resonance phase changes between every excitation. The phase offsets lead to ghosting artifacts.

The correction method presented in this chapter used two FID phase navigators to measure the phase offset every TR. The phase difference between the two navigators is directly proportional to the off resonance frequency. Adjusting the phase of k-space to remove the excess phase led to significant improvements in both the magnitude and phase images. The correction method was evaluated with phantoms and in vivo breast. The FID phase navigator correction resulted in an average improvement to the PRF temperature precision by a factor of 2 in coronal 3D seg-EPI sequences.

The work presented in chapter six focused on rapidly predicting the ultrasound focus location in MR coordinates of a transducer with multiple degrees of freedom. Three small tracker coils were built and rigidly attached to the ultrasound housing. An MRI sequence with a simple 1D readout performed along each of the three axes provided the positions of the tracker coils. The position of the ultrasound focus relative to the tracker coil positions was calibrated in a gelatin phantom. The Euclidean transformation of the calibrated tracker positions to their current positions was calculated. The same transformation was applied to the calibrated focus position to predict its current location. The imaging sequence and prediction calculation took less than 1 second to perform. Testing the tracker coils prediction accuracy in a gelatin phantom resulted in an average error in the prediction of approximately 2 mm. This method resulted in a fast and accurate method for predicting the location of the ultrasound focus for transducers with multiple degrees of freedom.

Chapter 7 presented a method to monitor temperature changes with a large field of view and high spatial and temporal resolution using a pseudo-golden angle multi-echo stack of stars sequence with k-space weighted image contrast (KWIC). The

KWIC reconstruction increased the temporal resolution of the radial acquisition by including data over a smaller temporal window in the center region of k-space. A golden angle distribution of projections guarantees an optimal distribution for an arbitrary number of projection angles. The pseudo-golden angle caused the artifacts from the KWIC undersampling to repeat, which allowed for a multibaseline library to remove those artifacts. The multiple echo acquisition gave several advantages. Respiration offsets can be corrected using self-navigation. Separate water/fat images can be generated. The phase and magnitude information from each echo can be combined to improve the precision of PRF temperature measurements and provide quantitative measurements of T2* and M(0), which can possibly be used as a measure of temperature in adipose tissue.

The stack of stars KWIC method was tested in both a pork phantom and five healthy volunteers. Both the multibaseline library and echo phase combination provided significant improvements to the PRF temperature precision. The PRF precision within the breast ranged between 0.3-1.0 °C. T2* and M(0) measurements displayed a temperature dependence during FUS heating in adipose tissue in the pork phantom. The ability of this sequence to simultaneously measure temperature changes in aqueous and adipose tissue with high precision is promising for monitoring thermal therapies within structures containing a significant amount of tissue mixture, such as the breast.